UTS UNIVERSITY
OF TECHNOLOGY
SYDNEY

Modelling Flowable Engineered Cementitious Composites and Its Fibre Orientation and Distribution for Tensile Performance Evaluation

by Hai Tran Thanh

Thesis submitted in fulfilment of the requirements for the degree of

Doctor of Philosophy

under the supervision of Professor Jianchun Li, A/Professor Yixia Zhang and Dr. Jianguo Wang

University of Technology Sydney
Faculty of Engineering and Information Technology

January 2021

Certificate of Original Authorship

I, Hai Tran Thanh declare that this thesis is submitted in fulfilment of the requirements for the award of Doctor of Philosophy, in the Faculty of Engineering and Information Technology at the University of Technology Sydney

This thesis is wholly my own work unless otherwise referenced or acknowledged. In addition, I certify that all information sources and literature used are indicated in the thesis.

This document has not previously been submitted for qualifications at any other academic institution.

Signature of Candidate

Production Note:
Signature removed prior to publication.

Date: January 4, 2021

Acknowledgements

First of all, I would like to express my sincere gratefulness to my principal supervisor, Professor Jianchun Li, for his great supervision, tremendous support and constant inspiration during my PhD study at the Centre for Built Infrastructure Research, University of Technology Sydney (UTS). I would also wish to thank my external supervisor, Associate Professor Yixia Zhang from Western University of Sydney for her helpful discussions and papers revision, and my co-supervisor Dr. Jack Wang at UTS for his helpful suggestions.

I would also like to thank all my friends and colleagues at UTS for making my time here enjoyable and memorable.

And finally, I want to dedicate all the works in this thesis to my beloved family for their endless encouragement and unconditional love. An exceptional and heartfelt thanks to my wife, Hang Duong, and my two sons, Ben and Bao, for their love and sacrifices throughout stages of my study.

Publications from this Thesis

In this thesis, the research contents of Chapter III, IV, and V have been published, and Chapter VI has been submitted for publication.

Journal Papers

1. Thanh, H.T., Li, J. & Zhang, Y. 2019, 'Numerical modelling of the flow of self-consolidating engineered cementitious composites using smoothed particle hydrodynamics', *Construction and Building Materials*, vol. 211, pp. 109-19, (Chapter III).

2. Thanh, H.T., Li, J. & Zhang, Y.X. 2020, 'Numerical simulation of self-consolidating engineered cementitious composite flow with the V-funnel and U-box', *Construction and Building Materials*, vol. 236, p. 117467, (Chapter IV).

3. Thanh, H.T., Li, J. & Zhang, Y.X. 2021, 'A novel approach for evaluating the orientation and distribution of fibre and their effects on the tensile performance of ECC', submitted to Cement and Concrete Composites and under review (Chapter VI).

Conference Paper

1. Thanh, H.T., Li, J. & Zhang, Y.X. 2020, 'Numerical evaluation the effect of specimen thickness on fibre orientation in self-consolidating engineered cementitious composites', RILEM-fib International Symposium on Fibre Reinforced Concrete, Springer, pp. 661-9, (Chapter V).

Book Chapter

1. Thanh, H.T., Li, J. & Zhang, Y. 2022, 'Numerical modelling of the flow of self-consolidating engineered cementitious composites using smoothed particle hydrodynamics', Advances in Engineered Cementitious Composites: Materials, Structures and Numerical Modelling. To be published in January 2022.

Table of Contents

List of Figures

xi

List of Tables

Abstract

Fibres have been implemented in cement-based materials in an attempt to overcome their brittleness nature. This implementation has illustrated the ability to reduce or eliminate the brittleness of concrete, enhance the ductility and fracture toughness of structures using fibre-reinforced cement-based materials (FRCs). However, it has been revealed by numerous studies that there is a dissimilarity in the mechanical performance of FRCs at different parts of specimens, even casting within the same mixture. The variation of fibres/matrix interaction, which is largely influenced by the distribution and orientation of fibre in the matrix, has been identified as a main factor leading to such divergence in FRCs behaviour. This vital shortcoming has restrained the application of FRCs in large-scale on-site production and industrial construction. Previous investigations have indicated the rheology properties of the fresh mix, fibre properties, mixing and casting procedure, size of specimens and wall-effect contribute to the fibre distribution and orientation in FRCs. Nevertheless, most research on the distribution and orientation of fibres in FRCs so far is limited to rigid steel fibre.

Engineered Cementitious Composites (ECC) is a unique class of high-performance fibre-reinforced cementitious composites (HPFRCC), exhibiting high tensile ductility with the tensile strain capacity up to 5% with a moderately low synthetic fibre fraction (typically 2% or less by volume). Through micromechanics tools, ECC properties can be engineered based on applications, forming a range of ECC materials for disparate functionalities in addition to the common characteristics of high tensile ductility and multiple fine cracking. Different groups of ECC are named based on their dominant characteristics. For example, self-consolidating or flowable ECC was

developed for large-scale on-site construction applications and employed in real-scale structural members. ECC typically utilises short synthetic fibres, such as polyvinyl alcohol (PVA) or polyethylene (PE) fibres, which are tiny in diameter. These fibres are flexible, i.e., they can be bent or coiled in the matrix of ECC. Notably, the orientation of a bent or coiled fibre varies at different cross-sections of the specimen. Moreover, actual distribution of the fibre orientation can be affected by other factors such as casting techniques or the rheology of fresh mix. Hitherto, what has not been reported is a reliable approach that can provide a full understanding of the orientation and distribution of flexible synthetic fibres in the matrix of ECC and practical information regarding fibre orientation and distribution for estimating the tensile performance of ECC.

The aim of this PhD research is to model the flow behaviour of ECC and then investigate the distribution and orientation of flexible synthetic fibres and their effects on the tensile performance of ECC material. To achieve this aim, a numerical model was first developed to simulate the flow of fresh ECC, in order to gain insights into ECC flow as well as distribution and orientation of flexible synthetic fibres in the cementitious matrix of fresh ECC. The developed model particularly focused on the flow characteristics of self-consolidating or flowable ECC. The flow of self-consolidating ECC was described as a non-Newtonian viscous fluid. The Lagrangian form of the Navier-Stokes constitutive equations of fresh ECC was solved using a mesh-free, smoothed particle hydrodynamics method. The flexible synthetic fibre in ECC was modelled as separate particles in the computational domain, which possessed identical continuum properties as mortar particles except for the drag force between two adjacent fibre particles.

The developed models were then validated by several standard tests through simulating the flow of self-consolidating ECC, including the flow cone tests, V-funnel and U-box tests. Numerical results were found to be consistent with the experimental test data obtained from the literature. Through these validations, the proposed model has proved its capability of providing insight into the flow behaviour of self-consolidating ECC in terms of filling, passing abilities and the distribution/orientation of flexible synthetic fibres. A simple technique was then proposed for evaluating the orientation distribution of flexible synthetic fibres at various sections of a simulated specimen after the fresh ECC stopped flowing in the mould. The influence of specimen thickness on the orientation of synthetic fibres in ECC was also numerically investigated through the simulation the casting of fresh self-consolidating ECC into different thicknesses of moulds. The bending phenomenon of flexible synthetic fibres and its influence on the distribution of fibre orientations were also studied.

Over the years, since the stress-crack opening relationship of a single crack at the lower mesoscale of ECC crucially governs the stress strain-hardening at its macroscale composite structure, several fibre-bridging constitutive models have been developed. However, although the two-way pullout mechanism of fibre, micro-matrix spalling and Cook-Gordon effects were considered in these models, the prediction of the stress-crack opening relationship still showed a remarkable difference compared to the experimental test data. To take advantage on the understanding of the orientation distribution of flexible synthetic fibres from the developed model above, a novel fibre-bridging model was also developed in this thesis. In this innovative model, the relationship between fibre stress and its displacement when bearing the stress released from the cracked matrix was derived through considering the two-way pullout mechanisms of an arbitrary inclined

fibre. Consequently, the findings of the proposed fibre-bridging model reveal much better agreements with the experimental testing data in comparison with existing models, especially during the pullout stage of fibre. Finally, a novel approach was proposed for estimating the tensile performance of ECC through the developed models at two states of ECC above. The information of fibre orientation and distribution at different cross-sections of a moulding specimen were incorporated into the developed fibre-bridging model to estimate the tensile behaviour of ECC. With this strategy, the distinct effects of fibre orientation and distribution on the tensile behaviour of ECC were also exposed.

Although the flowable ECC has garnered much attention in this work, the developed models in this thesis have great engineering potential for applications of other ECC. Extrudable or printable ECC, for instance, exhibits self-reinforcing properties being emerged as an encouraging material for 3D printing concrete. In this regard, modelling the extrusion process can be valuable for observing and evaluating the orientation and distribution of flexible fibres at each print filament. Moreover, modelling of extrudable ECC at the fresh state is worthwhile, and help us to understand the influences of its rheology properties on the deformation of filaments and stability of printed structures. If successful, this can save a huge amount of materials and effort on 3D printing research using ECC.

Chapter 1

Introduction

1.1 Engineered Cementitious Composites (ECC)

1.1.1 Historical development of ECC

Cement-based materials have long played an important role in the growth of civil infrastructure constructions worldwide. Many ultra-large-scale buildings as well as bridges or dams, etc., have been built - thanks to the outstanding performance in increasing tensile strength of concrete incorporated with steel as the reinforcement. However, brittleness, as one of the intrinsically disadvantageous characteristics of conventional concrete as well as ultra-high performance concrete, is still the major concern when building concrete-based structures. In attempting to overcome the brittle nature of concrete, fibres have been incorporated into concrete since the 1960s (Zollo 1997) and have proved able to reduce or eliminate brittleness, enhance ductility, fracture toughness and energy dissipation of structural elements (Parra-Montesinos 2005; Brandt 2008). A wide variety of fibre types such as steel, carbon, synthetic or natural fibre as well as cement-based matrix have been incorporated to form a range of fibre-reinforced concrete (FRC) or fibre-reinforced cementitious composites (FRCC) materials so far. While the matrix of FRC generally incorporates aggregates of various sizes, the matrix of FRCC contains no aggregates except for sand (Bentur & Mindess 2014). In general, the term FRCs is commonly used to refer to both FRC and FRCC materials.

For most conventional FRCC under tensile load, fracture energy can be improved by an order of magnitude with the tension-softening behaviour, but tensile strength or tensile strain typically does not increase much (Li 1993). The enhanced fracture toughness is mainly associated with energy absorption due to the fibre-bridging actions in the fracture process zone (Li & Maalej 1996; Cotterell & Mai 2014). To increase the

tensile strength and tensile strain of ordinary FRCC, micromechanical models served as a useful tool to tailor the matrix and fibre properties, fibre aspect ratio and fibre/matrix interaction. As a result, the steady state and multiple cracking in tension loading of FRCC with moderate fibre volume fraction were achieved (Li & Leung 1992; Li & Wu 1992; Li 1993). In 1987, Naaman proposed the name high-performance fibre-reinforced cement composites (HPFRCC) to describe the FRCC which exhibits strain-hardening behaviour and to differentiate it from strain-softening behaviour after first cracking occurs in regular FRCC in tensile performance (Naaman 2007) (Figure 1.1).
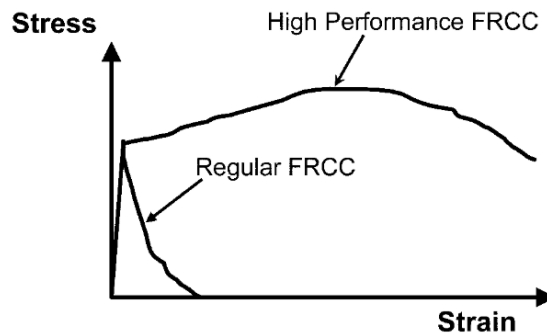
Figure 1.1   Tensile stress-strain behaviour of regular and high performance FRCC (Parra-Montesinos 2005).

Engineered cementitious composites (ECC), a typical member of HPFRCC, exhibits high tensile ductility in comparison with conventional concrete through the micro-mechanical interactions between short-random fibres and cementitious matrix. These determine the fibre-bridging strength, forming multiple fine cracks under loading action. The term "Engineered Cementitious Composite" emphasises the deliberate constituent tailoring and optimisation method embodied in ECC (Li 1993). Another name of ECC, i.e., Strain Hardening Cementitious Composites has been commonly used in Europe and South Africa, and it was first proposed by the RILEM technical committee on HPFRCC to emphasise the unique tensile strain-hardening properties of this material

(Li 2008). In China, the term Ultra High Toughness Cementitious Composite is popularly used to classify the FRCC possessing tensile strain capacity larger than 3% while reinforced by less than 2.5% short fibre by volume (Hedong 2008; Li et al. 2009). Ductile Fibre Reinforced Cementitious Composite (DFRCC) is the term generally employed in Japan, and it was suggested by a research committee of the Japan Concrete Institute (JCI). This agency was established to examine such ductile materials and their application in industrial construction (Kunieda & Rokugo 2006). Meanwhile, the Japan Society of Civil Engineers (JSCE) has called the material as "Multiple Fine Cracking Fibre Reinforced Cementitious Composites" to emphasise the multiple fine cracking characteristics. Essentially, all of these materials have been established via micromechanical approaches, and they exhibit identical material behaviour as ECC.
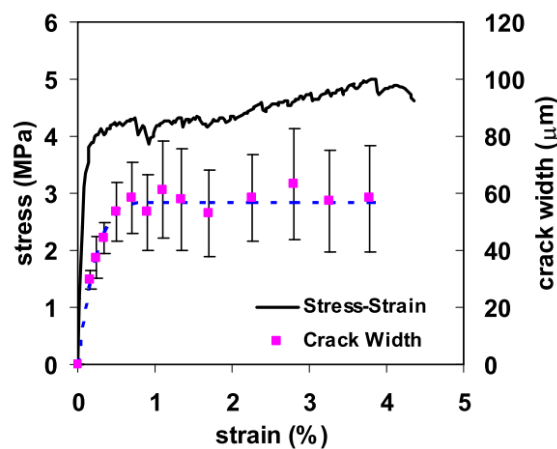
Figure 1.2   Typical tensile stress-strain crack width relationship of SC-ECC (Yang et al. 2008).

Originating in the 1980s, the strain-hardening response of several HPFRCC materials in tension was only achieved by utilising a relatively large amount of fibres (generally more than 5% by the volume fraction of steel fibres). Lankard (1984) introduced slurry infiltrated fibre concrete (SIFCON) using from 4% up to 20% by volume of discontinuous steel fibres to obtain high strength, high ductility and

crack/spall resistant properties. SIFCON demonstrated the ability to bear tensile stress up to nearly 30 MPa while the strains at peak stress ranged from 1% to 2% (Naaman & Homrich 1989). Due to a large volume of implemented fibres, which causes the mixing and casting to become hugely difficult or impossible. First, fibres have to be replaced in a mould, and then cement-based slurry infiltrates the fibre network. Slurry infiltrated mat concrete (SIMCON) is another similar approach and process, but with continuous steel fibre-mats put into the form. The ultimate tensile strength of SIMCON is up to 17 MPa, while the corresponding strain is between 1 to 1.5%, using more than 5% by volume of steel fibres (Hackman et al. 1992). However, these materials' application is greatly restricted due to the high price of steel fibres as well as demands made on in-situ construction.

By contrast, ECC, which was originally developed by a group of researchers at the University of Michigan, exhibits a reasonable tensile strength capacity of about 5 MPa and the tensile strain capacity in excess of 5% with a moderately low synthetic fibres fraction (Figure 1.2). Furthermore, the compressive strength of ECC is in the range of typical high strength concrete (Li 1998). To date, experimental investigations have demonstrated the advantage of ECC over normal concrete at the structural scale level such as in joint beam-column under cyclic loading (Pan & Yuan 2013; Yuan et al. 2013; Qudah & Maalej 2014), and in steel-reinforced ECC (R/ECC) (Shimizu et al. 2004; Wu et al. 2017; Xu et al. 2017). Moreover, ECC has proven ability to diminish or even obliterate the need for shear reinforcements in R/ECC elements due to its high shear strength capacity (Qudah & Maalej 2014). The compatible deformation of ECC with steel reinforcements also leads to high structural damage tolerance and deformability (Li 2008).

1.1.2 Micromechanics approach of ECC

It is worth mentioning here that one of the most advantageous properties of ECC is its high tensile ductility with moderate fibre volume content, making ECC cost-effective for the construction industry as well as flexible enough for in-situ processing. This is largely due to the micromechanics approach in ECC. Micromechanical models served as useful tools for systematically tailoring microstructures and optimising constitutive materials of ECC. The pioneer research on micromechanics of random short fibres reinforced brittle cementitious matrix can be traced back to the works of Aveston & Kelly (1973) and Marshall & Cox (1988). Subsequently, two micromechanics criteria to attain the multiple flat-cracking modes and strain-hardening behaviour were determined (Li & Leung 1992). The first condition, known as strength criterion, aims to control the initiation of cracks, i.e., the tensile cracking strength of matrix σ_c must not surpass the ultimate bridging strength of fibres σ_0. This condition ensures the bridging fibres can sustain the tensile stress release from cracked matrix, which normally commences from defect sites (pre-existing internal flaws). This criterion prevents the instant failure mode after the first crack occurs in the matrix. The second condition, known as energy criterion, is the fundamental requirement to govern the steady-state mode of flat crack propagation. The crack tip toughness J_{tip} has to be less than the complementary energy J_b' of the bridging fibres as can be seen in Figure 1.3. In this way, the crack is able to propagate while the crack opening remains constant. The bridging fibres bear and transfer stress to the surrounding matrix without weakening and fracturing. A further micro-crack begins at another defect site and subsequent flat crack propagation as more load action arises (Li 2003). The satisfaction of these conditions is

necessary to form multiple steady-state cracks, which results in the strain-hardening behaviour of ECC.

$$J_b' \equiv \sigma_0 \delta_0 - \int_0^{\delta_0} \sigma(\delta)d\delta$$

$$\sigma_{ss}\delta_{ss} - \int_0^{\delta_{ss}} \sigma(\delta)d\delta = J_{tip}$$
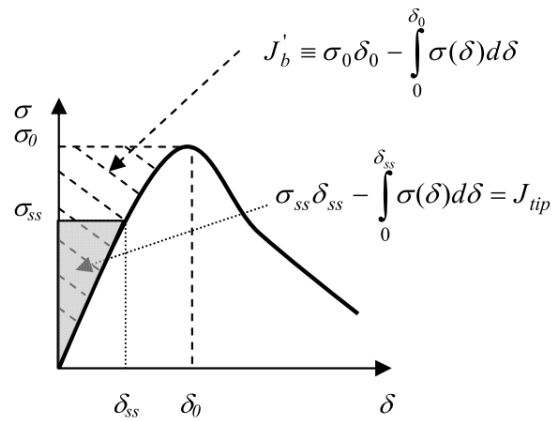
Figure 1.3   Typical tensile strain-hardening σ - δ curve. Hatched zone signifies the complementary energy J_b'. Shaped zone signifies the crack tip toughness J_{tip} (Yang et al. 2008).

As observed in Figure 1.3, the stress-crack opening (σ – δ) relationship represents the properties of fibre-bridging across a matrix crack with reference to both criteria to form the strain-hardening response of ECC. The σ - δ relationship, consequently plays a vital role in controlling the tensile strain-hardening behaviour of ECC (Yang et al. 2008). Lin et al. (1999) indicated that the fibre properties and fibre/matrix interaction are those factors that govern the shape of the σ-δ curve in ECC. These understandings provide guidelines for tailoring the properties of fibres, matrix and fibre/matrix interface to improve the robustness of high tensile strength, and high tensile ductility of ECC. Two indispensable criteria to form multi-crack under tension, i.e., control the initiation of cracks (strength criterion) and ensure the appearance of steady-state flat-crack propagation (energy criterion) are attained with just around 2% volume fraction of synthetic fibres (Li 2003). For instance, the application of plasma treatment has enhanced the interface bond strength of the very high tensile strength polyethylene (PE) fibres exhibiting low bond properties. This in turn, has led to high tensile performance

of PE-ECC with low fibre volume fraction (Li et al. 1996). In contrast, reducing the interfacial chemical and frictional bond by oiling agent has confirmed the efficiency with the moderate strength polyvinyl alcohol (PVA) fibre exhibiting high chemical bond (Redon et al. 2001; Li 2002; Li et al. 2002). Matrix tailoring with fine aggregates (Li et al. 1995), the blast furnace slag (Kim et al. 2007; Zhou et al. 2010), high volume of fly ash (Wang & Li 2007; Yang et al. 2007) also illustrated an improvement in the fibre/matrix interaction. The end result was an enhancement in the robustness of tensile behaviour of ECC.

Through micromechanics tools, ECC properties are tailorable and form a range of ECC material for different purposes augmented by common high tensile performance and multiple fine cracking. Different groups of ECC are named in the literature based on their dominant characteristics such as self-consolidating or flowable ECC (Kong et al. 2003b; Lepech & Li 2008), self-healing ECC (Li, Lim, et al. 1998; Wu et al. 2012), self-sensing ECC (Lin et al. 2011; Huang, Li, et al. 2018) or ECC using local ingredients (Ma et al. 2015; Meng, Huang, et al. 2017). In recent times, the development of ECC is still contributed by researchers worldwide. For example, a new type of ultra-high performance ECC has been developed recently (Yu et al. 2018). The obtained tensile strength and tensile strain of UHP-ECC, which utilising PE fibres, is up to 20 MPa and 8.7%, respectively. Besides, self-reinforced ECC has also established to combine with 3D printing technology for building-scale applications (Soltan & Li 2018; Zhu et al. 2019). This printable ECC is a promising material for full-scale 3D printing processes as steel reinforcement, one of the major obstacles in this automated manufacturing technique, can be eliminated in printed structures (Li et al. 2020).

1.2 The Role of Fibre Orientation and Distribution on Tensile Behaviour of ECC: A Multiscale Consideration

The tensile strain-hardening behaviour of ECC is achieved though the steady formation of multiple flat cracks at different defect zones in the matrix. From the micro to macroscale considerations (Kabele 2007; Kang & Bolander 2015; Huang et al. 2016), the distribution and orientation of fibres have emerged as the two vital factors that govern the relationship of the tensile stress-crack opening of a single crack, and thus strongly affect the tensile stress-strain behaviour of ECC. Therefore, a detailed literature review of fibre distribution and orientation and their impact on the mechanical behaviour of ECC at different length scales will be presented in the following sections.

1.2.1 Pullout behaviour of an inclined fibre at the microscale level

At this length scale, influence of the inclination on the pullout behaviour of an inclined fibre from the cementitious matrix was studied (Nak-Ho & Suh 1979; Li et al. 1990; Ouyang et al. 1994). Basically, an arbitrary fibre must be debonded from the surrounding matrix before being pulled out. While both stages are in progress, the snubbing phenomenon associated with the inclined fibre has occurred (Li et al. 1990; Wu & Li 1992) (Figure 1.4a). Li et al. (1990) supposed that the deformation of inclined fibre took place completely around its exit point. The inclined pullout fibre then was considered as a string passing over a small frictional pulley. The ultimate pullout load of an inclined fibre was estimated by magnifying the peak pullout load of a non-inclined fibre with a snubbing factor. By assuming the snubbing factor to be constant for all debonding length and pullout distance, the relationship between bridging force and displacement of inclined fibre was derived. This snubbing friction model was then

applied to estimate the mechanical behaviour of ECC in direct tension (Li et al. 1991; Leung & Li 1992; Wu & Li 1992) and bending (Maalej & Li 1994).

However, the snubbing effect also reduced the critical fibre embedment length leading to premature fibre failure, which then strongly undermined the bridging behaviour of fibre (Li 1993; Maalej et al. 1995). Leung & Ybanez (1997) developed a new snubbing model, considered the matrix spalling around the exit point of the pullout of inclined fibres (Figure 1.4b). This model also deliberated the increase of interfacial friction, resulting in a good agreement with the experimental outcomes. The later work of Kanda & Li (1998) found that fibres with a larger inclined angle tend to rupture more than the smaller ones due to the decline in its apparent strength. The apparent strength-reduction factor $f^{'}$ to be approximately 0.3 was then proposed. Similarly, Zhang & Li (2002) stated that the rupture load of an inclined fibre was significantly reduced in comparison with an aligned fibre. This was because of the bending effect occur when the inclined fibre be pulled out of the matrix.
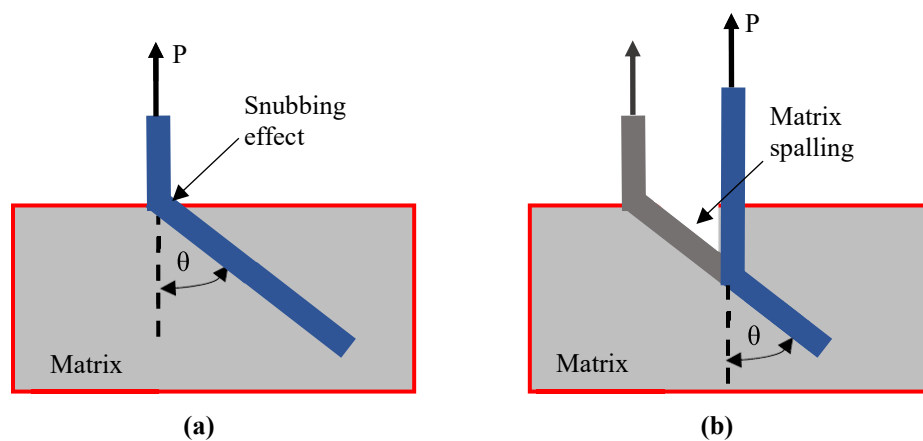
Figure 1.4 (a) Snubbing effect; (b) Matrix spalling of an inclined fibre.

1.2.2 Fibre-bridging consecutive law at the lower mesoscale level

As shown in Figure 1.5, the lower mesoscale looks into details of the behaviour of the numerous fibres bridging an individual crack. When a crack is formed in the matrix, all intersected fibres at that crack will bear the stress released by the matrix. The capability of these bridging fibre to first sustain and then steady transfer the stress to the surrounding matrix is primarily important in forming multiple micro-cracks at the upper mesoscale, resulting in the strain-hardening behaviour of macroscopic material properties of ECC (Kabele 2007). Therefore, the crack bridging strength versus the crack opening σ - δ relationship has played an essential role since it links the properties of matrix, fibre and matrix/fibre interface at the microscale level with those of the macroscopic composite. A well-controlled crack bridging behaviour is crucial in achieving high tensile strength and strain capacity of ECC.
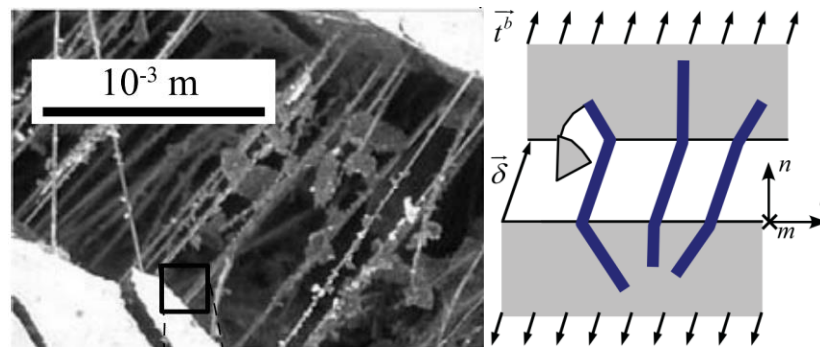
Figure 1.5   Lower mesoscale level of fibres bridging crack in ECC (Kabele 2007).

The σ – δ curve of a crack is characterised by the performance of individual bridging fibre at that crack plane. Since the 1990s, several research attempts have been dedicated to forming the bridging consecutive law models accounting for the difference of fibre/matrix interface properties and the difference of fibre rupture modes. The original fibre-bridging models (FBM) have been established through considering the

random orientation of fibre, snubbing effect of fibre and fibre slip-hardening interface. These FBM were based on the constitutive interface relationship and the micromechanical models of a single fibre pullout (Leung & Li 1992; Li & Leung 1992; Lin & Li 1997). However, these models, have not considered the rupture of fibres when bearing stress. In fact, the rupture of fibres might occur at both the debonding or pullout period, on condition that the tensile stress is greater than their apparent strength, which might be significantly reduced in inclined fibres (Maalej et al. 1995; Kanda & Li 1998).

Due to the slip-hardening behaviour, experimental studies have shown that the ultimate bridging stress of fibre being pulled out the matrix could be much larger than that at the end of the debonding period (Li et al. 2002; Yang et al. 2008). Therefore, the rupture tends to happen at the pullout stage with fibre exhibiting strong slip-hardening interface behaviour such as PVA fibre. Besides, fibre slippage might appear at both short and long embedded sides of bridging fibres due to the behaviour of fibre slip-hardening interface. Thus, the accurateness of stress-crack opening prediction from FBMs considering the two-way fibre pullout and fibre rupture has been improved (Yang et al. 2008; Huang et al. 2015) (Figure 1.6).
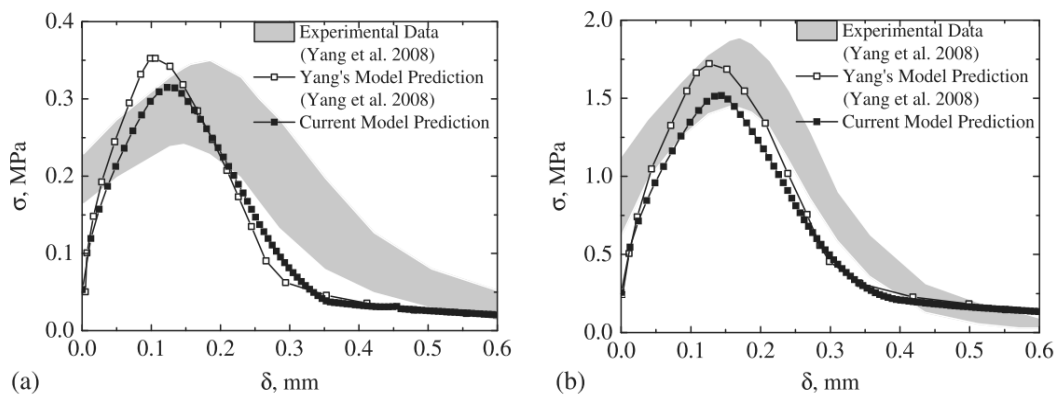
Figure 1.6   Model prediction and experimental data of σ-δ curve with different fibre volume fraction: (a) Vf = 0.1%; (b) Vf = 0.5% (Huang et al. 2015).

The influence of the fibre orientation distribution on the prediction of FBM was also investigated. Lee, Lee, et al. (2010) and Lee, Kim, et al. (2010) attempted to improve the accurateness of FBM by obtaining the distribution of fibre orientation and the number of fibres in ECC specimens rather than using the assumption of fibre orientation distribution occurring in two or three dimensions as in previous models. They used the image analysis to quantify the fibre orientation distribution in specimens, then implemented into the FBM to obtain the $\sigma - \delta$ curves. The obtained peak tensile strength from this model approach showed a 15% error with the experimental results, much less than 50% of the ultimate tensile strength obtained by assuming two or three dimensions distribution of fibre orientation. The better prediction in this model approach was then mentioned as a consequence of the influence of flow direction or size of specimens on the distribution of fibre orientation, which could not be considered in probabilistic FBM model. In the later work of Kanakubo et al. (2016), the effect of casting direction on fibre orientation distribution, which then influences the bridging performance of PVA-ECC was also examined. The water glass solution served to simulate the casting process of a self-consolidating ECC with two different casting directions. The obtained $\sigma - \delta$ curves of FBM illustrated the different effects of fibre orientation distribution in different simulations on the bridging performance of fibres. The efficiency of fibre in bearing stress at a crack plane released by the matrix, thus strongly depends on the number of intersected fibres and their orientation at that plane.

1.2.3 Inhomogeneous fibre distribution at the macroscale level

From the influences of fibre orientation on pullout behaviour at the microscale and the distribution of fibre orientation on the $\sigma - \delta$ relationship at the lower mesoscale, the distribution and orientation of fibres are recognised as crucial factors, which influence

the mechanical performance of ECC at the higher length-scale. At the macroscale level, together with the distribution of matrix flaw sizes, the non-uniform distribution of inclined fibres in the matrix has significantly varied the tensile behaviour at different parts of ECC specimen (Li et al. 1995; Ranade et al. 2012; Tosun-Felekoğlu et al. 2014; Ding et al. 2020). Therefore, it is essential to understand the orientation and distribution of fibre in cementitious matrix and their influence on macroscopic properties of ECC. Hitherto, it is not straightforward to investigate the distribution and orientation of synthetic fibres commonly used in ECC owning fine diameter (ranging between 0.01-0.04 mm) with lower contrast than the cementitious matrix. Torigoe et al. (2003) have tried to use the fluorescence technique, which was commonly used in biomedical fields, to capture PVA fibres with a charge-coupled device (CCD) camera through a microscope. The PVA fibres were observed as green to yellow dots in the cross-sections of the composite through the Green Fluorescent Protein (GFP) filter. Lee et al. (2009) after that enhanced this technique by employing a series of processes based on categorisation, watershed segmentation, and morphological reconstruction in the image processing phase (Figure 1.7). Another effective method was proposed by Felekoğlu et al. (2015), using a scanning electron microscope (SEM) of micro-images at backscattered electron mode (BEC) to investigate the distribution of polypropylene (PP) fibres. Through these techniques, the inhomogeneous distribution of inclined fibre could be observed in the surface of a cross-section as is depicted in Figure 1.7.
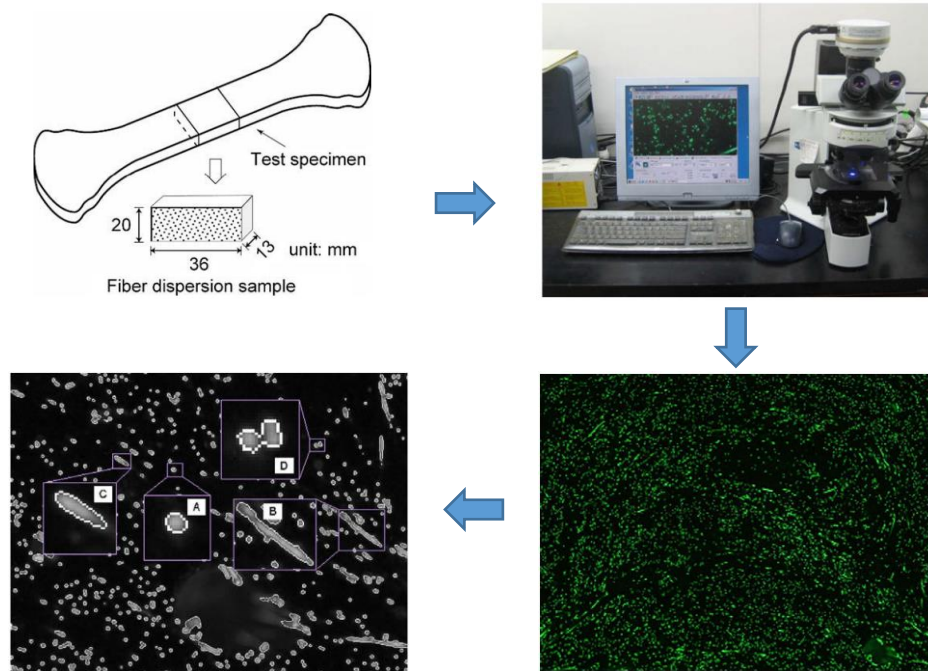
Figure 1.7 Schematic evaluation technique of PVA fibre dispersion (Lee et al. 2009).

Several attempts have been made to enhance the dispersion of fibres in the mixture of ECC. Rheology-control of ECC mortar has proven ability to escalate the dispersion of fibres, then improve the tensile properties of ECC (Yang et al. 2009; Şahmaran et al. 2013). Li & Li (2013) used the Marsh cone flow time as a simple tool to measure and control the rheology of the mortar before adding PVA fibres. An optimal range of Marsh cone rate between 24s and 33s was suggested to achieve better fibre dispersion and higher tensile strain capacity. Zhou et al. (2012) divided the mixing of solid materials with the liquid into two-phase, and the fibres were added between two steps to improve the dispersion of PVA fibre in the fresh mix of ECC. Then, the obtained fibre distribution coefficient increased up to 24% in comparison with standard mixing sequence. As a result, the tensile strain and ultimate tensile strength was 50 times and 14% higher than those of the traditional mixing of ECC, respectively. Also, the influence of fibre orientation distribution on the tensile performance of ECC specimens, considering

casting direction or sizes of specimens was illustrated via experimental studies (Ding et al. 2020; Yu et al. 2020).

However, these above techniques required the image processing and analysis procedures to evaluate the fibre dispersion and orientation quantitatively. Although image analysis is a trusted and well-studied method, it is incredibly time-consuming. Thus, the overwhelming approach is to cut tested specimens at the major cracking position or near the fracture zone only, to obtain the fibre orientation and distribution factors. Then, the obtained fibre orientation and distribution information at those sections was used to correlate with the mechanical performance of ECC specimens. Moreover, the size of tested or cut specimens has to be small enough to suit with the employed equipment, i.e., the microscope. These drawbacks tend to narrow the application of these methods, especially at an industrial scale.

1.3 Self-Consolidating (or Flowable) ECC

For cementitious materials, inadequate vibration or compaction at the fresh state could compromise the material quality and durability of structural elements as air is considerably trapped inside the cementitious matrix. Therefore, the implementation of internal or external vibration when casting fresh cementitious materials is required as an inevitable phase. However, this task becomes more challenging for normal ECC due to the disqualification of coarse aggregates and the incorporation of fibres into the fresh mortar. Basically, the vibration is required at a high-frequency level for moulding fresh mixtures into formworks, ensuring the sufficient consolidation of fresh normal ECC (Li, Kong, et al. 1998). Moreover, non-uniform distribution of fibres due to low workability of fresh ECC mixture might also reduce the fibres' efficiency.

In the meantime, since the invention of the self-consolidating or self-compacting concrete (SCC) in Japan in the 1990s, its application in industrial construction has been adopted as means to improve the durability and quality of concrete structures (Okamura & Ozawa 1995; Ozawa 1995). The capability of SCC to thoroughly compact under its self-weight has made this invention one of the outstanding revolutions in concrete technology in recent decades due to the enhanced material performance and working environment. SCC has high fluidity properties which help it to occupy every corner of the formworks, even with complexity shape of formworks, without the need of external efforts such as using compaction vibrators, poking, etc. Also, the application of SCC in the building industry has led to several good outcomes such as reduced noise pollution and labour costs, better productivity, etc. The development and successful application of SCC were the motivation for the evolution of a new type of ECC that can be self-consolidating in the fresh state but still possess its unique intrinsic property, i.e., high tensile ductility in the hardened state (Li, Kong, et al. 1998).

1.3.1 Development and application of self-consolidating (flowable) ECC

A group of researchers at the University of Michigan has developed the self-consolidating (SC) or flowable ECC by combining the constitutive micromechanics design and rheological control of fresh mortar (Li, Kong, et al. 1998; Kong et al. 2003b; 2003a). In these studies, ingredients of the cementitious matrix were tailored to obtain the desired flowability, while respecting the criteria for achieving the strain-hardening behaviour of ECC. A strong polyelectrolyte (a superplasticiser) has been optimised in conjunction with a non-ionic polymer to achieve high fluidity of fresh mortar and effectively controls the aggregation and segregation of the cement particles and fibres suspension.

Large-scale production procedures and the tensile properties of this member of ECC have also been studied (Fischer & Shuxin 2003; Kanda et al. 2004; Lepech & Li 2008). Kanda et al. (2004) conducted research on eleven batches ranging from 0.3 to 0.8 m^3 in size using one cubic meter Omni-mixer at a concrete prefabrication manufactory with different ambient weather conditions. The tested results at the fresh state and hardened state illustrated the self-consolidating and strain-hardening properties of this ECC material. Lepech & Li (2008) performed an investigation at a larger scale up to 3 m^3 batch at a commercial plant and transited by mixer trucks. This study results have shown that the capacity of compressive strength, tensile strength and tensile strain of SC-ECC (called ECC-M45) can be designated at 60 MPa, 4.35 MPa, and 2.0%, respectively (Lepech & Li 2008). In general, SC-ECC used fine silica sand, which has a maximum grain size of 250 μm with a mean size of 110 μm, and the sand to binder (cement and fly ash) ratio of 0.36 to maintain adequate stiffness and volume stability (Li 2008). The general-purpose Portland cement made by Cement Australia Pty. Ltd. and ASTM fly ash; type F is utilised. The mixture proportions by weight of SC-ECC (flowable ECC or ECC-M45) using PVA fibre, which was developed for large-scale on-site construction applications are given in Table 1.1.

Table 1.1 Mix proportion by weight for SC-ECC (ECC-M45) (Lepech & Li 2008).

Mix	Cement	Fly ash	Fine sand	Water	HRWR*	Fibre, vol %
SC-ECC (ECC-M45)	1	1.2	0.8	0.56	0.012	0.02

(*) polycarboxylate-based high range water reducer

Self-consolidating or flowable ECC has been applied in real-scale structural members such as bridge deck link slabs in Michigan, USA as shown in Figure 1.8a

(Lepech & Li 2009). Another application utilised pre-cast SC-ECC coupling beams of two high-rise RC buildings in Japan acting as dampers in core walls to absorb the seismic energy (Maruta et al. 2005) (Figure 1.8b). The capability of this approach was illustrated as no visible damage being observed in these two buildings after experiencing a strong earthquake on 11th of March, 2011 (Kanda et al. 2011).

(a)   **(b)**
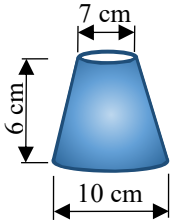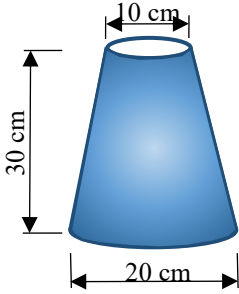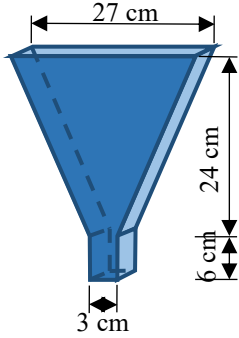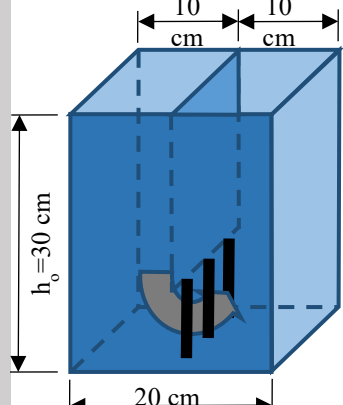
Figure 1.8 Application of SC-ECC: (a) Link slabs of bridge deck in Michigan, USA (Lepech & Li 2009); (b) Coupling beams in the core region of multi-storey structures in Japan (Maruta et al. 2005).

1.3.2 Workability and rheology of fresh self-consolidating ECC

Being primary properties, the self-consolidating characteristics of fresh ECC have to be quantified and evaluated after the mixing process is completed. In both laboratory and field practice, the workability of fresh SC-ECC is tested before casting the fresh mix into formworks by using several standard tests. In the studies and establishments of SC-ECC, V.C. Li and his associates applied similar methods for testing fresh SCC which were proposed by Ozawa (1995). These tests include the deformability tests using slump cone flow, flow rate test using a V-funnel device, and self-placing test using a U-box

device with reinforcing steel as obstacles to SC-ECC flow. The geometry, dimensions,

functionality of each device and the corresponding indices are given in Table 1.2.

Table 1.2 Test devices for fresh SC-ECC.

Test	Shape and dimensions of devices	Type of measurement	Flow index
Deformability test I (mini-cone flow test)	7 cm / 6 cm / 10 cm	Diameter of the spread, $\bar{d}_1$ (cm) and time t_1 when flow stop (sec.)	$\Gamma_1 = \dfrac{\bar{d}_1^2 - \bar{d}_0^2}{\bar{d}_0^2}$
Deformability test II (Slump flow test)	10 cm / 30 cm / 20 cm	Diameter of the spread, $\bar{d}_2$ (cm), time t_{500} and t_2 when flow stop (sec.)	$\Gamma_2 = \dfrac{\bar{d}_2^2 - \bar{d}_0^2}{\bar{d}_0^2}$
Flow rate test (V-funnel test)	27 cm / 24 cm / 6 cm / 3 cm	Time for material completely vacate from the outlet, t *(sec.)*	$R = \dfrac{10}{t}$
Self-placing test (U-box test)	10 cm / 10 cm / h_o = 30 cm / 20 cm	Height of material reach in the next chamber h (cm), time t when flow stop (sec.)	$L = \dfrac{2h}{h_0}$

1.3.2.1 Slump flow test

The slump flow test is a simple, rapid and feasible method that can characterise and quantify the deformability, flowability of fresh self-consolidating ECC. To evaluate those properties of flowable ECC, both the mini cone and normal cone slump flow are employed. After being fully filled with fresh mix, the cones are lifted up for the fresh mix collapse freely under its own weight, and then spreads horizontally without any obstructions except the frictional resistance of flat base. The measured diameters of the spread are used to determine the deformability index of ECC (Figure 1.9).

Figure 1.9   Measuring the diameter of flowability ECC of a slump flow test (Li 2008).

1.3.2.2 V-funnel test

The V-funnel device has served to test the flow rate and filling ability of fresh ECC. The funnel is fully filled with fresh mixture and then the lid at the funnel bottom is removed to allow fresh ECC dribble through the funnel-outlet (Figure 1.10). The recorded time from starting to when the material particles completely vacate the bottom outlet of the funnel is utilised to calculate the flow rate index of flowable ECC. For SCC, Ozawa (1995) concluded that the allowable values of flow rate index, R, ranging from

0.8 to 1.2. In general, a low flow rate index value specifies a low filling ability of fresh mixture and vice versa. Also, the results of the V-funnel test could be used to indicate plastic viscosity of the fresh mixture. Short flow time indicates low plastic viscosity of the mixture (Okamura & Ouchi 2003; Lashkarbolouk et al. 2014).

Figure 1.10   Setup for V-funnel test (Okamura & Ouchi 2003).

1.3.2.3 U-box test

The U-box is a useful device to verify the self-placing or self-consolidating of fresh ECC, and to examine the ability of fresh material to pass through narrow spaces between steel reinforcements. After filling one chamber with fresh ECC, the gate located between two champers is lifted for the fresh mix to flow horizontally to the adjacent chamber. In this test, the mortar and fibres have to pass through the steel bars successfully before moving to the next chamber. The height of fresh ECC in the initial empty- chamber when the flow stops levelling is measured to calculate the self-consolidating index of the fresh mix (Figure 1.11). Correspondingly, Nagamoto & Ozawa (1997) have suggested a range value of 0.7 to 1 for the self-placing index of SCC.
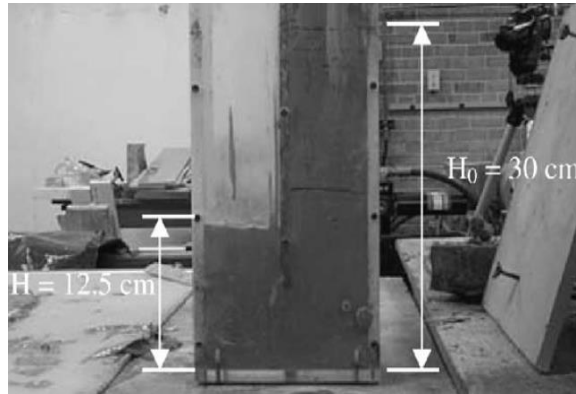
Figure 1.11 U-box device for testing self-placing ability of SC-ECC and measuring the results (Kong et al. 2003a).

1.3.2.4 Beneficial and drawbacks of workability tests

Generally, the results from these above workability tests are beneficial for:

- Evaluation the flowability, filling and passing abilities of fresh ECC mixtures.

- Visual inspection of the cohesiveness between material ingredients, whether or not the aggregation and segregation between fibres suspension and cementitious matrix during their flow occurs.

- Estimating the plastic viscosity of fresh ECC, which could not be accurately measured in FRCs materials when using rheometers (Ghanbari & Karihaloo 2009).

However, there is no double that these tests have to be repeated for different mixtures and, consequently, it is costly and labour-intensive. More importantly, the understanding and/or observation of fibres' movement in the fresh mixture during the testing processes, which might help to envisage the distribution and orientation of fibres in the matrix of elements, is unachievable.

1.4 Motivation and Objectives of this Research

1.4.1 Motivation of this research

Since fibres are incorporated into cement-based materials, the crucial influence of fibre dispersion and orientation on the variation of mechanical properties of FRCs have been proved by intensive studies. The differing fibres/matrix interactions due to non-uniform distribution and orientation of fibre have led to the large variations of mechanical performance of FRCs at different locations and even casting within the same mixture (Kang & Kim 2011; Zerbino et al. 2012; Maya Duque & Graybeal 2016; Sarmiento et al. 2016; Zhou & Uchida 2017a; 2017b). The ability to evaluate or predict fibre distribution orientation within the FRCs mixtures will make it possible to control the quality and noticeably reduce the scale of variations of FRCs' performance. This, in turn, ensures the structural performance of FRCs that is essential for design and construction using FRCs. However, the distribution and orientation of fibres are complex and influenced by diverse factors. Fibre orientation and distribution can change throughout the manufacturing process of the FRCs, from the mixing procedure to the casting into the formwork. The distribution of fibres is mainly influenced by the fresh properties of FRCs (Li & Li 2013; Meng & Khayat 2017; Wang et al. 2017; Ahmad & Umar 2018) or mixing procedure (Zhou et al. 2012; Sassani et al. 2017). Meanwhile, several other factors considerably affect the orientation of fibre. For a number of self-compacting FRCs, wall effects (Švec et al. 2014; Huang, Su, et al. 2019) and flow-induced (Boulekbache et al. 2010; Ferrara et al. 2011; Zhou & Uchida 2017a), which in turn depend on the geometry of the element and the rheology of the material respectively, are experimentally identified as the two dominating factors affect the

orientation of fibre. Casting techniques such as casting locations and casting directions have also shown significant effects on the fibre orientation distribution (Torrijos et al. 2010; Van Mier et al. 2013; Maya Duque & Graybeal 2016; Abrishambaf et al. 2017; Zhou & Uchida 2017a; Huang, Gao, et al. 2018; Song et al. 2018; Ding et al. 2020).

For the aforementioned experimental studies, image analysis programs have been used for analysing cross-sections of fibres at the fracture surface or cutting sections of tested specimens to determine the fibre dispersion and orientation. Due to the time-consuming nature of this approach, only one or a few sections of tested specimens were studied. Although the obtained fibre orientation and distribution at cutting sections have shown a correlation with the mechanical properties of specimens, it is necessary to understand fibre orientation and distribution at different parts of specimens. For this aspiration, the numerical method is advantageous for investigating and predicting the orientation distribution of fibres in the FRCs member. Various numerical models have been devised for modelling the flowable FRCs. Particle-based or mesh-free methods, in which the entire computational domain is separated by distinct particles, have been illustrated their dominance in solving the governing equations referring to the large deformation of fresh self-compacting FRCs flow (Svec et al. 2011; Kulasegaram & Karihaloo 2013; Deeb, Karihaloo, et al. 2014). In these approaches, changes in fibre movement and orientation are easily monitored during its flow. These studies have contributed to the improvement of fibre dispersion and orientation, resulting in enhanced mechanical behaviour of FRCs structural elements. However, investigations on the distribution and orientation of fibres so far have mainly focused on rigid fibres such as steel fibres in FRCs.

On the other hand, synthetic fibres commonly used in ECC are flexible fibres that could be bent or coiled in the mix during the flow of fresh ECC, especially self-consolidating ECC. This phenomenon might significantly affect the distribution and orientation of fibres in the specimens, resulting in the variation of mechanical performance of ECC at structural scale, and has not yet been studied in the literature. Also, investigation of fibre orientation and distribution at the cutting surface could not provide the data of how synthetic fibres are bent in ECC matrix. So far, the bending of synthetic fibres was only observed by using the transparent model of concrete to perform the casting of self-compacting FRCs (Van Mier et al. 2013; Kanakubo et al. 2016; Zhou & Uchida 2017a). Therefore, a novel method to investigate the distribution and orientation of bendable synthetic fibres in ECC, especially at its fresh state, is highly desired. The improved understanding of the fresh ECC flow characteristics is beneficial to enhance the distribution and orientation of flexible synthetic fibres, achieving the desired strength of ECC structural members.

It is worth noting that the principal advantage of the simulation approach is that it can capture the flow behaviour of self-compacting FRCs, providing insights into the motion of fibres during their flow and therefore providing a fulfilling understanding of the distribution and orientation of fibres in the mixture's fresh state. Furthermore, the correlation between fresh-state properties, i.e., the rheology of fresh mix with fibre distribution orientation, can be feasibly investigated. Moreover, the numerical approach is cost-effective and can replace the expensive experimental procedure in the laboratory, which helps to save time, effort and materials. Nonetheless, one shortcoming associated with the simulation method is the prolongation of computational time. However, modern

high-performance computers with serial, parallel and dual computing capabilities could help to solve this problem.

1.4.2 Research objectives

The aim of this PhD research is to model the flow behaviour of ECC and then investigate the distribution and orientation of flexible synthetic fibres and their effects on the tensile performance of ECC material. To achieve these goals, a numerical model is firstly developed to simulate the flow of fresh ECC for obtaining the real picture of ECC flow as well as the distribution and orientation of flexible synthetic fibres in the cementitious matrix of fresh ECC. The numerical model focuses on the flow characteristics of self-consolidating ECC. The simulation results are then validated with reported experimental studies on fresh self-consolidating ECC. At the hardened state of ECC, predicting the stress-crack opening relationship at the lower mesoscale is the main concern. Several fibre-bridging constitutive models of ECC have been developed and improved the prediction results by considering the two-way pullout of fibre. However, the results from those models still show a notable difference in comparison with the experimental findings. Thus, improving the accuracy of FBM is also stressed. Finally, the tensile performance of ECC can be numerically estimated through a consideration of two states of ECC.

Specifically, the objectives of this research are to:

- Develop a numerical model based on a mesh-free method to simulate the flow of fresh ECC in two-dimension and three-dimension contexts, in order to investigate its flowability, filling and passing ability. The model makes it

possible to simulate and track the motion of flexible synthetic fibre in the fresh ECC.

- Propose a simple technique for evaluating the distribution and orientation of flexible synthetic fibre in ECC.

- Investigate the bending phenomenon of flexible synthetic fibre in ECC and its influence on the distribution of fibre orientation.

- Develop a new fibre-bridging law model to accurately predict the stress-strain relationship of a single crack at the lower mesoscale level of ECC.

- Propose an innovative approach, which can incorporate the information of fibre distribution and orientation from the simulation of fresh ECC flow with the fibre-bridging law model to estimate the tensile behaviour of ECC material.

1.5 Outline of the Thesis

The contents of this thesis are organised into seven chapters, and they are summarised as follows.

The first chapter presents the background information on the historical development of ECC materials. The effects of fibre distribution and orientation on the tensile behaviour of ECC at the three-scale levels are then reviewed. The development of flowable ECC and the gaps in our knowledge on this subject, which are the motivation and objectives of the thesis, are explained in this chapter.

In Chapter 2, a brief review of preceding efforts for modelling flowable FRCs materials is first provided. Then, a typical computational strategy to model the flow

behaviour of self-compacting FRCs is clarified. Finally, the details of numerical scheme from the governing equations of viscous fluid to the incorporation of the Lagrangian particle-based smoothed particles hydrodynamics (SPH) for approximately solving the constitutive equations. The SPH is presented in detail, including its general concept, interpolant smoothing kernels, boundary conditions and methods to solve the pressure and mass term in governing equations of viscous fluid. Moreover, the rheology models to describe the viscous fluid are introduced.

Chapter 3 presents the development of a numerical model for simulating the flow of SC-ECC, which is described as a non-Newtonian viscous fluid, in two dimensions. Flexible synthetic fibres in the SC-ECC are modelled as separate particles in the computational domain, which possess identical continuum properties as mortar particles apart from the drag force between two adjacent fibre particles. The simulation of slump flow tests is conducted to confirm the effectiveness of the proposed model. The model results are comparable with the experimental data obtained from reported studies in the literature. The correlations between the wall-effects, the distance of flow, the casting position with the orientation and the distribution of synthetic fibres are also examined.

In Chapter 4, a three-dimensional model is developed to simulate the flowable ECC through the V-funnel and U-box tests. The V-funnel model focuses on the flow rate characteristics and correlation of the dispersion of synthetic fibres with the plastic viscosity of fresh mixtures. The U-box simulation confirms the self-consolidating capability and passing ability of SC-ECC flow through reinforcing bars. The simulation results of the discharge time in the V-funnel model and self-levelling index in the U-box model agree well with experimental results from the literature, which provide convincing evidence on the correctness and effectiveness of the developed model. The

29

proposed model can therefore generate insights into the behaviour of flowable ECC in terms of filling, passing abilities and the dispersion/orientation of flexible synthetic fibres.

Chapter 5 investigates the effects of sample thickness on fibre orientations by simulating the casting of fresh SC-ECC into different thicknesses of moulds. A simple technique is then proposed to assess the inclination of flexible synthetic fibres at various sections of simulated specimens after the SC-ECC stop flowing in the mould. The findings offer an understanding of flexible fibre orientate in thin specimens and thick specimens. Fibres tend to parallel with the longitudinal direction of specimens at the bottom of the formwork and rotate freely at the top surface of specimens.

Chapter 6 presents a novel approach, aiming to link the fresh state properties with the strain-hardening behaviour via connecting the distribution and orientation of fibres in the matrix of specimens with the micromechanics of ECC. For this purpose, the SPH method is combined with a fibre-bridging model, which is newly developed based on the stress-displacement relationship of an inclined fibre-bridging crack. The obtained orientation/distribution of fibres through simulating the moulding process by SPH are incorporated into the bridging law model to acquire the peak bridging stress at multi-vertical sections along the specimen. The distinct effects of fibre distribution and fibre orientation on the tensile behaviour of ECC is revealed. The bending of flexible synthetic fibre during the flow of the moulding process and its influence on the orientation distribution are also exposed and revealed.

Finally, Chapter 7 summarises the undertaken work as well as the main conclusions of this research. Recommendations for future research are also suggested in this chapter.

Chapter 2

Numerical Modelling Flowable Fibre-Reinforced Cement-Based Materials

2.1 Introduction

In the building industry in recent times, the application of cement-based materials with self-compacting or flowable properties has gradually replaced the ordinary concrete for ensuring the durability and quality of concrete structures. Since then, the need to understand the flow behaviour of self-compacting cement-based materials has become vital for producing the high quality of those structures. For this purpose, observation of concrete flow in the transparent formworks have been conducted (Vasilic et al. 2011; Vasilic et al. 2016). Meanwhile, for the self-compacting FRCs materials, the distribution and orientation of fibre could only be observed through the transparent model of concrete (Van Mier et al. 2013; Zhou & Uchida 2017a).

Numerical simulation, in this regard, is an appropriate approach, not only useful to reduce the costs, save labour and materials, but also provide an insight into the rheology behaviour of fresh mixture including fibre suspensions. Numerical models have the advantage of monitoring the movement of fibres, and thereby provide real information about fibres distribution and orientation during the flow. This chapter first presents a brief review of previous attempts to numerically model self-compacting FRCs flow in the literature. Then, the general numerical scheme for flow simulation of self-compacting FRCs is discussed. The latter part of this chapter concentrates on the numerical scheme details, from the governing equations of viscous fluid to the method for approximately solving those equations. General knowledge concerning the mesh-free SPH method is introduced. The rheology models to describe the non-Newtonian viscous fluid are also presented.

2.2 Previous Efforts for Modelling the Flow Behaviour of Self-Compacting Fibre-Reinforced Cement-Based Materials

In order to understand the flow characteristics of self-compacting concrete (SCC) and how implemented fibres distribute and orient in SCC flow, a number of numerical models have been proposed to model the self-compacting FRCs flow. These models offered useful tools to investigate the distribution and orientation of fibres in the matrix of fresh flowable concrete. Svec et al. (2011) were one of the first authors developing a framework to simulate the self-compacting FRCs flow. The flowable FRCs was treated as a non-Newtonian viscous fluid, including fluid particles and fibre particles. The immersed boundary method has been combined with the Lattice Boltzmann method (LBM) for modelling the interactions between fluid-fluid particles and fluid-rigid particles of fibre suspension. Algorithms for mass tracking of free surface and solving the dynamic interactions between rigid fibres were also considered. This method was then used for simulating the slump flow test of flowable FRCs as presented in Figure 2.1. This framework was also applied to examine steel fibres' orientation in flowable FRCs, and the influence of rough formwork surface was taken into account (Švec et al. 2014).

0 s   0.16 s   14.5 s
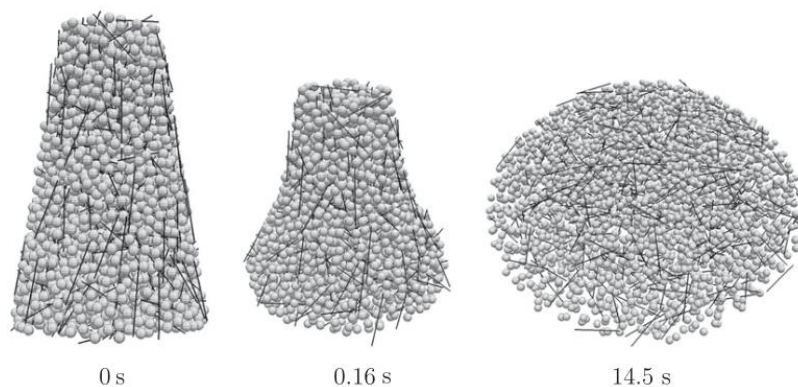
Figure 2.1   LBM for modelling slump flow test (Švec et al. 2012).

Kulasegaram & Karihaloo (2013) developed another approach to model the flow of self-consolidating FRCs by using mesh-free smoothed particles hydrodynamics (SPH) methods in two dimensions. The domain of fresh concrete and fibre was discretised on the set of particles to approximately solving the Lagrangian form of Navier-Stokes constitutive equations. The flow behaviour of fresh self-compacting FRCs was also regarded as a non-Newtonian viscous liquid, and characterised by the consecutive rheology of the Bingham model. Flowable concrete and steel fibres are represented by separated particles, which formed a homogeneous mass and possessed identical continuum properties. This 2D simulation model was then extended to a three-dimension context to simulate flow self-compacting FRCs in slump flow test (Deeb, Kulasegaram, et al. 2014b) and L-box test (Deeb, Kulasegaram, et al. 2014a) (Figure 2.2). In those studies, the steel fibres were virtually connected by two-end represent particles, and only undergo translation and rotation throughout the flow. The addition of steel fibre into the SCC mix has led to an increase in the viscosity of the cement mix-fibre suspension. For this reason, fibres have been considered as passive markers, which move and orient according to the fluid motion (Figure 2.3). A simple method has also been proposed to evaluate fibre orientation and distribution in the mixture by assessing the shapes of fibres' cross-sections (Deeb, Karihaloo, et al. 2014). Recently, Huang, Gao, et al. (2019) used a similar SPH approach to evaluate steel fibre orientations in the controlled flow of self-compacting FRCs through a small outlet funnel. Steel fibre was also treated as rigid bodies represented by two-end particles owning a haft of the fibre's mass. The influence of different placements on steel fibre orientation distribution was then investigated (Huang et al. 2020).
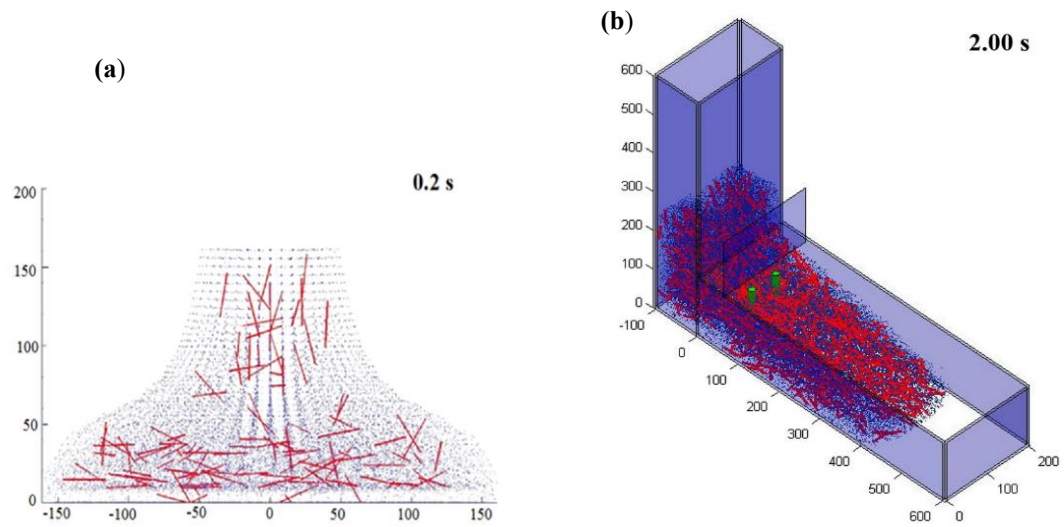
Figure 2.2 3D simulation of SFR-SCC: (a) Slump flow test (Deeb, Kulasegaram, et al. 2014b); (b) L-box test (Deeb, Kulasegaram, et al. 2014a).
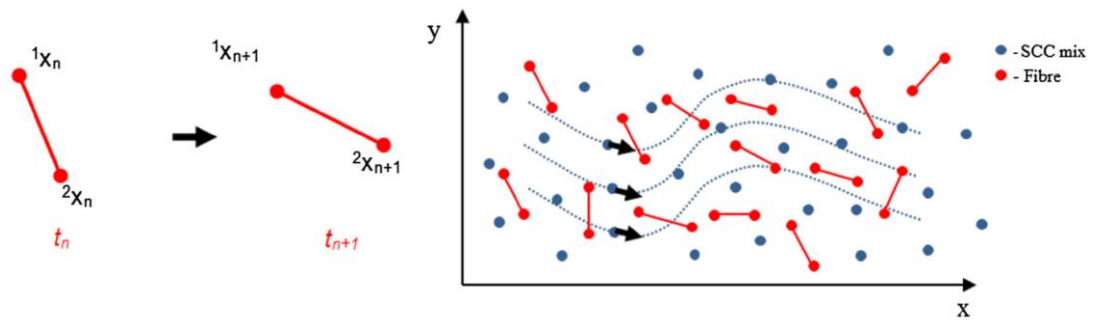
Figure 2.3 Modelling of rigid fibre orientation distributions at time step t_n and t_{n+1} (Deeb, Kulasegaram, et al. 2014b).

Bi et al. (2017) combined the computational fluid dynamics software CFX and a Matlab program to simulate the self-compacting FRCs flow. In this work, the SCC fluid was regarded as a non-Newtonian fluid and deemed to be a single homogeneous phase that was not affected by suspension fibres. The mesh-based finite volume method was implemented for solving governing equations of viscous fluid. Meanwhile, steel fibres were modelled as rigid slender rods and their rotation and translation were obligated by the flow of fresh SCC (Bi et al. 2019). The proposed method was then applied to

investigate the effect of moulding techniques on the fibre distribution and orientation (Figure 2.4). The number of fibres and their orientation could be determined at the different sections of the casted beam.
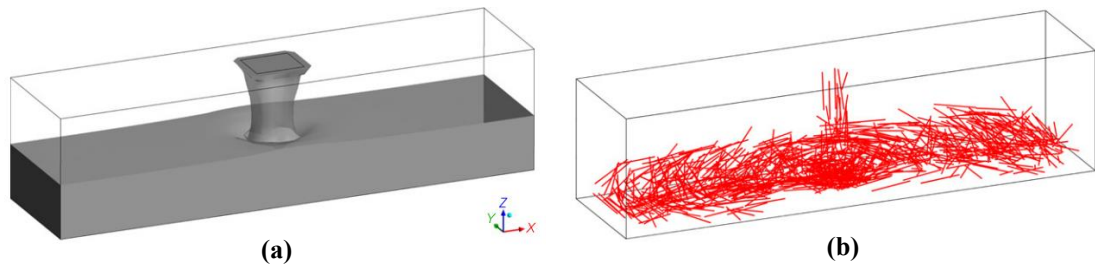
Figure 2.4 (a) The moulding simulation of SCC flow; (b) corresponding steel fibres motion (Bi et al. 2017).

The aforementioned efforts to model the flow behaviour of self-compacting FRCs have their own advantages and drawbacks in investigating the orientation and distribution of rigid steel fibres. However, the mesh-free particle-based Lagrangian approaches seem more practical and appropriate for modelling the flowable concrete and evaluating the dispersion and orientation of fibre suspensions. From the above studies, the mesh-free SPH method have illustrated the capability in modelling the flowable FRCs. From the computational point of view, mesh-free SPH methods are very promising to model the large-deformation of fresh ECC flow, which encompasses bendable synthetic fibres. With a similar intrinsic nature, fresh self-consolidating ECC can also be treated as a non-Newtonian viscous liquid in which its flow characteristics are controlled by its rheology behaviour. Therefore, the later sections of this chapter will describe in detail the numerical scheme to model the non-Newtonian viscous fluid flow using the SPH method.

2.3 Scheme for Numerical Modelling the Flow of Self-Compacting Fibre-Reinforced Cement-Based Materials

Despite the difference of strategy approaches, numerical simulation of the self-compacting FRCs flow possessed an identical process. Generally, the flow chart of the scheme for the numerical simulation of self-compacting cement-based materials containing short fibres is presented in Figure 2.5. From the beginning, physical phenomena regarding the self-compacting FRCs flow are observed and represented by the governing equations of viscous fluid. For solving the governing equations, the whole domain of the considered continuum has to be discretised into separate elements or particles depending on the strategy taken. As discussed above, mesh-free particle-based methods have illustrated the ability and advantage to replace traditional grid-based methods such as finite element or finite volume method due to the large deformation of the fluid flow. Then, the selected approach will define the computational algorithms and steps to approximately resolve the governing equations. The modelling of fibres motion and their interaction with fluid components or with surrounding fibres are also defined at this step. The next stage is to code or translate the computational domain and approximation algorithms using computer programming languages in a specific manner. The obtained results from the computation will be then analysed and visualised by an appropriate technique.
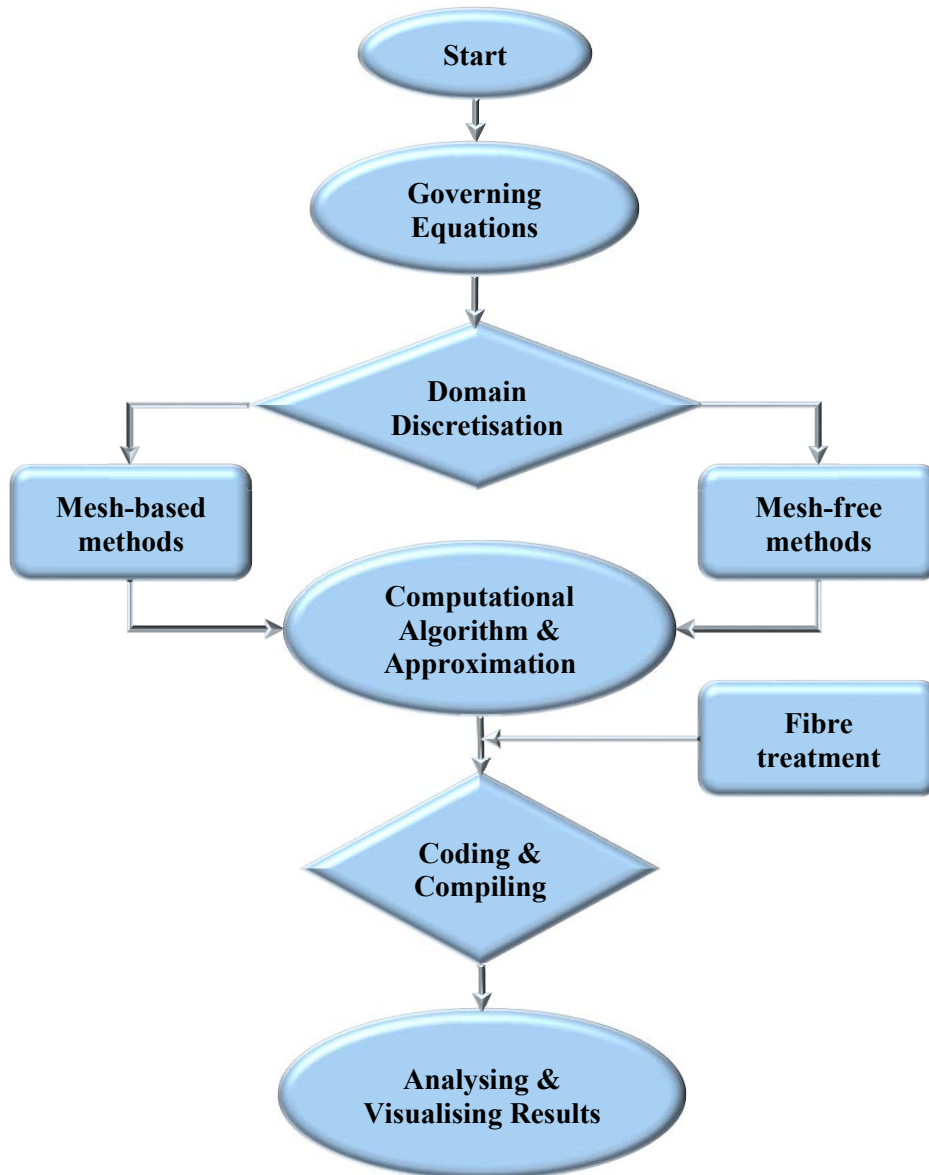
Figure 2.5 Flow chart of numerical strategy for modelling the flow of self-consolidating fibre-reinforced cement-based materials.

2.4 The Governing Equations of Viscous Fluid

As mentioned above, due to the flowability and fluidity of self-consolidating ECC, the fundamental equations of fluid dynamics can be used to govern its flow behaviour. These governing equations are mathematical expressions of three fundamental laws of physics, i.e., mass and energy conservation, and Newton's second law (Anderson 1992).

Although the surrounding temperature has influenced the flow of flowable concrete (Ghafoori & Diawara 2010), it is reasonable to consider that the surrounding temperature being constant and heat flux is absent in the domain of the flowable concrete model. For this reason, the energy conservation can be ignored, and therefore only the continuity (mass) and momentum (Newton's second law) equations govern the flow characteristics of self-consolidating ECC.

2.4.1 The continuity equation

A minuscule element of fluid with fixed mass δm moving along with the flow of viscous fluid is considered. By denoting the volume of this infinitesimal element as δV and its density is ρ, we have:

$$\delta m = \rho \delta V \tag{2.1}$$

During the movement of the fluid element along with the flow, the time rate of change of its mass equals zero due to the mass being conserved, as

$$\frac{D(\delta m)}{Dt} = 0 \tag{2.2}$$

Combining Equation 2.1 and Equation 2.2, we obtain:

$$\frac{D(\rho \delta V)}{Dt} = \delta V \frac{D\rho}{Dt} + \rho \frac{D(\delta V)}{Dt} = 0 \tag{2.3}$$

or,

$$\frac{D\rho}{Dt} + \rho \left[\frac{1}{\delta V} \frac{D(\delta V)}{Dt} \right] = 0 \tag{2.4}$$

The brackets term of the second term in Equation 2.4 represents the time rate of change of the moving fluid element per unit volume, which interpretes the physical meaning of the divergence of velocity $\nabla . v$ as

$$\nabla . v = \frac{1}{\delta V} \frac{D(\delta V)}{Dt} \tag{2.5}$$

Hence, combining Equation 2.4 and Equation 2.5, we have:

$$\frac{D\rho}{Dt} + \rho \nabla . v = 0 \tag{2.6}$$

Equation 2.6 is the non-conservation form of the continuity equation of a fluid element.

2.4.2 The momentum equation

The equation of momentum describes fluid motion of by applying Newton's second law to the moving fluid element. The net force on the fluid element equals its mass times the acceleration of the element. This is a vector-relation and hence can be split into two scalars along the x and y-axes in two-dimensional space or into three scalar relations along the x, y, and z-axes in three-dimensional space (Figure 2.6). Considering the x-component of Newton's 2nd law, we have:

$$F_x = ma_x \tag{2.7}$$

The force F_x exerts on the moving fluid element including two components, these being body forces and surface forces:

- **Body forces:** these forces exert directly on the volumetric mass of the fluid element. The body forces might be gravitational, magnetic or electrical forces in nature.

- **Surface forces:** these forces exert directly on the surface of fluid element. There are two sources in the surface forces, including: (a) the pressure exerting on the element surface, forced by surrounding fluid elements; and (b) the shear and normal stress distributions exerting on the element surface, also enforced by outside fluids by means of friction.
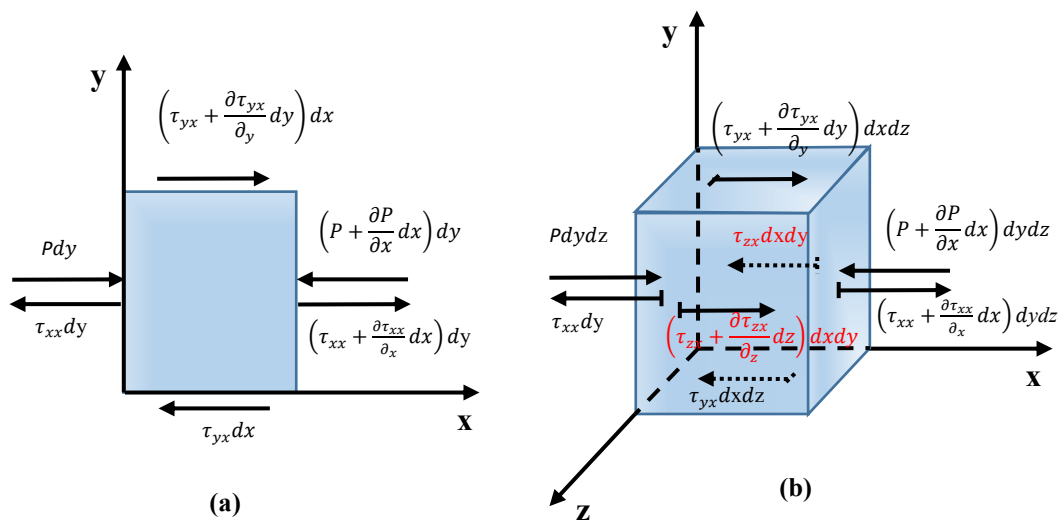
Figure 2.6   Surface forces in x-direction of a moving infinitesimal element of fluid: a) two-dimensional space and b) three-dimensional space.

The body force per unit mass acting on the fluid element is denoted by F_B, with F_{Bx} as its x-component. In the two-dimensional space, the body force exerting on fluid element in x-direction is written as follows:

$$F_{Bx}\rho d_x d_y \tag{2.8}$$

42

By symbolising the surface forces exerting on the fluid element as F_S with F_{Sx} for its x-component, we have:

$$F_{Sx} = Pdy - \left(P + \frac{\partial P}{\partial x}dx\right)dy - \tau_{xx}dy + \left(\tau_{xx} + \frac{\partial \tau_{xx}}{\partial x}dx\right)dy \tag{2.9}$$

$$- \tau_{yx}dx + \left(\tau_{yx} + \frac{\partial \tau_{yx}}{\partial y}dy\right)dx$$

$$F_{Sx} = -\frac{\partial P}{\partial x}dxdy + \frac{\partial \tau_{xx}}{\partial x}dxdy + \frac{\partial \tau_{yx}}{\partial y}dxdy \tag{2.10}$$

Then, the x-component of the total force exerting on fluid element is calculated:

$$F_x = -\frac{\partial P}{\partial x}dxdy + \frac{\partial \tau_{xx}}{\partial x}dxdy + \frac{\partial \tau_{yx}}{\partial y}dxdy + F_{Bx}\rho d_x d_y \tag{2.11}$$

The term a_x in Newton's 2nd law is the time rate of change of velocity v_x. For a fuild element travelling along the flow, this term is given by the substantial derivative, so that

$$a_x = \frac{Dv_x}{Dt} \tag{2.12}$$

Also, the mass of the fluid element is fixed and is equal to

$$m = \rho dxdy \tag{2.13}$$

Substituting Equations 2.12 and 2.13 into Equation 2.7, we have:

$$F_x = \frac{Dv_x}{Dt}\rho dxdy \tag{2.14}$$

Substituting Equation 2.14 into Equation 2.11 leads to the following:

$$\frac{Dv_x}{Dt}\rho dxdy = -\frac{\partial P}{\partial x}dxdy + \frac{\partial \tau_{xx}}{\partial_x}dxdy + \frac{\partial \tau_{yx}}{\partial_y}dxdy + F_{Bx}\rho d_x d_y \qquad (2.15)$$

or

$$\rho\frac{Dv_x}{Dt} = -\frac{\partial P}{\partial x} + \frac{\partial \tau_{xx}}{\partial x} + \frac{\partial \tau_{yx}}{\partial y} + F_{Bx}\rho \qquad (2.16)$$

Similarly with y direction:

$$\rho\frac{Dv_y}{Dt} = -\frac{\partial P}{\partial y} + \frac{\partial \tau_{xy}}{\partial x} + \frac{\partial \tau_{yy}}{\partial y} + F_{By}\rho \qquad (2.17)$$

Equations. 2.16 and 2.17 are x-component and y-component, respectively, of the momentum equation which refers to the moving fluid element in two-dimensional space. Similarly, the x,y,z-components of the momentum equation in three-dimensional space are as follows:

$$\rho\frac{Dv_x}{Dt} = -\frac{\partial P}{\partial x} + \frac{\partial \tau_{xx}}{\partial x} + \frac{\partial \tau_{yx}}{\partial y} + \frac{\partial \tau_{zx}}{\partial z} + F_{Bx}\rho \ , \qquad (2.18a)$$

$$\rho\frac{Dv_y}{Dt} = -\frac{\partial P}{\partial y} + \frac{\partial \tau_{xy}}{\partial x} + \frac{\partial \tau_{yy}}{\partial y} + \frac{\partial \tau_{zy}}{\partial z} + F_{By}\rho \ , \qquad (2.18b)$$

$$\rho\frac{Dv_z}{Dt} = -\frac{\partial P}{\partial z} + \frac{\partial \tau_{xz}}{\partial x} + \frac{\partial \tau_{yz}}{\partial y} + \frac{\partial \tau_{zz}}{\partial z} + F_{Bz}\rho \ . \qquad (2.18c)$$

Since this fluid element is moving with the flow, the above momentum equations are in non-conservation and scalar forms. Those equations have been called the Navier–Stokes equations in honour of two scientists, C. Navier and G. Stokes, who independently obtained the equations in the first half of the nineteenth century.

2.5 Rheology Models to Describe the Behaviour of a non-Newtonian Viscous Fluid

The flow behaviour of a viscous fluid can be either classified as a Newtonian fluid or non-Newtonian fluid. In reality, most fluids are non-Newtonian fluids, which means that the relationship between shear stress τ and shear rate $\dot{\gamma}$ is nonlinear or the viscosity μ varies with time and rate of deformation (shear thinning or thickening). Moreover, non-Newtonian fluids have the yield stress τ_y, which controls the initial stage of flow. When the yield stress τ_y is exceeded, the fluid starts to flow, and then its viscosity controls the fluid flow performance. Several empirical models have been proposed to described non-Newtonian fluid flow, such as Bingham plastic model (Papanastasiou 1987; Ghanbari & Karihaloo 2009), Herschel-Bulkley model (De Larrard et al. 1998; Huang & Garcia 1998), and Cross model (Cross 1965).

2.5.1 Bingham model

The Bingham constitutive model is normally used to describe the behaviour of viscous fluid owning a yield stress τ_y. Once the fluid flows, the shear stress τ increases linearly with an increase in the shear strain rate $\dot{\gamma}$ (identical with Newtonian fluid). When the shear stress falls below the yield stress τ_y, the fluid stops flowing. It is written as

$$\tau = \tau_y + \mu\dot{\gamma} \quad \text{for } \tau > \tau_y \tag{2.19}$$

$$\dot{\gamma} = 0 \quad \text{for } \tau \leq \tau_y \tag{2.20}$$

and the effective viscosity of Bingham model is expressed as

$$\mu_{eff} = \mu + \frac{\tau_y}{\dot{\gamma}} \tag{2.21}$$

Papanastasiou (1987) proposed an exponential regularisation function, which was valid for both yielded and un-yielded liquid. The proposed model was called the Bingham-Papanastasiou model and written as follows:

$$\tau = \mu\dot{\gamma} + \tau_y(1 - e^{-m\dot{\gamma}}) \tag{2.22}$$

The parameter m was proposed to control the exponential growth of the yield stress. When $m = 0$, the Newtonian fluid is recovered as can be seen in Figure 2.7, and when $m = 5.10^4$, the continuous function in Equation 2.22 is fully equivalent to the ideal bi-linear Bingham plastic model (Ghanbari & Karihaloo 2009).
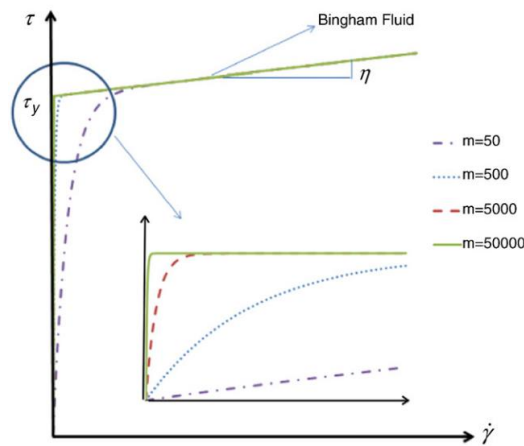
Figure 2.7   The Bingham-Papanastasiou model with different m values. An approach to bi-linear Bingham fluid when $m = 5.10^4$ (Ghanbari & Karihaloo 2009).

2.5.2 Herschel-Bulkley model

The Herschel-Bulkley model is a generalisation of the Bingham model and it can classify a viscous fluid as shear thinning or shear thickening behaviour. This model is expressed as:

$$\tau = \tau_y + \mu \dot{\gamma}^n \quad \text{for } \tau > \tau_y \qquad (2.23)$$

$$\dot{\gamma} = 0 \qquad \text{for } \tau \leq \tau_y \qquad (2.24)$$

In Equation 2.23, the exponential parameter n is an empirical curve-fitting index, and its value varies between 0 and 1 for a shear thinning fluid. When $n = 1$, viscous fluid is said to exhibit Bingham behaviour. Generally, the smaller the value of n indicates the greater shear thinning behaviour of a fluid. Also, the index n is larger than 1 for a shear thickening fluid.

2.5.3 Cross model

The Cross model (Cross 1965) is an alternative model that describes the non-Newtonian flow effectively, and it is written as

$$\mu_{eff} = \mu_\infty + \frac{\mu_0 - \mu_\infty}{1 + (K\dot{\gamma})^m} \qquad (2.25)$$

By taking the power-law index m equals unity, the simplified Cross model is represented as

$$\mu_{eff} = \frac{\mu_0 + K\dot{\gamma}\mu_\infty}{1 + K\dot{\gamma}} \qquad (2.26)$$

where μ_{eff}, μ_0 and μ_∞ are the effective viscosity, viscosity at very low and very high shear strain rate, respectively. K and m are the constant parameters, respectively. The drawback of this model is that it requires four input rheological parameters to determine the effective viscosity of fluid.

2.6 SPH Method-Numerical Approximation

SPH is a "truly" mesh-free particle method, which was simultaneously invented in 1977 for solving astrophysical problems in three-dimensional open space by (Lucy 1977) and (Gingold & Monaghan 1977). The name "Smoothed particle hydrodynamics" emphasised the employment of the smoothing kernel (Parzen 1962) to approximately estimate the value of integrals with a set of particles based on Monte Carlo procedure to solve hydrodynamics problems (Gingold & Monaghan 1977). The SPH had first been developed for simulating compressible flow problems in the confined situations, till the attempt made by Monaghan to spread out the SPH application in an effort to simulate the free surface flows (Monaghan 1994). Since then, researchers worldwide have continued to contribute to the SPH method to unravel numerous sophisticated engineering problems. For instance, near-shore solitary wave (Y.M. Lo & Shao 2002), water waves (Dalrymple & Rogers 2006), free surface Newtonian and non-Newtonian flows (Shao & Lo 2003), weakly compressible (Becker & Teschner 2007), tsunami waves (Rogers & Dalrymple 2008), and other various applications using SPH can be found in (Randles & Libersky 1996; Gomez-Gesteira et al. 2010; Liu & Liu 2010; Violeau & Rogers 2016).

In the SPH method, each particle can carry information about material properties such as mass, density, velocity, etc., depending on problems that need to be solved, and it can characterise deformation of a continuum by particles' motions. Hence, the SPH method has shown strong capacity to model the large deformation, separation, contact and coalescence of composite materials under some specific conditions (Randles & Libersky 1996; Yashiro 2017). Moreover, the Lagrangian nature of SPH makes it possible to track a material element (a particle) during its motion and monitor any

changes in its properties. In other words, the grids are allowed to embed in the particles in the Lagrangian approach, and consequently, free-surface flows and material interfaces are simply tracked, in contrast with the purely Eulerian technique (Liu & Liu 2003). Therefore, although a number of particle-based methods have been developed in the literature to simulate the fluid flow such as Discrete Element Method (Noor & Uomoto 1999), Particle Finite Element Method (Idelsohn et al. 2004), and Moving Particle Semi-implicit (Yashiro et al. 2012), SPH has been receiving much attention for solving sophisticated engineering problems.

2.6.1 Integral and summation interpolants

The SPH method starts from approximating an arbitrary function A($\mathbf{r}$) through its interval over the domain Ω based on a kernel function *W as*

$$A(\boldsymbol{r}) \cong \int_{\Omega} A(\boldsymbol{r}')W(\boldsymbol{r} - \boldsymbol{r}', h)d\boldsymbol{r}' \tag{2.27}$$

where $W(\boldsymbol{r} - \boldsymbol{r}', h)$ is the smoothing kernel or the weighting function (Figure 2.8). The approximated summation for the spatial derivative of the function $A(\boldsymbol{r})$ for a particle *a,* in the influencing range of surrounded particles *b,* is calculated as

$$\nabla A(\mathbf{r})_a = \sum_b m_b \frac{A_b}{\rho_b} \nabla W(\mathbf{r}_a - \mathbf{r}_b, h) \tag{2.28}$$
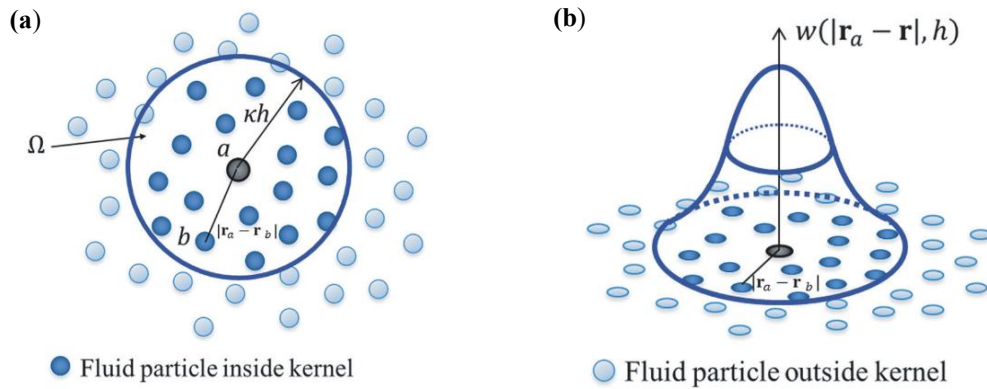
Figure 2.8   Particles distribution: (a) inside and (b) outside of the support domain Ω of particle a (Violeau & Rogers 2016).

2.6.2 The smoothing kernels in SPH

2.6.2.1 SPH kernel and genetic properties

The smoothing performance of SPH simulation critically depends on the choice of kernel function W, with h is its smoothing length, defining the influence area of the kernel function κh, and a non-dimensional distance between particles, given by $q = r/h$, whereas r is the distance between particle a and b, $r = |r_a - r_b|$. According to Morris (2000), a kernel function W can be written in a general form as

$$W(\boldsymbol{r}_{ab}, h) = \frac{1}{h^d} f\left(\frac{\boldsymbol{r}_{ab}}{h}\right)$$

(2.29)

where d represents for the dimensional space of system, and the smoothing length, h, is typically taken to be 1-1.5 times with the particle distance. Moreover, the smoothing kernel W has to satisfy a number of requirements, as follow (Liu et al. 2003):

- The smoothing kernel has to be normalised over its support domain, i.e., the unity condition:

$$\int_{\Omega} W(\boldsymbol{r} - \boldsymbol{r}', h) d\boldsymbol{r}' = 1 \qquad\qquad (2.30)$$

- The smoothing kernel should be compactly supported:

$$W(\boldsymbol{r} - \boldsymbol{r}') = 0 \text{ if } |r - r'| > \kappa h \qquad\qquad (2.31)$$

- The smoothing kernel should be non-negative in the support domain:

$$W(\boldsymbol{r} - \boldsymbol{r}') \geq 0 \qquad\qquad (2.32)$$

- The smoothing kernel should satisfy the Dirac delta function condition as the smoothing length approaches zero:

$$\lim_{h \to 0} W(\boldsymbol{r} - \boldsymbol{r}', h) = \delta(\boldsymbol{r} - \boldsymbol{r}') \qquad\qquad (2.33)$$

- The smoothing kernel should be an even function, i.e having the symetric property, to ensure an identical effect on a given particle from different surrounding particles but having the same distance.

2.6.2.2 Kernel Functions

Many kinds of smoothing functions have been developed in the literature based on these above required properties. In general, the kernel functions have been categorised into four groups based on kernel-shapes, i.e., bell-shape, parabolic-shape, hyperbolic-shape or double hump-shape. The bell-shape kernels have proved their ability to outperform other kernels in the region of smooth data (Fulk & Quinn 1996).

- **Gaussian kernel:** Gingold & Monaghan (1977) has utilised this kernel function to simulate non-spherical stars (Equation 2.34). The Gaussian kernel performs a

stable and accurate interpolation. However, this kernel requires excessive computational time because a lengthy distance to approach zero is necessary (Figure 2.9b).

$$W(\mathbf{r},h) = \alpha_d e^{-q^2} \tag{2.34}$$

where $\alpha_d = \begin{cases} 1/\sqrt{\pi}h & \text{in 1D} \\ 1/\pi h^2 & \text{in 2D} \\ 1/\sqrt{\pi^3}h^3 & \text{in 3D} \end{cases}$

- **Cubic spline kernel** (Monaghan 1992) has been the most commonly used of the SPH approaches since it closely resembles a Gaussian function while exhibiting a narrower compact support (Equation 2.35 and Figure 2.9b). However, its second derivative is a piecewise linear function (Figure 2.9a) and consequently, the stability properties of cubic spline kernel might be inferior to those of smoother kernels such as double cosine kernel function proposed by Yang et al. (2014) (Figure 2.10).

$$W(\mathbf{r},h) = \alpha_d \begin{cases} 1-\frac{3}{2}q^2+\frac{3}{4}q^3 & \text{for } 0\leq q\leq 1 \\ \frac{1}{4}(2-q)^3 & \text{for } 1<q\leq 2 \\ 0 & \text{for } q>2 \end{cases} \tag{2.35}$$

where $\alpha_d = \begin{cases} 1/h & \text{in 1D} \\ 10/7\pi h^2 & \text{in 2D} \\ 1/\pi h^3 & \text{in 3D} \end{cases}$

(a)   **(b)**
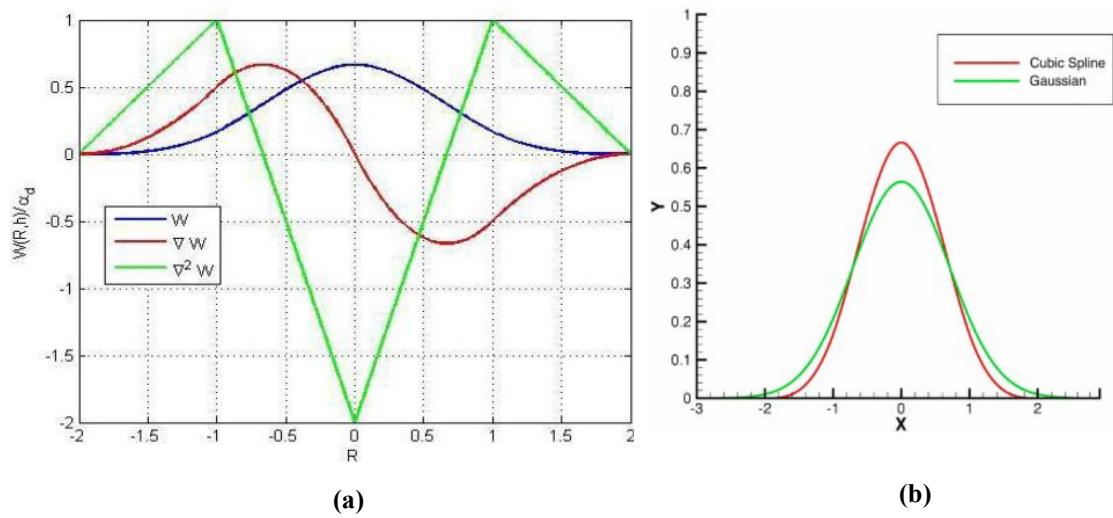
Figure 2.9   (a) Cubic spline and its derivative ($\kappa = 2$)(Deeb 2013); (b) Comparison of the Cubic spline and Gaussian kernel functions (Li & Liu 2002).
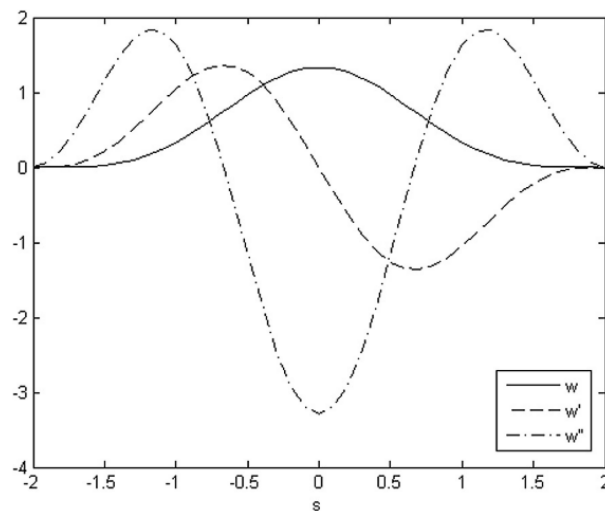
Figure 2.10   Double cosine function and its derivatives ($\kappa = 2$) (Yang et al. 2014).

Other smoothing functions have been developed such as quadratic kernel function (Johnson et al. 1996; Liu et al. 2003), high order spline (quartic and quantic) kernel (Wendland 1995; Morris 1996), and double cosine kernel function (Yang et al. 2014).

2.6.3 Improvement of SPH approximation

In the simulation of fluid dynamics, especially free surface flow, the standard SPH algorithms do not precisely approximate or reproduce the properties of particles near the boundary or at free-surface. The smoothing kernel is truncated due to the absence of nearby particles in these zones, which results in the conditions of consistency and normalisation of kernel might no longer satisfy. Therefore, some correction techniques have been developed in the literature with the aim of enhancing the accuracy of the interpolation algorithms of SPH. Moreover, the correction methods help to satisfy the conservation of angular momentum, which is not automatically satisfied in SPH. In this section, two techniques for kernel renormalisation, i.e., by correcting kernel function or its gradient to prevent inaccuracies from a corrupted interpolating function, are briefly introduced.

2.6.3.1 Kernel correction

The method was first proposed by (Liu et al. 1997) and later by (Bonet & Lok 1999). Modifying the kernel was proposed to guarantee the values of polynomial functions up to a given degree was precisely interpolated. For the first-order (linear) correction, they introduced two functions $\alpha(r)$ and $\beta(r)$ so that the correction kernel $\widetilde{W}_{ab}$ is expressed as

$$\widetilde{W}_{ab} = W_{ab}\alpha(r)[1 + \beta(r).(\mathbf{r}_a - \mathbf{r}_b)] \tag{2.36}$$

The functions $\alpha(r)$ and $\beta(r)$ could be identified by enforcing the correction kernel $\widetilde{W}_{ab}$ must exactly interpolate any linear velocity distribution, that is:

$$\boldsymbol{v}_0 + \boldsymbol{v}_1 \cdot \boldsymbol{r} = \sum_b \frac{m_b}{\rho_b}(\boldsymbol{v}_0 + \boldsymbol{v}_1 \cdot \boldsymbol{r}_b)\widetilde{W}_{ab} \tag{2.37}$$

Since both $\boldsymbol{v}_0$ and $\boldsymbol{v}_1$ are arbitrary vectors, the following consistency conditions must therefore be satisfied by the corrected kernel:

$$\sum_b \frac{m_b}{\rho_b}\widetilde{W}_{ab} = 1 \tag{2.38a}$$

$$\sum_b \frac{m_b}{\rho_b}((\boldsymbol{r}_a - \boldsymbol{r}_b))\widetilde{W}_{ab} = 0 \tag{2.38b}$$

From Equation 2.36 and Equations 2.38a and 2.38b, the two correction funtions $\alpha(\boldsymbol{r})$ and $\beta(\boldsymbol{r})$ are obtained. However, since both $\alpha(\boldsymbol{r})$ and $\beta(\boldsymbol{r})$ are functions of $\boldsymbol{r},$ this liner correction technique has shown computational expensive, so unsuitable for explicit type of calculations (Bonet & Lok 1999). Thus, Bonet & Lok (1999) have suggested using constant correction by taking $\beta(\boldsymbol{r}) = 0$, which simplified the corrected kernel as

$$\widetilde{W}_{ab} = \frac{W_{ab}}{\sum_b \frac{m_b}{\rho_b}W_{ab}} \tag{2.39}$$

So, a vectorial variable $A(\boldsymbol{r})_a$ can be expressed as

$$A(\boldsymbol{r})_a = \frac{\sum_b \frac{m_b}{\rho_b}A(\boldsymbol{r})_b W_{ab}}{\sum_b \frac{m_b}{\rho_b}W_{ab}} \tag{2.40}$$

2.6.3.2 Kernel gradient correction

In this technique, Bonet & Lok (1999) introduced a correction matrix **L**, to give:

$$\widetilde{\nabla}W_{ab} = \boldsymbol{L}_a\nabla W_{ab} \tag{2.41}$$

The correction matrix **L** is calculated at each particle by enforcing the below condition to satisfy:

$$\sum_b \frac{m_b}{\rho_b}(\boldsymbol{r}_b - \boldsymbol{r}_a) \otimes \tilde{\nabla} W_{ab} = \left(\sum_b \frac{m_b}{\rho_b}(\boldsymbol{r}_b - \boldsymbol{r}_a) \otimes \nabla W_{ab}\right) \boldsymbol{L}_a^T = \boldsymbol{I} \tag{2.42}$$

from which **L** is evaluated explicitly in the following form:

$$\boldsymbol{L}_a = \left(\sum_b \frac{m_b}{\rho_b} \nabla W_{ab} \otimes (\boldsymbol{r}_a - \boldsymbol{r}_b)\right)^{-1} \tag{2.43}$$

2.6.4 Equation of states and numerical schemes in SPH

There are two main approaches to solve the pressure term and mass conservation in modelling free surface flows by SPH, i.e., the truly incompressible SPH (ISPH) and weakly compressible SPH (WCSPH). While ISPH fulfils the incompressibility condition of fluid, WCSPH considers the fluid to be lightly compressible (Lee et al. 2008; Hughes & Graham 2010).

2.6.4.1 Weakly compressible SPH (WCSPH)

WCSPH is the most commonly used technique to compute the pressure term and mass conservation in the governing equations of viscous fluid. The modification of Tait's equation, which has been proposed by Monaghan (Monaghan 1994) to suit the bulk flow of fluid in WCSPH approach, has the following form:

$$P_n = B\left(\left(\frac{\rho_n}{\rho_0}\right)^{\gamma} - 1\right) \tag{2.44}$$

where γ is a power coefficient, which its value is depended on fluid properties, and ρ_0 is the reference density of the fluid. Whereas, *B* is the constant pressure which governs the relative density fluctuation $\frac{|\Delta\rho|}{\rho_0}$. This fluctuation scales with the Mach number of flow as follows (Cummins & Rudman 1999; Becker & Teschner 2007):

$$\frac{|\Delta\rho|}{\rho_0} \sim \frac{|v_f|^2}{c_s^2} \tag{2.45}$$

where c_s and v_f denote the speed of sound in the fluid and the speed of fluid flow, respectively. By assuming that c_s to be large enough to preserve the fluctuation of density below an order of 1%., then B is taken as

$$B = \frac{\rho_0 c_s^2}{\gamma} \tag{2.46}$$

by substituting B into Equation 2.44, we have:

$$P_n = \frac{\rho_0 c_s^2}{\gamma}\left(\left(\frac{\rho_n}{\rho_0}\right)^\gamma - 1\right) \tag{2.47}$$

The WCSPH is an explicit time-stepping method, in which the densities, velocities and positions are calculated and updated at each time step. For this reason, the WCSPH requires a very small time step to ensure the stability interpolation of fluid properties. A flow chart using the predictor-corrector algorithm (Monaghan 1989) for WCSPH is illustrated in Figure 2.11. The values of density ρ, velocity $\boldsymbol{v}$ and position $\boldsymbol{r}$ of particles at time step *n* are utilised to predict and correct at the two half-time steps *n + ½,* and then final values are summarised on the time step *n + 1*.

Step1: Prediction step:

$$\rho_{n+1/2} = \rho_n + \frac{\Delta t}{2} \nabla . v_n;$$

$$v_{n+1/2} = v_n + \left(-\frac{1}{\rho}\nabla P_n + g + \frac{1}{\rho}\nabla \tau_n\right)\frac{\Delta t}{2};$$

$$r_{n+1/2} = r_n + \frac{\Delta t}{2} v_{n+1/2};$$

Calculate pressure

$$P_{n+1/2} = \frac{\rho_0 c_s^2}{\gamma}\left(\left(\frac{\rho_{n+1/2}}{\rho_0}\right)^\gamma - 1\right)$$

Step2: Correction step:

$$\rho_{n+1/2} = \rho_n + \frac{\Delta t}{2} \nabla . v_{n+1/2};$$

$$v_{n+1/2} = v_n + \left(-\frac{1}{\rho}\nabla P_{n+1/2} + g + \frac{1}{\rho}\nabla \tau_n\right)\frac{\Delta t}{2};$$

$$r_{n+1/2} = r_n + \frac{\Delta t}{2} v_{n+1/2};$$

another half time step $n + \frac{1}{2}$

$n = n + 1; t = t$

Step3: Final step

$$v_{n+1} = 2v_{n+1/2} - v_n$$

$$\rho_{n+1} = 2\rho_{n+1/2} - \rho_n$$

$$r_{n+1} = 2r_{n+1/2} - r_n$$
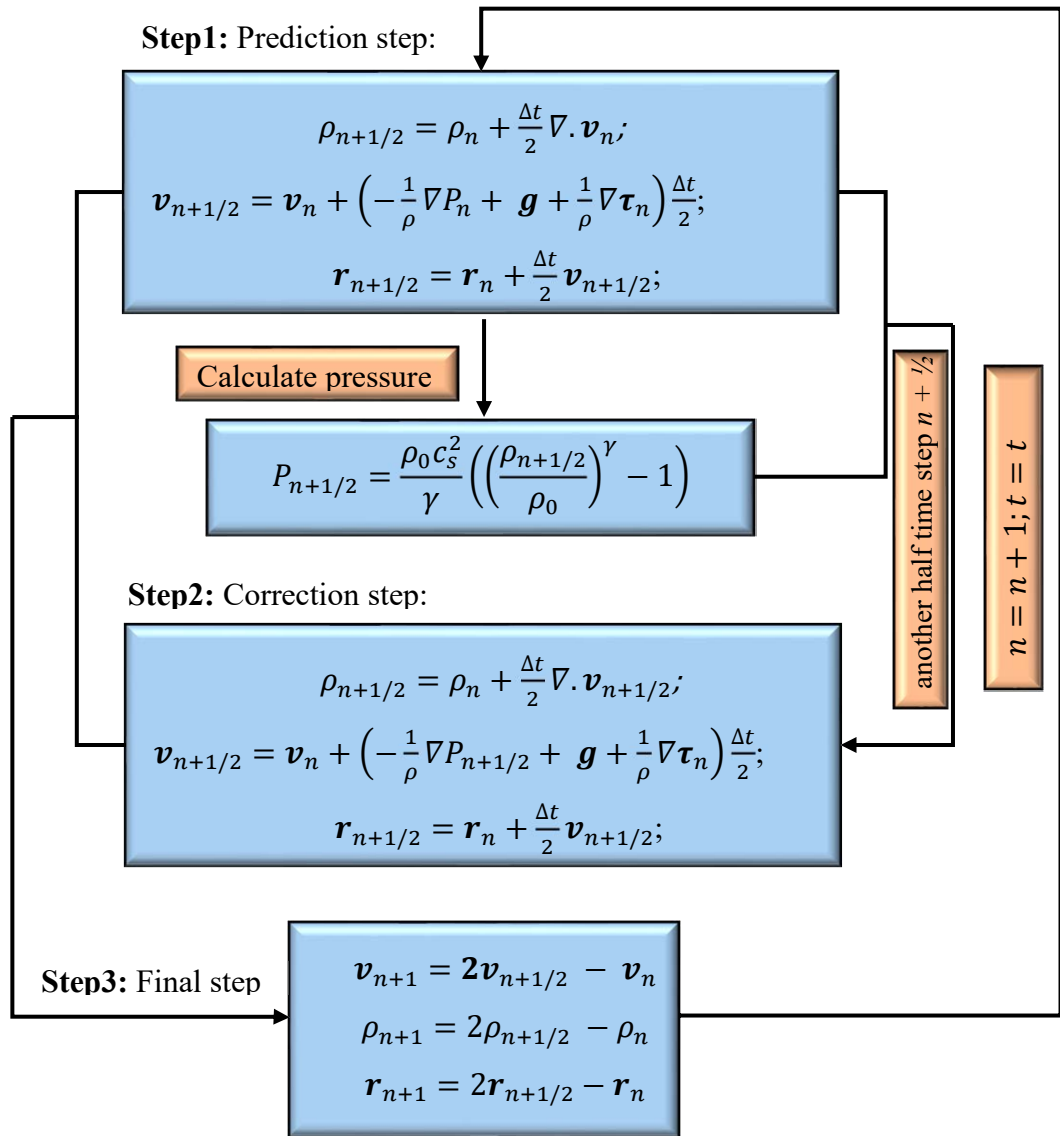
Figure 2.11   Flow chart showing the three steps of predictor-corrector algorithm in WCSPH.

2.6.4.2 Truly incompressible SPH (ISPH)

In contrast with WCSPH, the ISPH is a semi-implicit approach to model the incompressible flow. In ISPH, the density is constant, thus the continuity equation of fluid flow (Equation 2.6) reduces to $\nabla . v = 0$. The classical projection method (Cummins & Rudman 1999) is used to solve the velocity-pressure coupling problem in the Navier-Stokes equations. The discretised form of momentum equation (Equation

2.17) in the governing equations of fluid is separated into two parts: firstly, the viscous and gravity forces serve to predict the intermediate velocity; and secondly, the pressure force functions to correct the particles' velocity. The procedure of this approach is summarised by a flow chart in Figure 2.12. The intermediate velocity v_{n+1}^* is typically not divergence-free, but this is imposed upon the corrected velocity v_{n+1}. Hence, the intermediate velocity is projected on the divergence-free space, including the incompressibility condition ($\nabla v_{n+1} = 0$) and constant density ρ. Once the pressure term is obtained from solving the Poisson equation, the velocity of particles is updated by the computed pressure gradient. Finally, each particle's position is also updated using the obtained corrected velocity (Lee et al. 2008).
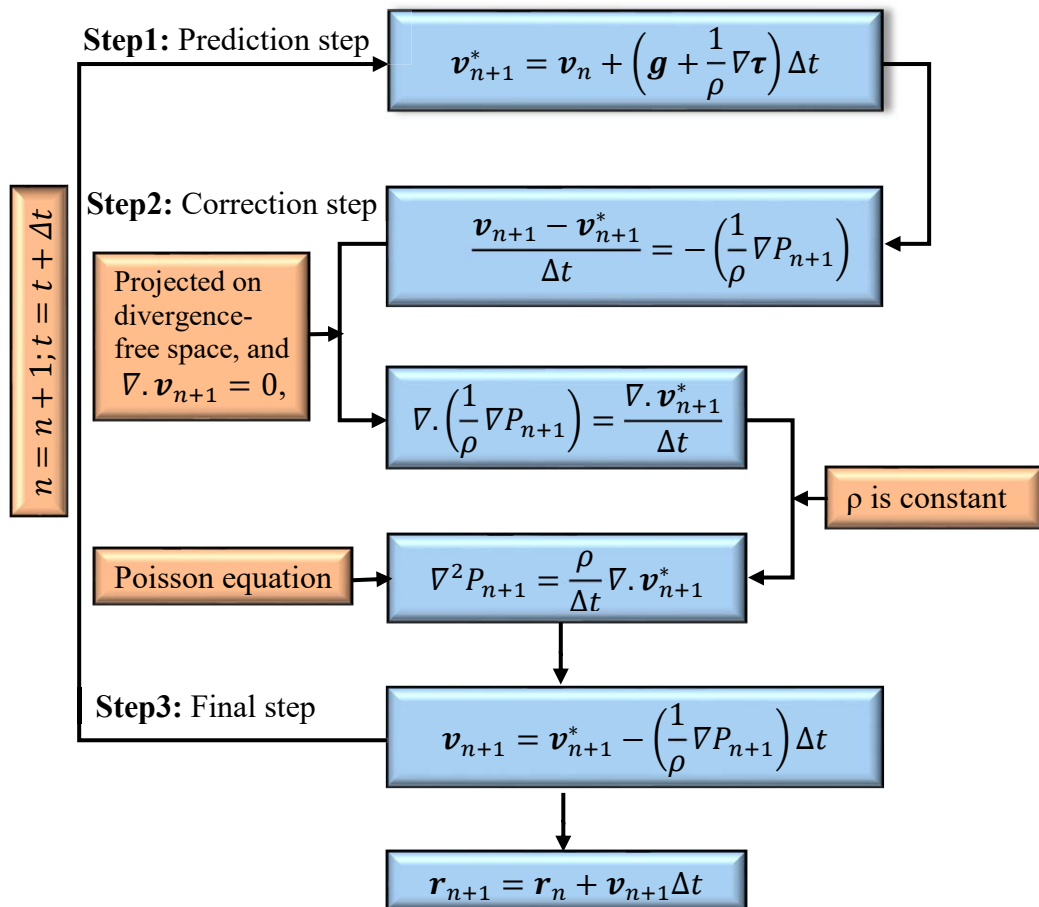
Figure 2.12   Flow chart showing the predictor-corrector steps of projection method in ISPH.

2.6.5 Boundary conditions

Implementing the boundary conditions in the mesh-free SPH is not as straightforward as the mesh-based methods. Typically, the solid boundary is also modelled by separated and frozen particles in SPH. These immovable particles have to properly interact with the mobile particles and keep them inside the computational domain during the processing time. Since the emergence of the meshless, SPH method, a range of available techniques have been developed to model the boundary condition. The typical methods that can be found in the literature are the repulsive forces particle (Monaghan 1994), mirror (or ghost) particles (Cummins & Rudman 1999), dummy particles (Shao & Lo 2003) and boundary integrals (Feldman & Bonet 2007; Leroy et al. 2014). Violeau & Rogers (2016) have classified the above methods into three general groups, as shown in Figure 2.13. The primary roles of these techniques are first to prevent fluid particles from penetrating through the boundary, and second, to solve the problem of the lack of fluid particles in the supported range of the kernel function along the boundaries.
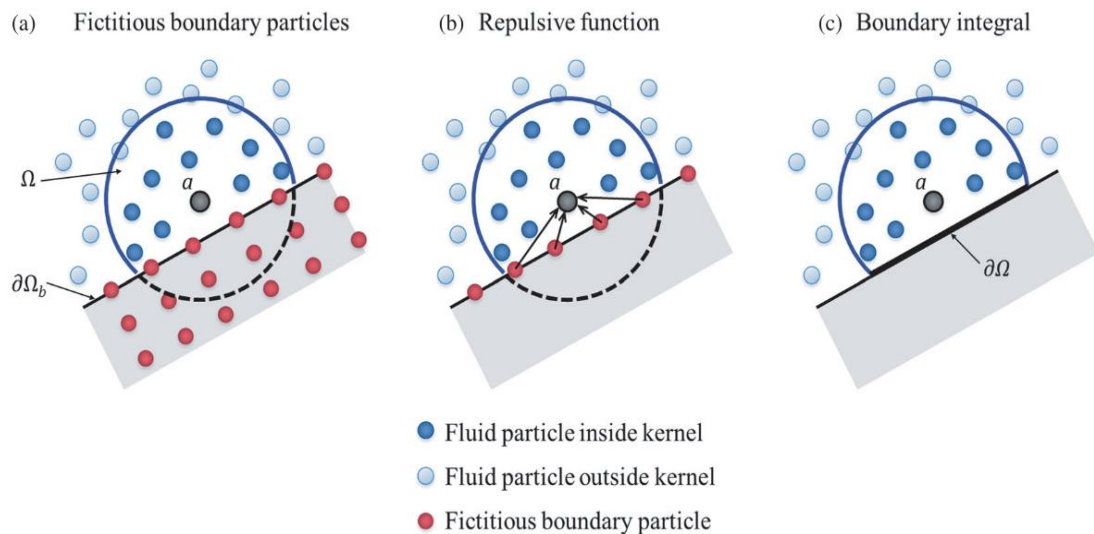
Figure 2.13   Group methods of boundary particle conditions represent the rigid walls in SPH (Violeau & Rogers 2016).

- ***Fictitious boundary particles*** include several techniques such as prescribed (dummy) fluid particles, mirror (ghost) particles, or dynamic particles. The approach of dummy particles is to add several layers of zero-velocity particles but still satisfy the governing equations of fluid particles. Shao & Lo (2003) proved that four rows of dummy particles were sufficient to represent the boundary particles. Meanwhile, Dalrymple & Knio (2001) and Crespo et al. (2007) confirmed that the two-layer particles were satisfactory for the dynamic boundary conditions. The mirror particles method is an alternative technique, first introduced by Cummins & Rudman (1999), by creating the ghost images of fluid particles. When the fluid particles approach the boundary, they will interact with their mirror image particles and thus not penetrate the solid boundary since they cannot pass through themselves. However, the accuracy of this approach was significantly affected by the complicated geometries such as sharp vortex-forming corners, due to the variation of density in those areas (Violeau & Rogers 2016).

- ***Repulsive force boundary*** was proposed by Monaghan (1994) with one layer of fixed particles, exerting the central forces on the approaching fluid particles to ensure they cannot cross through the boundary. The expression form of this approach is similar to intermolecular forces of the Lennard-Jones potential. The problem of a non-constant force exerts on the particle moving parallel to the wall of the original method was then corrected by Monaghan & Kos (1999). After that, Rogers & Dalrymple (2008) proposed an additional function to modify the magnitude of the repulsive force conforming to the local depth of fluid particles and their normal velocity with the boundary. While the implementation of this method is relatively straightforward, the lack of fluid particles in the kernel

support range has to be solved, in order to stabilise the accuracy of the interpolated summation of SPH.

- *Boundary integral*: the basic idea of this method is to solve the problem of the interpolation in SPH associated with the truncated kernel at the boundary. A renormalised factor was added to the integral of the function A(r) in order to compensate for the absence of surrounding fluid particles in the support domain (Kulasegaram et al. 2004; Cercos-Pita 2015). Subsequently, this method can be applied to any arbitrary wall-boundary condition (Ferrand et al. 2013).

- *Free-surface condition* (Figure 2.14): The approach for free-surface condition in SPH is relatively different between WCSPH and ISPH. In WCSPH, the pressure at the free surface tends to drop to zero because of the lack of particles above thanks to the equation of state (Equation 2.44). By contrast, the pressure of free-surface particles must be assigned equal to zero in ISPH approach (in other words, the Dirichlet condition) due to the semi-implicit approach of ISPH in solving the Poisson equation (Figure 2.12). In this way, particles are considered to be surface particles if their density fluctuation is over 1%, but below that of the inner fluid in ISPH (Shao & Lo 2003; Nomeritae et al. 2016).
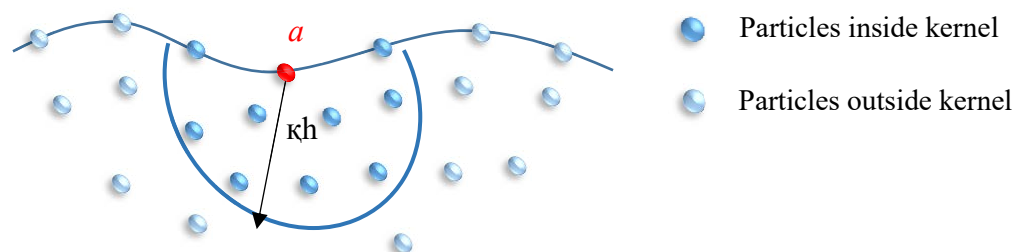
Figure 2.14 Boundary particles at free-surface condition.

2.7 Conclusions

Computer-aided numerical simulation has emerged as a useful tool to investigate the flowability and filling ability of fresh flowable FRCs in the formwork. The simulation models can provide a better understanding of the flow behaviour of fresh concrete containing fibre, helping to improve the casting procedure at in-situ construction, enhancing the matrix-fibre interaction at the hardened state. In this chapter, an effective computational modelling strategy using SPH for modelling the flow behaviour of flowable FRCs has been presented in detail. The adaptability and Lagrangian nature of SPH have shown a promising to model the flow of self-consolidating or flowable ECC, which can also be considered as a non-Newtonian viscous fluid containing flexible fibres.

In the next chapters, appropriate computational approaches using SPH are developed to model the flow behaviour of self-consolidating ECC containing flexible synthetic fibres. In SPH approaches, flexible synthetic fibres are also modelled by separated particles as mortar particles. A suitable rheology model is applied to describe the constitutive behaviour of flowable ECC. The models are coded and compiled based on an open-source SPH program (called SPHYSICS*),* which were collaboratively developed to study free-surface flows by researchers at the University of Vigo (Spain), Johns Hopkins University (U.S.A.) and the University of Manchester (U.K.). The proposed models are programmed in two and three dimensions with a variety of geometrical shapes, which are similar to those devices using for the workability tests of fresh self-consolidating ECC described in Chapter 1.

Chapter 3

Modelling of Self-Consolidating ECC

Flow Using SPH

3.1 Introduction

The implementation of fibres into the cementitious matrix has been proven to be able to reduce or even eliminate the brittleness of ordinary concrete, enhancing ductility, fracture toughness, energy dissipation and durability of FRCs structural elements (Bentur & Mindess 2014). However, intensive studies have indicated the crucial influence of the dispersion and orientation of fibres on the performance of FRCs, which could lead to the variation in the mechanical behaviour in different parts of a structural element. This undesirable feature has restricted the application of FRCs materials in large-scale onsite production and industrial construction. Prior investigations have revealed that the rheology properties of the fresh mix, the fibre's length, the mixing and casting procedures, the size of specimens and the wall-effect are the main factors affecting the fibre distribution and orientation in FRC (Alberti et al. 2018b), and studies on the distribution and orientation of fibres have mainly focused on rigid fibres such as steel fibres in FRCs (Alberti et al. 2018b).

Engineered cementitious composites (ECC), a typical high-performance fibre reinforced cementitious composites (HPFRCC), exhibit a high tensile ductility with tensile strain capacities in excess of 5% by using a moderately low synthetic fibres fraction (typically 2% or less by volume). Designed by the micromechanics approach in fibres/matrix interaction, the mechanical of ECC properties are tailorable, forming a range of ECC for different functionalities such as self-consolidating ECC (SC-ECC) which was developed for large-scale on-site construction applications (Li, Kong, et al. 1998; Kong et al. 2003b; 2003a; Lepech & Li 2008); self-healing ECC (Wu et al. 2012) or ECC using local ingredients (Meng, Huang, et al. 2017). Among these, SC-ECC and its variants, which have been employed in real-scale structural members (Kunieda &

Rokugo 2006; Lepech & Li 2009), are receiving much more attention. However, the distribution and orientation of synthetic fibres and their influence on the tensile properties of SC-ECC are still rarely investigated to date. Moreover, synthetic fibres normally used in SC-ECC such as PE or PVA fibres with the fine diameter of 0.038 mm (Kong et al. 2003b) or 0.048 mm (Kong et al. 2003a), are flexible, which means they can be bent or coiled in the mix during the casting process, and this might significantly affect the distribution and orientation of fibres. For example, in the experimental study of Felekoğlu et al. (2015) with moderate vibration moulding mixtures, it was concluded that the real number of flexible polypropylene (PP) fibres at fracture sections was significantly less than the theoretical value due to the bending and inclining phenomenon of PP fibres.

In practice, it is not straightforward to investigate the distribution and orientation of synthetic fibres due to their lower contrast in comparison with cementitious matrix as well as their non-conductive nature. To investigate the distribution of PVA fibres, Torigoe et al. (2003) tried to use fluorescence technique to capture PVA fibres as green to yellow dots with a charge-coupled device (CCD) camera through a microscope. Felekoğlu et al. (2015) used scanning electron microscope (SEM) of micro-images at backscattered electron mode (BEC) to detect the dispersion PP fibres. These techniques require the employment of an image analysis program, which is extremely time-consuming. Moreover, the influence of casting process on the bending phenomenon of flexible synthetic fibre could not be determined.

Various numerical methods have been developed to model fresh SCC flow and to investigate the distribution and orientation of steel fibre-reinforced SCC (SFR-SCC) (Kulasegaram et al. 2011; Svec et al. 2011; Mechtcherine et al. 2014; Švec et al. 2014).

Mesh-free method, in which the entire computational domain is separated by distinct particles, has been used to approximately solve the governing equations of SCC flow. An overview of the utilisation of discrete element method for modelling the flow of SCC was presented by (Mechtcherine et al. 2014). Svec et al. (2011) implemented the Lattice Boltzmann method to model the flow of SFR-SCC, and then investigated the orientation of steel fibres in SCC considering the influence of a rough formwork surface (Švec et al. 2014). Kulasegaram et al. (2011) used smoothed particle hydrodynamics (SPH) to simulate SCC flow with the conventional cone test and L-box test in two dimensions. Among these methods, SPH, a mesh-free Lagrangian particle method, which was originally invented to solve astrophysical problems, has been emerging as a powerful approach for simulating the flow of SFR-SCC. The SPH was used to simulate the SFR-SCC flow with the slump tests (Deeb, Kulasegaram, et al. 2014b) and L-box tests (Deeb, Kulasegaram, et al. 2014a) in three dimensions.

In this chapter, the flow of SC-ECC is simulated using the SPH methodology to solve the Navier-Stokes constitutive equations in Lagrangian form. The SC-ECC is treated as weakly compressible, which allow the density to fluctuate during the computational time slightly, to compute the pressure term in the governing equation. Flexible synthetic fibres are modelled as separate particles which possess the same continuum properties as mortar particles in the computational domain. A drag force between two adjacent fibre particles within a fibre is added in the momentum equation each time step to prevent them receding each other, and to avoid the length of fibre exceeding the initial fibre's length. The flow of SC-ECC is first simulated with the slump flow tests to validate the proposed method with the experimental data obtained from the literature. Then, the simulation of SC-ECC mixes casting into the mould of the

beam/slab specimens with two different funnel locations is conducted to study the influence of the casting position, the wall-effects and the distance of flow to the distribution and orientation of flexible synthetic fibres during the flow of SC-ECC. The results of numerical modelling provide an insight into the SC-ECC's flow characteristics, and how the flexible synthetic fibres distribute and orient during flow.

This chapter is structured as follows. The SPH Lagrangian form of the Navier-Stokes constitutive equations of SC-ECC fluid and weakly compressible smoothed particle hydrodynamics (WCSPH) are described in Section 3.2. Section 3.3 presents the procedures of numerical simulation including flexible synthetic fibre modelling, input rheology parameters and time integration scheme. The numerical results are presented and discussed in Section 3.4. Finally, Section 3.5 addresses the concluding remarks of this chapter.

3.2 Numerical Schemes

3.2.1 Governing equations

In the case of SC-ECC, due to its flowability and fluidity, the constitutive equations of a viscous fluid can be used to describe the motion of SC-ECC flow. The isothermal Lagrangian form of the Navier-Stokes equations describes the mass conservation in the continuity equation and the motion of particles in the momentum equation. Considering that the body force acting is only the gravitational force **g**, they can be written in the following forms:

$$\frac{D\rho}{Dt} = -\rho \nabla . \boldsymbol{v} \qquad (3.1)$$

$$\frac{D\boldsymbol{v}}{Dt} = -\frac{1}{\rho}\nabla P + \frac{1}{\rho}\nabla\boldsymbol{\tau} + \boldsymbol{g} \tag{3.2}$$

where ρ, t and P denote the density, time and pressure of fluid particles, respectively. The $\boldsymbol{v}$, $\boldsymbol{\tau}$ and $\boldsymbol{g}$ are the particles velocity, shear stress tensor and gravitational acceleration in compact vectorial form, respectively.

3.2.2 Smoothed particle hydrodynamics (SPH)

3.2.2.1 Integral and summation interpolants

The concept of the SPH method starts by approximating an arbitrary function A(r) through its interval over the domain Ω base on a kernel function W as follows:

$$A(\boldsymbol{r}) \cong \int_{\Omega} A(\boldsymbol{r'})W(\boldsymbol{r} - \boldsymbol{r'}, h)d\boldsymbol{r'} \tag{3.3}$$

where $W(\boldsymbol{r} - \boldsymbol{r'}, h)$ is the smoothing kernel or the weighting function, usually chosen to be an even function, which becomes a delta function when h approaches zero, and $d\boldsymbol{r'}$ is a differential volume element. The approximated summation for the spatial derivative of the function $A(\boldsymbol{r})$ for a particle a, in the influencing range of surrounded particles b, is calculated using Equation 3.4.

$$\nabla A(\boldsymbol{r})_a = \sum_b m_b \frac{A_b}{\rho_b}\nabla W(\boldsymbol{r}_a - \boldsymbol{r}_b, h) \tag{3.4}$$

The smoothing performance of an SPH simulation is critically dependent on the kernel function W, with h being its smoothing length, defining the influence area of the kernel function κh, and a non-dimensional distance between particles, given by $q = r/h$, with r as the distance between particle a and b. Many kinds of kernel functions have

been developed in the literature, and the usually used cubic spline (Equation 3.5) is

adopted here due to its stability and accuracy (Shao & Lo 2003),

$$W(r,h) = \frac{10}{7\pi h^2} \begin{cases} 1 - \frac{3}{2}q^2 + \frac{3}{4}q^3 & for\ 0 \leq q \leq 1 \\ \frac{1}{4}(2-q)^3 & for\ 1 < q \leq 2 \\ 0 & for\ q > 2 \end{cases}$$

(3.5)

Due to the absence of neighbouring particles near the boundaries or at the free

surface, the smoothing kernel is truncated as shown in Figure 3.1. This issue may reduce

the accuracy of the SPH method through the corrupted interpolating function, hence the

corrected kernel $\widetilde{W}$ is used in this study. More information on this correction

methodology can be found in (Bonet & Lok 1999; Bonet & Kulasegaram 2000; Gomez-

Gesteira et al. 2012). Then, the gradient of the pressure term in Equation 3.2 can be

written in a symmetric form of a corrected SPH as follows (Shao & Lo 2003):

$$\left(\frac{1}{\rho}\nabla P\right)_a = \sum_b m_b \left(\frac{P_a}{\rho_a^2} + \frac{P_b}{\rho_b^2}\right) \nabla_a \widetilde{W}_{ab}$$

(3.6)

where $\nabla_a \widetilde{W}_{ab}$ is the gradient of the corrected kernel taken with respect to the position of

particle a. Only finite particles b in the smoothing kernel length h contribute to the

summation.
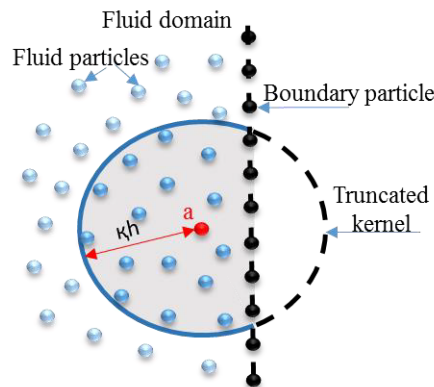
Figure 3.1   Truncated smoothing kernel at boundary.

The discretisation SPH form of the continuity and momentum equations of fluid flow in Equations. 3.1 and 3.2 can be expressed in the following corrected SPH forms:

$$\frac{d\rho_a}{dt} = \sum_b m_b (\boldsymbol{v}_a - \boldsymbol{v}_b) \nabla_a \widetilde{W}_{ab} \tag{3.7}$$

$$\frac{d\boldsymbol{v}_a}{dt} = -\sum_b m_b \left(\frac{P_a}{\rho_a^2} + \frac{P_b}{\rho_b^2} \right) \nabla_a \widetilde{W}_{ab} + \boldsymbol{g} + \textit{viscosity term} \tag{3.8}$$

3.2.2.2 Artificial viscosity

To stabilise the numerical algorithm or allow shock phenomena to be simulated, the artificial viscosity term, denoted by Π_{ab} (Monaghan 1992) is also used in this study. A typical form of Π_{ab} is shown in Equation 3.9.

$$\Pi_{ab} = \begin{cases} -\frac{\alpha \overline{c_{ab}}}{\overline{\rho_{ab}}} \cdot \frac{h \boldsymbol{v}_{ab} \boldsymbol{r}_{ab}}{r_{ab}^2 + 0.01 h^2}, & \boldsymbol{v}_{ab} \boldsymbol{r}_{ab} \leq 0 \\ 0 & \boldsymbol{v}_{ab} \boldsymbol{r}_{ab} > 0 \end{cases} \tag{3.9}$$

where $\boldsymbol{r}_{ab} = \boldsymbol{r}_a - \boldsymbol{r}_b$ and $\boldsymbol{v}_{ab} = \boldsymbol{v}_a - \boldsymbol{v}_b$ are the position and the velocity corresponding to the particles a and b; $\overline{c_{ab}} = (c_a + c_b)/2$ is the average speed of sound of particles a and b, and α is a free parameter that can be changed according to each problem. Becker (Becker & Teschner 2007) proposed that α is between 0.08 and 0.5 depending on the problem, and α is chosen to be 0.5 in the current study. The artificial viscosity Π_{ab} is normally added to the pressure term as

$$\frac{d\boldsymbol{v}_a}{dt} = -\sum_b m_b \left(\frac{P_a}{\rho_a^2} + \frac{P_b}{\rho_b^2} + \Pi_{ab} \right) \nabla_a \widetilde{W}_{ab} + \boldsymbol{g} + \textit{viscosity term} \tag{3.10}$$

3.2.2.3 Viscosity term

The divergence form in the corrected SPH definition of the viscosity term in Equation 3.8 is expressed in a symmetric form as follows (Shao & Lo 2003):

$$\left(\frac{1}{\rho}\nabla\boldsymbol{\tau}\right)_a = \sum_b m_b \left(\frac{\boldsymbol{\tau}_a}{\rho_a^2} + \frac{\boldsymbol{\tau}_b}{\rho_b^2}\right)\nabla_a\widetilde{W}_{ab} \tag{3.11}$$

where the shear stress tensor $\boldsymbol{\tau}$ is related to the strain tensor $\boldsymbol{E}$ in the following form:

$$\tau_{ji} = \mu_{eff}E_{ij} \tag{3.12}$$

where μ_{eff} is the effective viscosity, which is variable in a non-Newtonian flow and can be modelled by the Bingham model, as generally used in (Kulasegaram & Karihaloo 2013; Dhaheer et al. 2016; AL-Rubaye et al. 2017), and can be expressed by Equation 3.13,

$$\mu_{eff} = \mu_B + \frac{\tau_B}{\dot{\gamma}} \tag{3.13}$$

or by Cross model (Shao & Lo 2003; Wu et al. 2016) in the following form:

$$\mu_{eff} = \frac{\mu_0 + K\mu_B\dot{\gamma}}{1 + K\dot{\gamma}} \tag{3.14}$$

where μ_B , τ_B are the Bingham plastic viscostiy and Bingham yield stress, respectively; μ_0 is the viscosity at very low shear strain rate $\dot{\gamma}$, taken as $\mu_0 = 1000\mu_B$ to ensure numerical convergence and K $= \mu_0/\tau_B$ is a constant parameter.

However, the advantage of the Cross model over the Bingham model is that the effective viscosity is a continuous variable and numerical instability is avoided (Shao &

Lo 2003). Therefore, the Cross model is adopted here as a constitutive model. The shear strain rate $\dot{\gamma}$ in Equation 3.14 is defined in general by the second invariant of the deformation strain E_{ij} as

$$\dot{\gamma} = \sqrt{\frac{1}{2}\sum_i\sum_j E_{ij}E_{ij}}, \; with \; E_{ij} = \frac{\partial v_i}{\partial x_j} + \frac{\partial v_i}{\partial x_j} \qquad (3.15)$$

In two-dimension xy flow, the shear rate $\dot{\gamma}$ is calculated by

$$\dot{\gamma} = \sqrt{2\left(\left(\frac{\partial v_x}{\partial x}\right)^2 + \left(\frac{\partial v_y}{\partial y}\right)^2\right) + \left(\frac{\partial v_x}{\partial y} + \frac{\partial v_y}{\partial x}\right)^2} \qquad (3.16)$$

3.2.2.4 Weakly compressible SPH

The two main approaches to solve the pressure term in modelling viscous flows using SPH, including WCSPH and ISPH, have their own merits and drawbacks. Also, the obtained conclusion on ISPH and WCSPH approaches from several comparison studies is still controversy. For instance, Lee et al. (2008 stated that, under certain circumstances, ISPH performed better than WCSPH for several flows. In contrast, Hughes & Graham (2010) concluded that the results from the WCSPH appeared to be significantly smoother than those from the ISPH. Furthermore, solving the Poisson equation in ISPH is time-consuming (Becker & Teschner 2007). Therefore, WCSPH can be plausibly adopted in this study to compute the pressure term in the governing equation. Tait's equation as modified by Monaghan (Monaghan 1994) to suit bulk fluid flow is used in the simulation, which is given as:

$$P_n = B\left(\left(\frac{\rho_n}{\rho_0}\right)^{\gamma} - 1\right) = \frac{\rho_0 c_s^2}{\gamma}\left(\left(\frac{\rho_n}{\rho_0}\right)^{\gamma} - 1\right) \qquad (3.17)$$

where B is the constant pressure, which governs the relative density fluctuation $\frac{|\Delta\rho|}{\rho_0}$, γ is a power coefficient depending on the material properties, taken as 7, and ρ_0 is the reference density. The numerical speed of sound c_s is taken to be approximately ten times larger than the maximum fluid speed to keep the variation of density below the order of 1% (Cummins & Rudman 1999).

3.2.2.5 Boundary conditions

In SPH, several available techniques are adopted to implement the boundary conditions. The common methods that are used in the literature are the mirror (or ghost) particles method (Cummins & Rudman 1999), the repulsive force method (Monaghan 1994) and the dummy particles method (Shao & Lo 2003). These techniques focus on solving the problem of the lack of particles in the supported range of the kernel function along boundaries, and on deterring fluid particles not to penetrate the boundaries as the boundary is also modelled as separated particles in the SPH technique. A modified repulsive force boundary (Rogers & Dalrymple 2008) is used in this model. In this method, analogous to inter-molecular forces, the boundary particles in the range of the smoothing length h of a particle a will exert central forces when particle a approaches to the boundary as shown in Figure 3.2 (Rogers & Dalrymple 2008). Additionally, a dynamic coefficient of 0.55 Ns/m is implemented to account for the friction between the fresh SC-ECC mix and the wall-boundary (Deeb, Kulasegaram, et al. 2014b; Dhaheer et al. 2016).
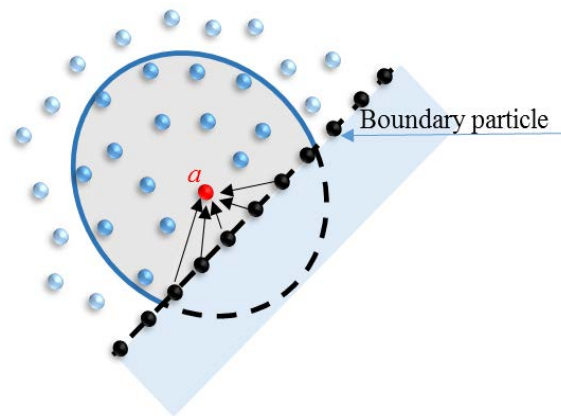
Figure 3.2 Repulsive force from boundary particles to particle a.

3.3 Numerical Simulation Procedures

3.3.1 Fibre modelling

Synthetic fibres, such as PE, PVA with a fine diameter in the range of 0.038 to 0.048 mm used in SC-ECC, are flexible and can be bent or coiled in the mix during the flow of SC-ECC. Notably, several investigations of the motion and shape of flexible fibres in viscous flows have been conducted (Joung et al. 2001; Lindner & Shelley 2015). In a recent study, Yang & Liu (2017) used particle-based method with coupling smoothed particle hydrodynamics (SPH) and an element bending group (EBG) to investigate the dynamics of a flexible fibre interacting with a viscous flow. Fluid and fibre particles were considered as neighbouring particles, and fibre particles were included when calculating the forces acting on fluid particles and vice versa. Adopting this approach, the flexible synthetic fibres in this study are similarly modelled as separated-particles and possess the same continuum properties as mortar particles. In this regard, for a particle, the total number of particles in its smoothing length h of the weighting kernel consists of the total number of neighbouring mortar particles and the total number of neighbouring fibre particles (Figure 3.3). However, in case of particles

within the same fibre, their motions are also influenced by each other. Therefore, a drag force between two adjacent fibre particles is added in the momentum equation (Equation 3.2) to deter them moving apart and to prevent the length of fibre exceeding the initial fibre's length. The tension force acting on particle a from its adjacent particle b of the same fibre is calculated using Equation 3.18,

$$T_{ab} = \begin{cases} EA\left(\dfrac{r_{ab}}{r_{ab}^o} - 1\right)\dfrac{\boldsymbol{r}_{ab}}{r_{ab}} & if\ r_{ab} \geq r_{ab}^o \\ 0 & if\ r_{ab} < r_{ab}^o \end{cases} \tag{3.18}$$

where EA is the tensile rigidity and r_{ab}^o is the initial distance between particles a and b. This force only exerts attractively when two adjacent particles within a fibre recede from each other. If they approach each other, it can be considered that fibres are bent or coiled, and the force equals zero. The parameters of a PVA fibre (length =12 mm, diameter = 39 μm and Young modulus = 42.8 GPa) are used in the simulations (Table 3.1).
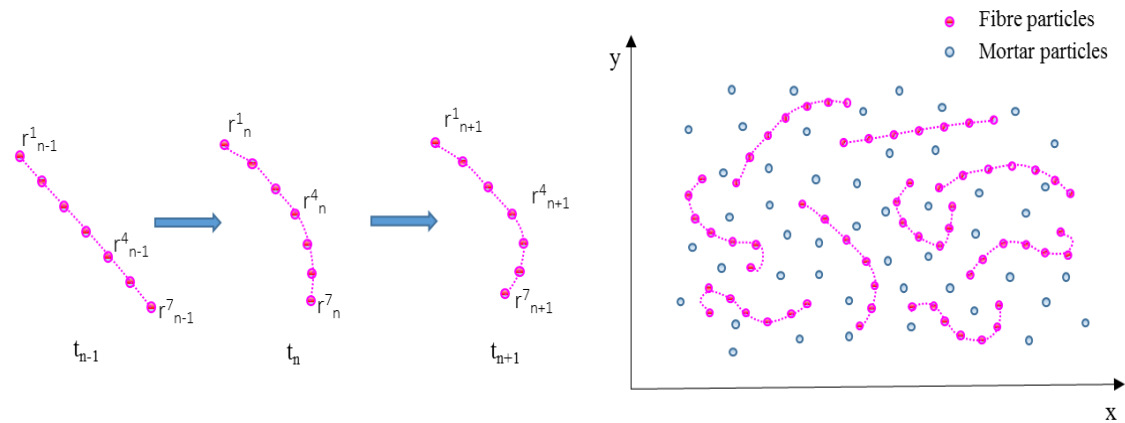
Figure 3.3   Synthetic flexible fibre motion at different time steps t_{n-1}, t_n and t_{n+1}.

3.3.2 Rheology parameters

The flow of shear rate-dependent response materials, such as the self-compacting cementitious composites, are undoubtedly controlled by their rheology behaviour. The

plastic viscosity controls the flow once the yield stress is overcome by the gravitation stress. Hence, to accurately simulate the flow of fresh SC-ECC, these two parameters are necessary. However, the same mix of SCC, it is reported that different rheometers will give diverse results of the yield stress and plastic viscosity (Beaupré et al. 2004), and a broad range of both values have been published (Wallevik & Wallevik 2011; Ferrara et al. 2012; Kostrzanowska-Siedlarz & Gołaszewski 2016). Furthermore, fresh SCC has a nonlinear flow curve and is shearing time-dependent, resulting in the yield stress being inconsistent with the time (Cao & Li 2017). Therefore, other methods to estimate the yield stress and viscosity values of SCC or SFR-SCC have been developed. A micro-mechanical model using a two-phase suspension approach was proposed to estimate the plastic viscosity of SCC and SFR-SCC from the knowledge of cement paste viscosity (Ghanbari & Karihaloo 2009). Badry et al. (2016) employed SPH simulation to estimate the yield stress of SCC from slump flow tests. Lashkarbolouk et al. (2014) used SPH model of V-funnel flow rate tests to determine an appropriate range of plastic viscosities and yield stresses for SCC.

For these reasons and considering the similar intrinsic of SCC and SC-ECC, which are self-compacting under their self-weight, in the scope of this study, the yield stress of SC-ECC is first assumed, and then the plastic viscosity is estimated using SPH simulations in the following two steps:

- Step 1: According to the previous studies (Kulasegaram & Karihaloo 2013; Deeb, Karihaloo, et al. 2014), the yield stress τ_B was assumed to be equal to 200 Pa to model the SCC and SFR-SCC flow. Other studies (Dhaheer et al. 2016; AL-Rubaye et al. 2017; Alyhya et al. 2017), used a range of τ_B from 175 Pa to 190 Pa to simulate the SCC flow. Due to the yield stress being defined as the stress a

SCC/SC-ECC has to overcome to start flowing/deforming under its self-weight, there is a strong correlation between the density of an SCC and the value of its yield stress, as illustrated in (Alyhya et al. 2017). Therefore, with a density of SC-ECC (PVA-ECC) being approximately 2,065 kg/m^3, slightly lower than that of an SCC or SFR-SCC (approximately 2,300-2,400 kg/m^3), the yield stress τ_B of SC-ECC mixes is chosen to be 165 Pa in this study as seen in Table 3.1.

- Step 2: The plastic viscosity of SC-ECC is estimated using an enormous error trial-corrector SPH modelling by comparing the spread of slump flow tests of the SPH simulation with the reported data from experimental studies in the literature. A range of plastic viscosity values μ_B from 5 Pa.s to 80 Pa.s has been used as input parameters for SPH simulation corresponding to τ_B = 165 Pa. The reasonable obtained results are when μ_B was in the range of 5 Pa.s to 40 Pa.s. Then, the plastic viscosity μ_B = 17 Pa.s is selected for using in all the simulations in this chapter (Table 3.1).

Table 3.1 Properties of the SC-ECC mix and polyvinyl alcohol (PVA) fibres.

SC-ECC		PVA	
Density (kg/m^3)	2,065	Young modulus (Gpa)	42.8
Plastic viscosity (Pa.s)	17	Diameter (µm)	39
Yield stress (Pa)	165	Length (mm)	12

3.3.3 Time integration scheme

The predictor-corrector algorithm (Monaghan 1989; 1994) is manipulated to perform the time integration scheme. Denoting the contractive forms of the momentum

and density conversation equations in Equations. 3.1 and 3.2 are $\frac{dv}{dt} = S$, $\frac{d\rho}{dt} = D$; and

of the particle's positon is $\frac{dr}{dt} = V$, where V represents the contribution of the velocity to

the moving of particles. All these time-variant values at time step n are utilised to predict

and correct at the two half-time steps $n + \frac{1}{2}$, and then final values are summarised on

the time step $n + 1$.

At the first half-time step $n + \frac{1}{2}$, intermediate values are predicted as follows:

$$\rho^{n+1/2} = \rho^n + \frac{\Delta t}{2} D^n; \boldsymbol{v}^{n+1/2} = \boldsymbol{v}^n + \frac{\Delta t}{2} \boldsymbol{S}^n; \boldsymbol{r}^{n+1/2} = \boldsymbol{r}^n + \frac{\Delta t}{2} \boldsymbol{V}^n \qquad (3.19)$$

The pressure term is then calculated according to Equation 3.17,

$$P^{n+1/2} = f(\rho^{n+1/2}) \qquad (3.20)$$

Then these variables are corrected using the aforementioned forces at another half-

time step $n + \frac{1}{2}$ as follows:

$$\rho^{n+1/2} = \rho^n + \frac{\Delta t}{2} D^{n+1/2}; \boldsymbol{v}^{n+1/2} = \boldsymbol{v}^n + \frac{\Delta t}{2} \boldsymbol{S}^{n+1/2}; \boldsymbol{r}^{n+1/2} = \boldsymbol{r}^n + \frac{\Delta t}{2} \boldsymbol{V}^{n+1/2} \quad (3.21)$$

The final values at the time steps $n + 1$ are updated as

$$\rho^{n+1} = 2\rho^{n+1/2} - \rho^n; \boldsymbol{v}^{n+1} = 2\boldsymbol{v}^{n+\frac{1}{2}} - \boldsymbol{v}^n; \boldsymbol{r}^{n+1} = 2\boldsymbol{r}^{n+1/2} - \boldsymbol{r}^n \qquad (3.22)$$

The size of the aforementioned time step Δt is normally controlled to satisfy the

Courant, Friedrichs and Lewy (CFL) condition. The time step Δt must be small enough

to be consistent with the number of particles in the computation. Furthermore, it is also

controlled by the effective plastic viscosity which mainly affects the maximum velocity

of the viscous flow. Therefore, the time step size must satisfy the following condition:

$$\Delta t \leq min \left(\frac{\alpha_1 r_{ab}^0}{v_{max}}, \frac{\alpha_2 \rho (r_{ab}^0)^2}{\mu_{eff}} \right) \tag{3.23}$$

where v_{max} is the anticipated maximum velocity of particles and μ_{eff} is effective plastic viscosity. The coefficients α_1 and α_2 are dependent on the selection of the SPH smoothing kernel and are usually on the order of 0.1. These two factors are estimated from the SPH numerical trials to obtain numerical convergence and a realistic flow simulation (Shao & Lo 2003).
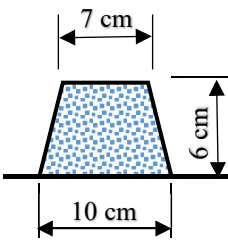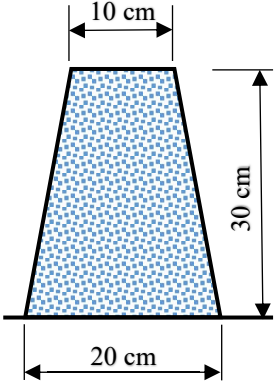
3.4 Simulation Results and Discussions

This section presents 2D numerical simulations of fresh SC-ECC flow in three different tests with different devices. First, slump flow tests with a mini cone and a conventional cone to quantify the deformability and flowability of fresh SC-ECC are simulated. The numerical results are then compared with the experimental data obtained from (Kong et al. 2003b; 2003a; Li & Li 2013). The geometry and dimensions of the device for these tests are shown in Table 3.2. Then, the castings of the beam/slab are simulated to investigate the effect of the casting position, wall-influence to the distribution and orientation of fibres during the flow.

In all models, the mortar particles are primitively arranged in a uniform square grid form with the x-axis and y-axis spacing equal to 0.002 m. Fibre particles are then created randomly with a range of inclined angles up to a maximum of 30 degrees and ensured not to overlap with the mortar particles. The distance between two adjacent fibre particles equals 0.002 m. The fibres are assumed to be straight initially. Theoretically, the number of fibre particles can be calculated based on the number of mortar particles and its volume fraction, i.e., typically 2% for ECC, by applying the geometric

probability. However, to suit the 2D simulation, the number of fibres was rationally calibrated in this study. The total number of particles involved in the computation is represented in Table 3.2. The particles representing the fibres and the mortar form a homogeneous mass and possess the same continuum properties, excepting their assigned number.

Table 3.2   Devices configuration and number of particles represented in the 2D simulations.

Tests	Mini cone test	Conventional cone test
Dimensions of the 2D shapes		
Boundary particles	213	803
Mortar particles	1,221	10,835
Fibre particles	210	1,470
Number of fibres	30	210
Total particles	1,644	13,108

3.4.1 Slump flow test

The slump flow test is recognised as a simple but feasible method to characterise and quantify the workability and flowability of SCC. In this model, both the mini cone

and normal cone slump flow are simulated to investigate the deformability of fresh SC-ECC. The total number of mortar particles and fibre particles used in the mini cone and normal cone are 1,431 and 12,305, respectively. During the cones being lifted up, the fresh mix collapses and spreads under the gravity force. Both cones are lifted up at a speed of 0.1 m/s. The spreads of the SC-ECC mix at several stages of the simulations are shown in Figure 3.4 and Figure 3.5.
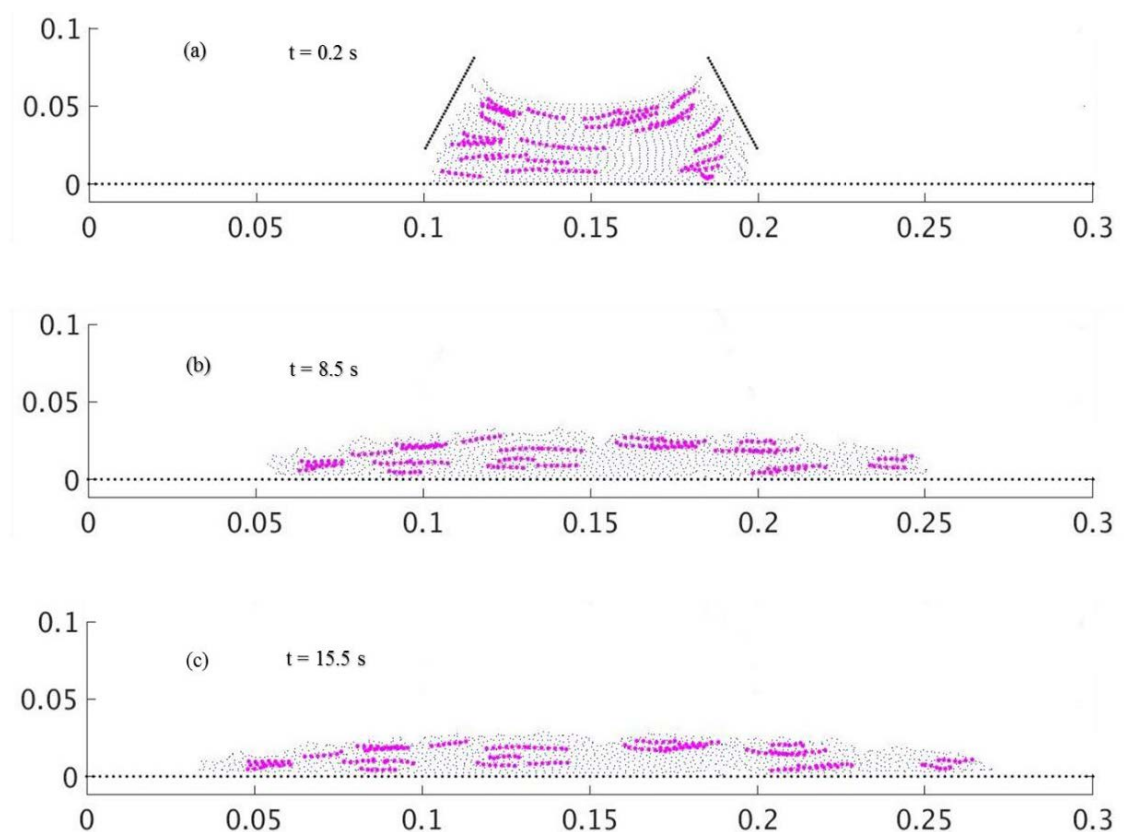
Figure 3.4   Simulation results of mini cone slump flow test.

It can be observed that the flow of the SC-ECC spread to 23.5 cm and 81.5 cm after 15.5 s for the mini cone and normal cone, respectively. Notably, after 15.5 s, the flow of both cone tests still spread with a very low-speed rate, and therefore the simulations could be considered to have stopped at this time. As can be seen in Table 3.3, the numerical results of slump flow tests are comparable with those reported in

experimental studies of Kong et al. (2003a), Kong et al. (2003b) and Li & Li (2013). However, the spreads of the SC-ECC mix in the simulation of the two cone tests are slightly higher than the values recorded in the laboratory, i.e., 21.5 cm for mini cone and 72.9 cm for normal cone. This slight difference can be explained by the lack of contact between the fluid particles with boundary particles in the two-dimensional simulation, which reduces the influence of friction at the boundary. It can also be seen that the flexible synthetic fibres move smoothly along the flow of the cement paste. Some fibres are bent, and others remain aligned as the flow spreads. The fibres near the cone-wall tend to incline or bend due to the high shear stress in this area when the cone is lifted up. In contrast, the fibres in the core region or near the bottom plane tend to align with the flow. These characteristics will be further investigated in next section.
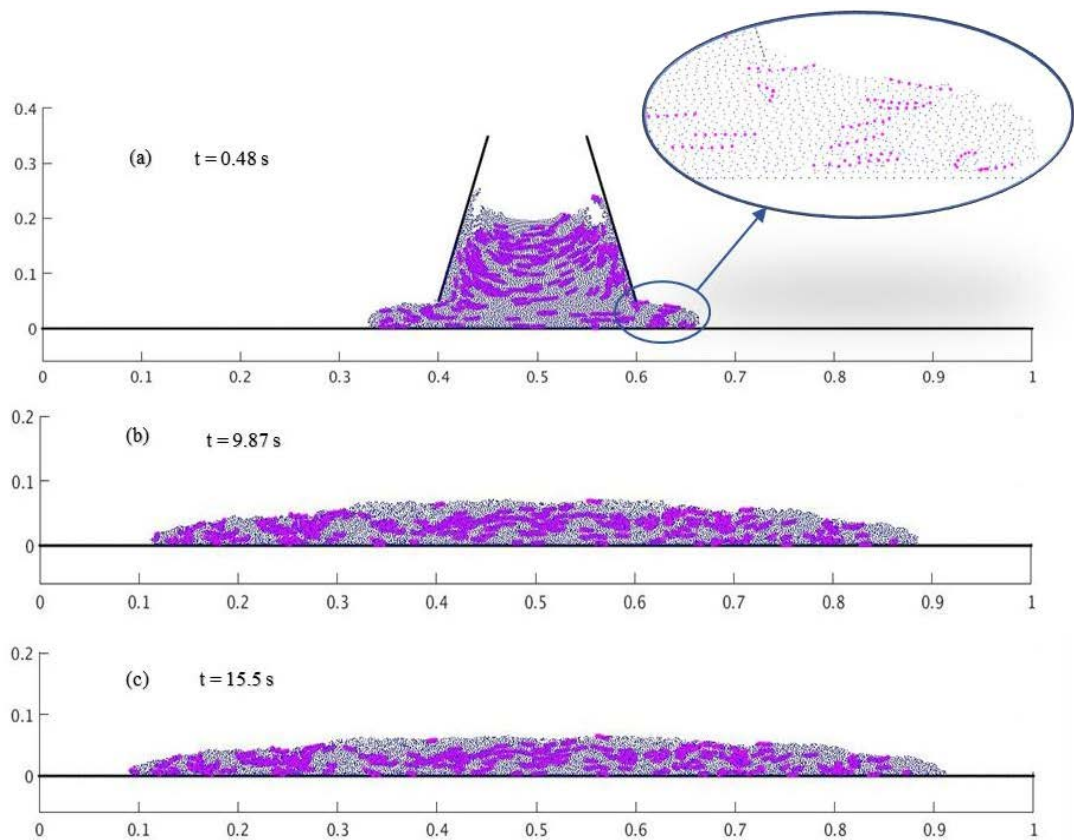
Figure 3.5   Simulation results of the conventional slump flow test.

Table 3.3 Comparison of slump flow tests of SC-ECC (PVA) in the simulation with experimental test data.

Test	Experimental test data			Simulation
	SC-ECC (PVA)	SC-ECC (PE)	SCC	SC-ECC (PVA)
Mini cone test (cm)	21.5 (Li & Li 2013)	18 (Kong et al. 2003b)		23.5 (at 15.5 s)
Normal cone test (cm)	72.9 (Kong et al. 2003a)	60 (Kong et al. 2003b)	60-72 (Kong et al. 2003b)	81.5 (at 15.5 s)
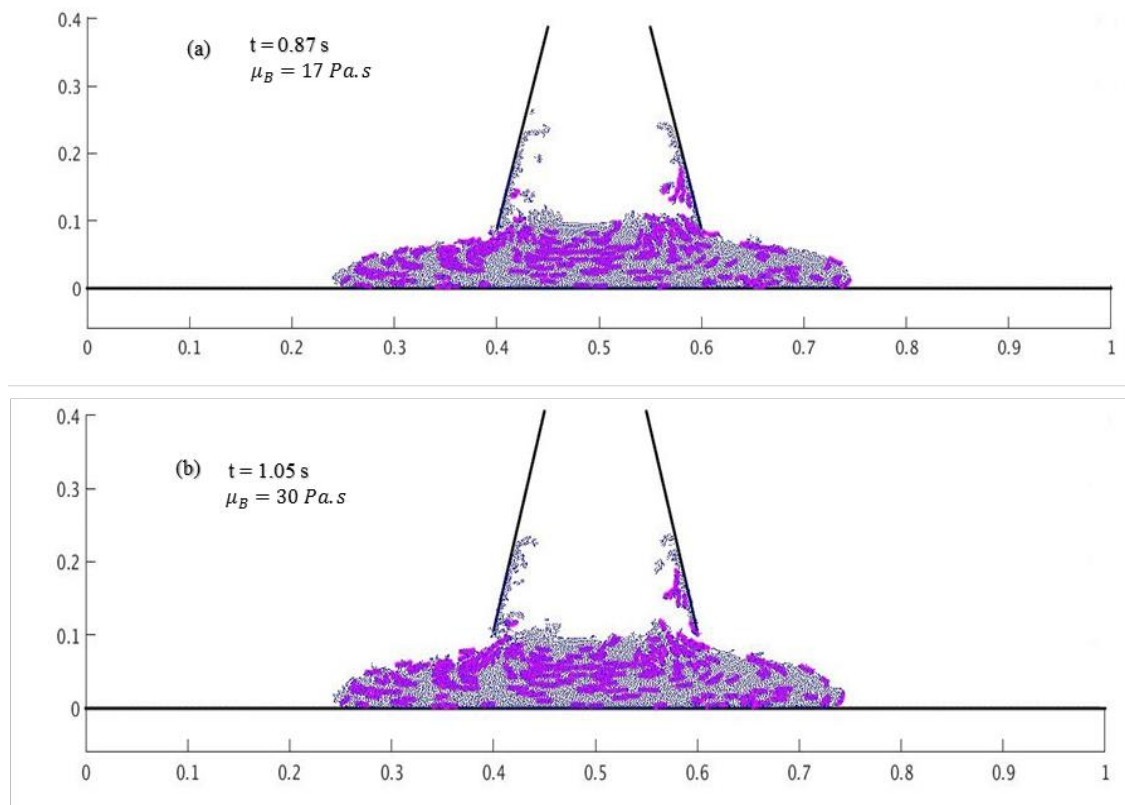
Figure 3.6 Comparison of the flow of the conventional cone test with two plastic viscosity values as it spreads to 50cm: (a) $\mu_B = 17\ Pa.s$; (b) $\mu_B = 30\ Pa.s$.

Furthermore, when the plastic viscosity of the SC-ECC increases (the yield stress is unchanged, = 165 Pa), the flow speed reduces. As shown in Figure 3.6, it takes 0.87 s for the SC-ECC mix with $\mu_B = 17$ Pa. s to reach 50 cm of spread in comparison with 1.05 s of the $\mu_B = 30$ Pa. s mix. When the cone is lifted up, a number of particles are kept on the walls before dropping down due to the fluid-boundary friction, which is exactly what occurred in the laboratory test.

3.4.2 Beam/slab moulding

To investigate the influences of the casting position and the wall-effects on the distribution and orientation of flexible synthetic fibres during the flow of SC-ECC, the mouldings of 2D beam/slab components are simulated. In this simulation, two different casting positions are implemented, one at the end (C1), the other in the middle (C2) of the beam. The specimens are divided into three parts, i.e., (I), (II), (III) for the visualisation on a larger scale, as can be seen in Figure 3.7. The utilised number of particles in the computation are 48,149 mortar particles and 2,800 fibre particles (equivalent 400 fibres). The random dispersion and initial inclined angle of fibres are similar to those in cases C1 and C2.
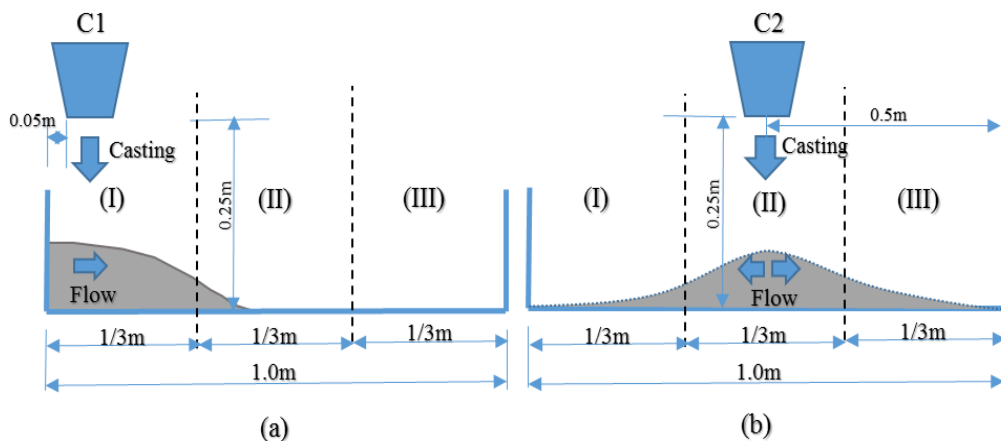
Figure 3.7 (a) Cast at the end of the mould, (b) Cast in the middle of the mould.

Figure 3.8 and Figure 3.9 represent three parts of the completed casting of the case C1 and case C2. It can be seen in all parts of the two cases casting C1&C2 that the fibres tend to align in the bottom area and near the bottom wall, which is beneficial for enhancing the flexural strength of beam/slab elements. This result agrees well with the conclusion from the previous studies (Alberti et al. 2018b). This region is known as the high shear stress/low velocity area due to the fluid-bottom boundary interaction, as seen in Figure 3.10. The fibres also tend to orient parallel to the bottom wall near the casting position, which enhances the orientation factor of the fibres in these areas. The remarkably similar results can also be found in (Alberti et al. 2016). Moreover, it can be observed that the flow tends to push fibres more towards the bottom plane in the range under the outlet of the funnel.
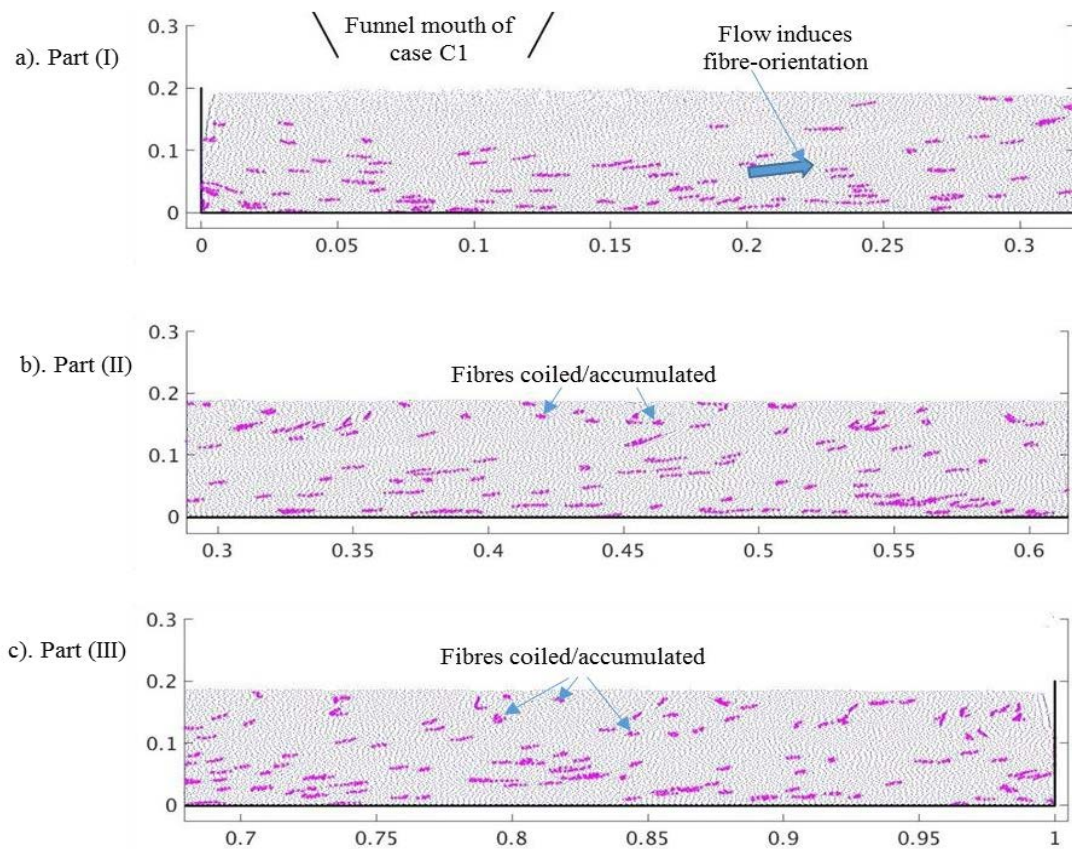
Figure 3.8 Three parts of the completed casting specimen of case C1 shown on a large scale: (a) Part I (at the end), (b) Part II (in the middle), (c) Part III (at the other end).
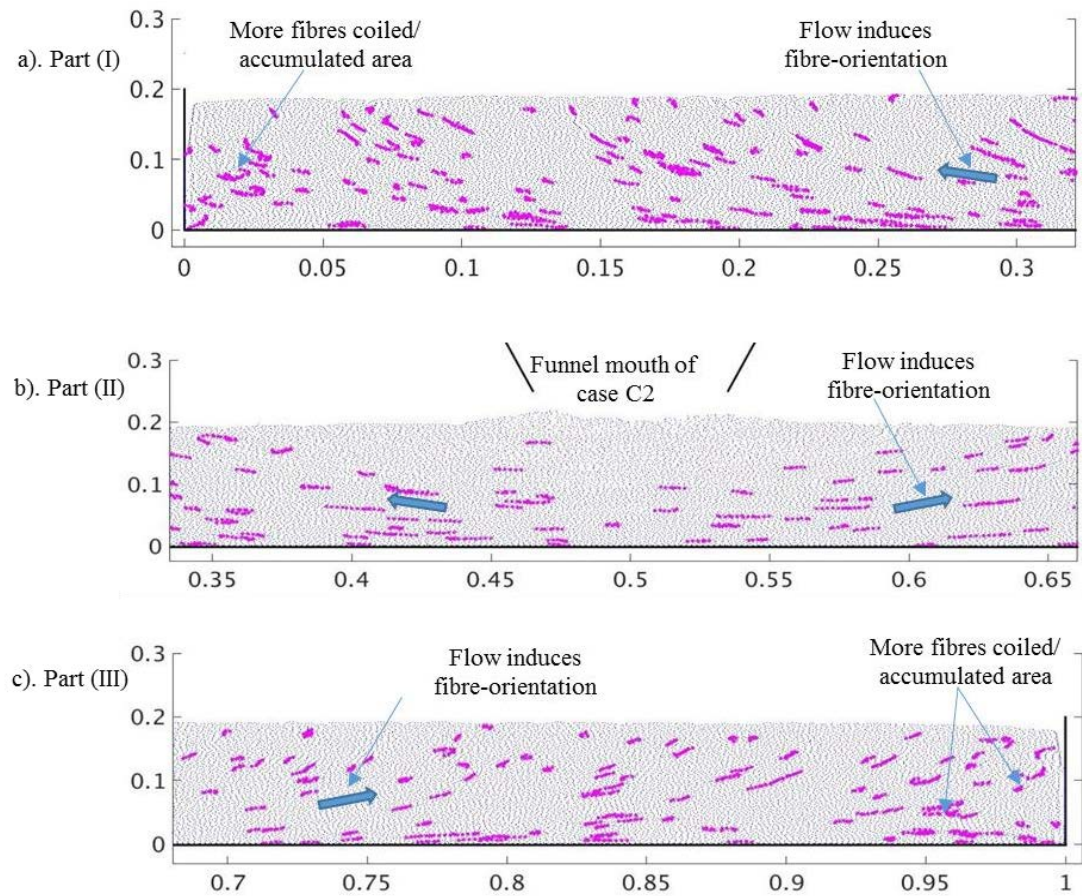
Figure 3.9   Three parts of the completed casting specimen of case C2 shown on a large scale:

(a) Part I (at the end), (b) Part II (in the middle), (c) Part III (at the other end).

Far from the casting position, the flow induces the fibre orientations upward to the surface. This phenomenon agrees well with the observation in the experimental study (Van Mier et al. 2013). Moreover, the fibres tend to coil near the end-vertical walls area of the formwork, where the flow of fresh SC-ECC may become disorderly as the flow reached the vertical walls and is pushed back. In comparison with case C1, more fibres concentrate at the vertical end walls when the casting position is located in the middle of the specimen (case C2). This result is because the magnitude of the flow velocity when it reaches to the walls in case C2 is larger than that in the case of C1 (Figure 3.10). The fibres also tend to coil near the surface of the specimen, where the fluid flow has a

higher velocity/lower shear stress than that in the middle zone or at the bottom area of the formwork (Figure 3.10). This feature contrasts with a recent numerical study, which assumed that the rotation of fibres was constrained and remained straight at a free surface flow (Lu & Leung 2017a). Notably, the dispersion of fibres in case C1 is generally somewhat better than that in case C2 with the same initial random dispersion and orientation of fibres.
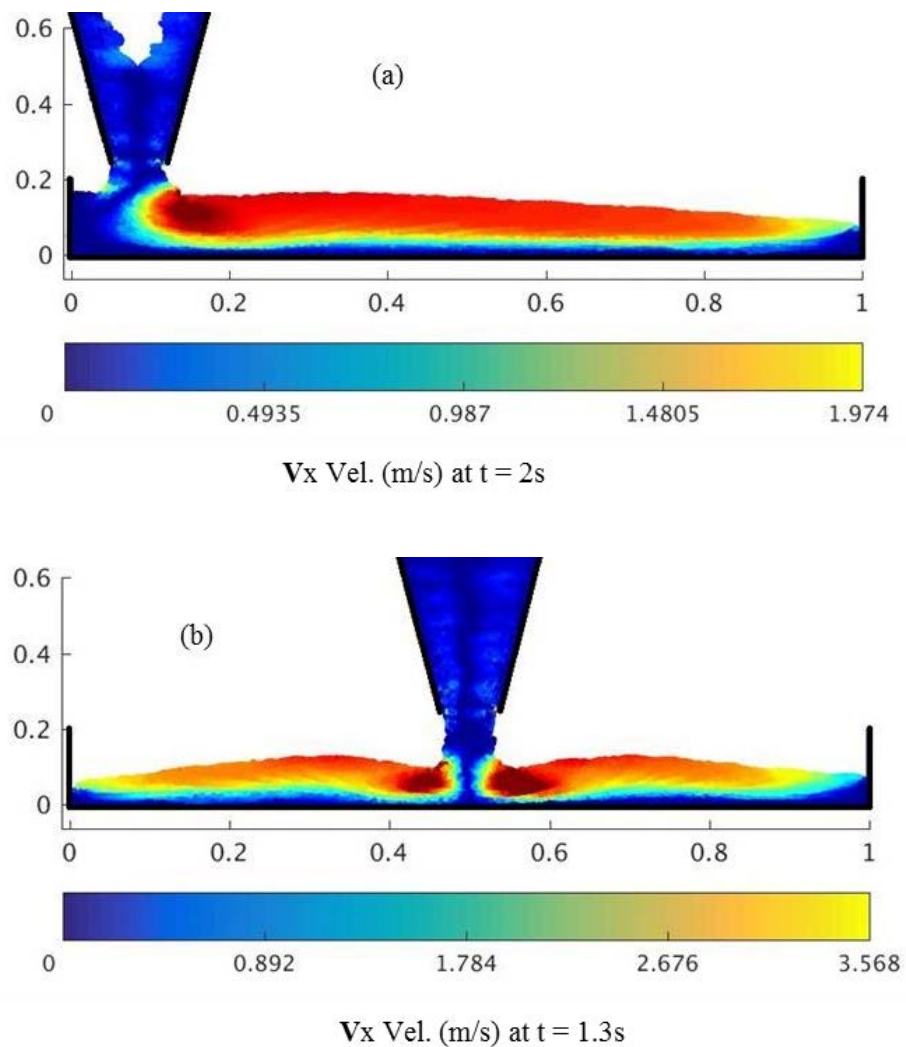
Figure 3.10   Magnitude of the longitudinal velocity when the flow reached the vertical walls: (a) Case C1, (b) Case C2.

3.5 Conclusions

This chapter presents the 2D simulation of a fresh SC-ECC flow by coupling the Lagrangian Navier-Stokes constitutive equations of a non-Newtonian viscous fluid with the WCSPH methodology. The SC-ECC flow, which discretised by representative particles of synthetic fibres and mortar, is described using the Cross rheology model. The reasonable agreement between the experimental data in the literature and the simulation results of the slump flow tests validate the proposed numerical method. The study results also demonstrate that flexible synthetic fibres used in SC-ECC can be modelled as separate mortar particles in the computational domain to simulate the flow of SC-ECC. This novel approach has potential to be used to optimise the distribution and orientation of the flexible synthetic fibres through controlling the casting process in order to gain the desired strength of SC-ECC structural members.

The proposed method provides insight into the distribution, orientation of flexible synthetic fibres in the beam/slab specimen during the casting process of SC-ECC. In this study, the fibres tend to be parallel to the bottom of formwork near the casting position, near the bottom wall and tend to coil near the end-vertical walls and at the surface of the specimen. Additionally, the influence of the flow on the fibres orientation and distribution diminished with the increase of the distance of flow from the casting position.

However, some drawbacks associated with the 2D simulation need to be overcome to obtain a real picture of the flow of SC-ECC and the motion of the flexible fibres. One of the main drawbacks of the aforementioned simulations is that the maximum inclined angles of fibres were assumed to be 30º, but it might vary from 0º to 90º in reality. The

reason for this assumption is that a larger inclined angle leads to more fibres intersecting each other in a single plane, which may result in more fibres accumulating and thus travelling together. Another disadvantage is that the number of fibres was also calibrated to suit the 2D simulation. Hence, the development of a 3D model to simulate the flow of SC-ECC is necessary and this will be further investigated and presented in the next chapter.

Chapter 4

Flow of Self-Consolidating ECC with V-Funnel and U-Box

4.1 Introduction

In both laboratory and field practice, the self-consolidating characteristics of fresh SC-ECC is quantified by using several standard tests. These tests, similar to ones applied for self-compacting concrete (SCC) (Okamura & Ouchi 2003), include deformability tests using slump cone flow, flow rate test using a V-funnel device, and self-placing test using a U-box with reinforcing steel as obstacles to SC-ECC flow (Kong et al. 2003b; 2003a; Lepech & Li 2008). The measured indices, which reflect the rheological properties of SC-ECC, help to evaluate the flowability, filling and passing abilities of an SC-ECC mixture. Apparently, these tests have to be repeated for different mixtures and therefore it is costly and labour-intensive. Moreover, the observation of fibres movement during testing processes, which might help to predict the distribution and orientation of fibres in structural elements, is unattainable.

In the previous chapter, the flow of SC-ECC is modelled in slump cone tests in two dimensions using weakly compressible smooth particle hydrodynamics (WCSPH) to solve the Lagrangian form of Navier-Stokes constitutive equations. The synthetic fibre was considered as flexible and modelled as separated particles, possessing the analogous continuum properties with mortar particles in the domain of SC-ECC. Within a fibre, the drag force was added in the momentum equation between two adjacent fibre particles to ensure they travel together. The results of the proposed model were encouraging after a comparison with the recorded data from the experiment studies. However, the results from two-dimensional simulations are somewhat inaccurate since the interaction between particles restricted to a single plane. The calibration of the fibre number and its inclined angle to suit the 2D model also affected the real picture of SC-ECC flow. To obtain the factual image of the SC-ECC flow, the actual distribution and

orientation of synthetic fibres in fresh mixture, the development of a three-dimensional model is essential. In addition, the SPH approach has been successfully implemented for simulating the SCC flow in three-dimension of the V-funnel (Alyhya et al. 2017). The contribution of this simulation was emphasised regarding the casting process of SCC in the precast factory by rectangular hopper.

This chapter aims at developing a 3D model for simulating the flow of SC-ECC, which is validated using the V-funnel and U-box tests, by extending the approach of SPH. The filling and passing ability of SC-ECC in these principal tests will be numerically examined through the proposed model. The rheology behaviour of SC-ECC and its influence on the flow characteristics will also be revealed. More importantly, the dispersion/orientation of synthetic fibres in the mix can be observed during the flow of fresh SC-ECC in these tests. This observation might be helpful in predicting the orientations of flexible synthetic fibres and their distribution, which have great influences on the performance of ECC materials (Zhou et al. 2012; Kanakubo et al. 2016), in the structural elements using SC-ECC.

The flow rate of SC-ECC mix is simulated by filling the V-funnel with mortar and fibre particles, and then allowing the material particles to flow through the funnel-outlet until the time when the material particles completely vacate the bottom outlet of the funnel. With the recent development in 3D printing for modern construction, an ECC material with self-reinforced characteristic has been developed aiming to reduce or eliminate steel bars in printed structures (Soltan & Li 2018). While there are differences in initial flowability and harden time of this material with SC-ECC (Soltan & Li 2018), the ability to continuously extrude through a small nozzle at the printing head is somewhat similar. In this regard, the V-funnel modelling can be a further advantage in

predicting the extruding ability, the printing time and the orientation of synthetic fibres of printable ECC materials in 3D printing elements.

On the other hand, the U-box is a vital device to verify the self-consolidation of fresh SC-ECC, and to exam the passing ability of fresh material through obstacles, i.e., steel bars. The U-box simulation is performed by filling one of the chambers with fresh SC-ECC particles, then allowing material particles flow to the adjacent chamber after passing the rebar obstructions until the time when the flow stops levelling. Notably, the combination of ECC materials with steel reinforcement has proved the capability to enhance the performance of structural elements (Fischer & Li 2007; Meng, Lee, et al. 2017). However, based on the authors' knowledge, the influence of steel bars on the dispersion or orientation of synthetic fibres used in ECC has not been studied yet. This issue is crucial for the case of flowable materials using flexible synthetic fibres like SC-ECC. Hence, the simulation of the U-box test in this study will be an advantageous approach to examine the effect of steel reinforcements on the SC-ECC flow, the dispersion and orientation of flexible synthetic fibres.

The simulation results of the two tests are then validated using the data obtained from the experimental studies in the literature. The successful simulation of these two standard tests will confirm the correctness and effectiveness of the 3D model and open a gateway in optimizing the distribution/orientation of the flexible synthetic fibres in structural elements using SC-ECC materials. The developed model can be used to simulate the casting process of SC-ECC into different moulds with different technique to achieve optimal values of fibres dispersion and orientation coefficients, helping to obtain the desired performance of structural elements. This approach could save a

massive amount of materials and efforts, enhance the application of SC-ECC materials in the building industry.

4.2 Model Development

4.2.1 Constitutive rheology model

The flow of SC-ECC is classified as a non-Newtonian fluid, which is governed by its rheology behaviour. The plastic viscosity controls the flow once the gravitation stress overwhelms its yield stress. During its flow, the relation between the shear stress tensor $\boldsymbol{\tau}$ and strain tensor $\boldsymbol{E}$ is expressed as:

$$\boldsymbol{\tau} = \mu_{eff}\boldsymbol{E} \tag{4.1}$$

where μ_{eff} is the effective viscosity. Being a continuous variable in a non-Newtonian viscous fluid, the effective viscosity can be expressed through the Cross rheology model (Shao & Lo 2003) as:

$$\mu_{eff} = \frac{\mu_0 + K\mu_B\dot{\gamma}}{1 + K\dot{\gamma}} \tag{4.2}$$

where μ_0 denotes the viscosity at the very low shear strain rate $\dot{\gamma}$, μ_0 is taken as $1000\mu_B$ to ensure numerical convergence and K = μ_0/τ_B is a constant parameter; μ_B , τ_B are the Bingham plastic viscosity and the Bingham yield stress, respectively. In three-dimension xyz flow, the shear rate $\dot{\gamma}$ is calculated by:

$$\dot{\gamma} = \sqrt{2\left(\left(\frac{\partial v_x}{\partial x}\right)^2 + \left(\frac{\partial v_y}{\partial y}\right)^2 + \left(\frac{\partial v_z}{\partial z}\right)^2\right) + \left(\frac{\partial v_x}{\partial y} + \frac{\partial v_y}{\partial x}\right)^2 + \left(\frac{\partial v_x}{\partial z} + \frac{\partial v_z}{\partial x}\right)^2 + \left(\frac{\partial v_y}{\partial z} + \frac{\partial v_z}{\partial y}\right)^2}$$

$$\tag{4.3}$$

4.2.2 Modelling of SC-ECC flow with SPH

The SPH method starts with discretising the whole SC-ECC domain using a limit amount of separated particles, and each particle possesses material properties. For a current particle a, the approximation of field variables is figured out by a summation of all the values of particles b in its dominant range κh based on a smoothing kernel W (Shao & Lo 2003) *or* its correction form $\widetilde{W}$ (Gomez-Gesteira et al. 2012) (Figure 4.1). Then the Lagrangian form of Navier-Stokes constitutive equations, considering the thermal term being constant all over the computational process, can be written in the SPH forms as following:

$$\frac{d\rho_a}{dt} = \sum_b m_b (\boldsymbol{v}_a - \boldsymbol{v}_b) \nabla_a \widetilde{W}_{ab} \tag{4.4}$$

$$\frac{d\boldsymbol{v}_a}{dt} = -\sum_b m_b \left(\frac{P_a}{\rho_a^2} + \frac{P_b}{\rho_b^2} \right) \nabla_a \widetilde{W}_{ab} + \boldsymbol{g} + \sum_b m_b \left(\frac{\boldsymbol{\tau}_a}{\rho_a^2} + \frac{\boldsymbol{\tau}_b}{\rho_b^2} \right) \nabla_a \widetilde{W}_{ab} \tag{4.5}$$

where P, ρ and t represent the pressure force, particle density and time, correspondingly. The vector form of the velocity, the gravitational acceleration and the shear stress tensor are denoted by $\boldsymbol{v}$, $\boldsymbol{g}$ and $\boldsymbol{\tau}$, respectively. The subscript a and b represents the current particle a and surrounding particle b. The term, $\nabla_a \widetilde{W}_{ab}$, is the gradient of the corrected kernel taken with regard to positions of current particle a.

The cubic spline kernel is also used in this simulation due to its stability and accuracy. The value of its influence range κh is selected to be 1.5 times of initial distance between discretised particles. This value is to ensure the smoothing performance of SPH code and the computational time is acceptable. Additionally, the artificial viscosity

proposed in (Monaghan 1992) is also employed here to stabilise the numerical algorithm.
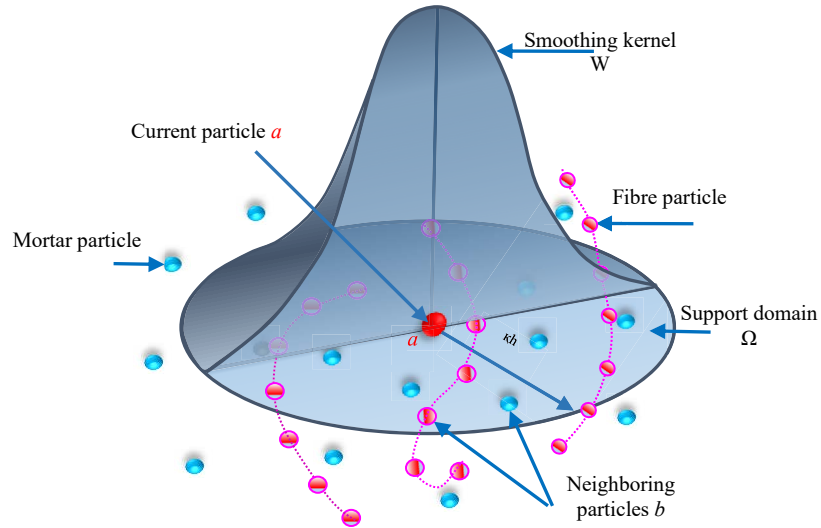
Figure 4.1   Smoothing kernel W and its support domain for the approximation of a current particle *a*.

In reality, fresh cementitious materials always enclose tiny air bubbles (Cao & Li 2017), which mean that their density might slightly fluctuate due to some air escape during the flow. Therefore, a weakly compressible SPH (WCSPH), developed in (Monaghan 1994), can be reasonably implemented here to calculate the pressure term *P* in the governing equations of SC-ECC flow. The modification to suit the flow of bulk fluid of Tait's equation (Monaghan 1994) is also used in this 3D simulation. The predictor-corrector algorithm described in (Monaghan & Kos 1999) is manipulated to track the flow. The procedure of time integration scheme is represented in the flow chart as shown in Figure 4.2. All these time-variant values at time step *n* are used to predict and correct at the two half-time steps *n + ½,* and then final values are summarised on the time step *n + 1*. The *D, S* and *V* are the contractive forms of the density conversation

in Equation 4.4, the momentum in Equation 4.5 and the involvement of the velocity to the movement of mortar and fibre particles, respectively.

1. Step1: Prediction step:

$$\rho_{n+1/2} = \rho_n + \frac{\Delta t}{2} D_n;$$

$$\boldsymbol{v}_{n+1/2} = \boldsymbol{v}_n + \frac{\Delta t}{2} \boldsymbol{S}_n;$$

$$\boldsymbol{r}_{n+1/2} = \boldsymbol{r}_n + \frac{\Delta t}{2} \boldsymbol{V}_n;$$

Calculate pressure P:

$$P_{n+1/2} = \frac{\rho_0 c_s^2}{\gamma} \left(\left(\frac{\rho_{n+1/2}}{\rho_0} \right)^{\gamma} - 1 \right)$$

2. Step2: Correction step:

$$\rho_{n+1/2} = \rho_n + \frac{\Delta t}{2} D_{n+1/2};$$

$$\boldsymbol{v}_{n+1/2} = \boldsymbol{v}_n + \frac{\Delta t}{2} \boldsymbol{S}_{n+1/2};$$

$$\boldsymbol{r}_{n+1/2} = \boldsymbol{r}_n + \frac{\Delta t}{2} \boldsymbol{V}_{n+1/2};$$

3. Final step:

$$\boldsymbol{v}_{n+1} = 2\boldsymbol{v}_{n+1/2} - \boldsymbol{v}_n$$

$$\rho_{n+1} = 2\rho_{n+1/2} - \rho_n$$

$$\boldsymbol{r}_{n+1} = 2\boldsymbol{r}_{n+1/2} - \boldsymbol{r}_n$$
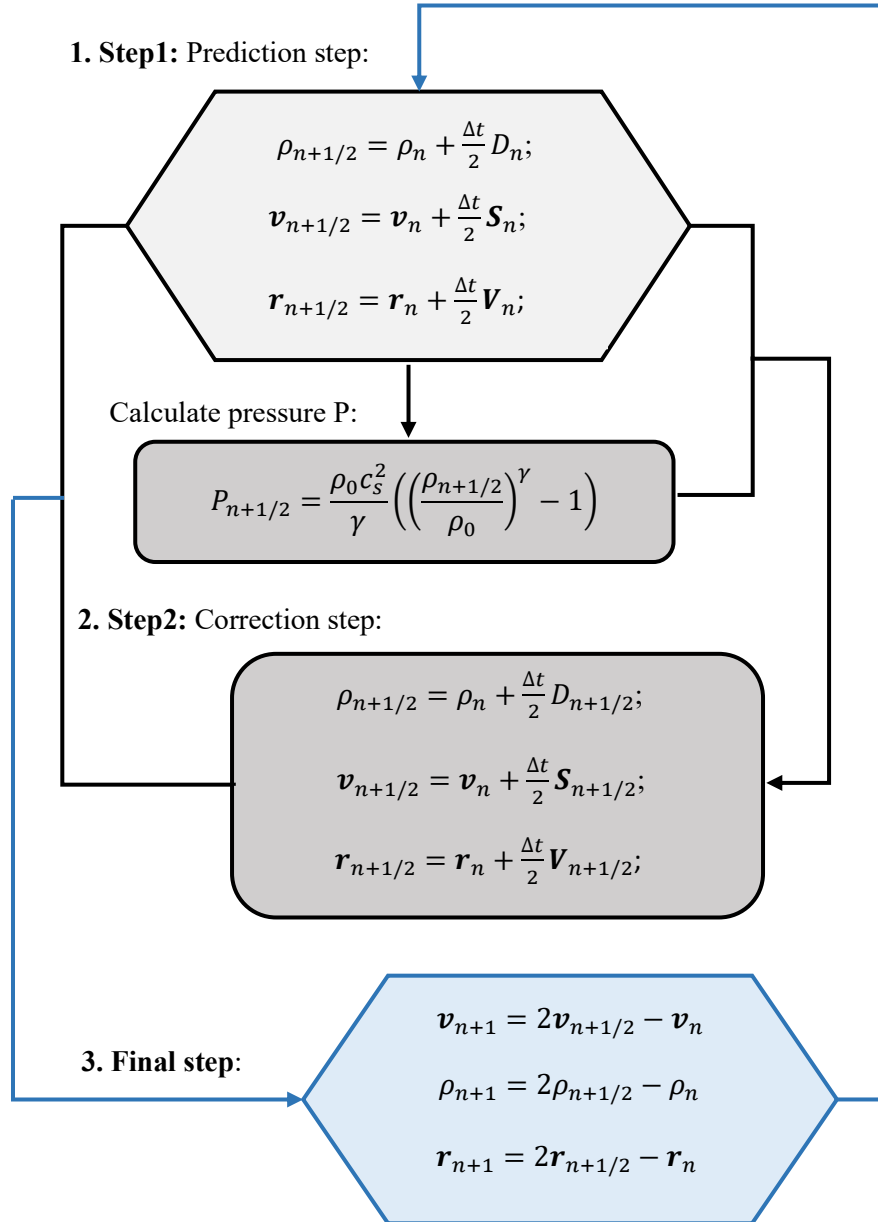
Figure 4.2   Flow chart of three steps of predictor-corrector algorithm.

4.2.3 Flexible synthetic fibre modelling

The SPH methodology requires discretizing the computational domain by a set of particles, with each particle possessing material properties depending on the problem.

Therefore, it is feasible and appropriate to model flexible synthetic fibres as separated particles in a viscous flow. In this regard, the mortar and fibre particles are considered as neighbor-particles, thus being involved in the calculation of the acting forces on each other. This methodology has been demonstrated its accuracy in the simulation of the flow of SC-ECC in two dimensions in previous chapter. The highlights of this method are summarised as bellow:

- Flexible synthetic fibres are modelled as separate particles, and each particle possesses the analogous continuum properties to mortar particles.

- Within a fibre, a drag force between two adjacent particles is added into the momentum equation each time step to prevent them from moving apart and exceeding its prescribed length.

- A fibre is considered as being bent or coiled if two neighboring fibre particles within a fibre approach each other.

4.2.4 Boundary particle condition

The modified repulsive force boundary (Rogers & Dalrymple 2008), which was successfully implemented in 2D simulation, is also implemented. In this method, a particle *a* will be exerted the repulsive forces from the boundary particles in its influence range when it approaches to the boundary. However, in 3D simulation, the number of involved boundary particles exerting repulsive forces to an approached mortar/fibre particle *a* are much larger than that in 2D (Figure 4.3). As can be seen Figure 4.4a, the robust repulsive force from boundary particles in 3D simulation tend to push the inside material particles moving upward initially. To account for this problem, a coefficient α_D is added in the original equation of (Rogers & Dalrymple 2008) as:

$$\boldsymbol{f}_e = \alpha_D \boldsymbol{n} R(y) P(x) \varepsilon(z, u_\perp) \tag{4.6}$$

where $\boldsymbol{f}_e$ and $\boldsymbol{n}$ are the vectorial form of the repulsive force and the normal of the reference boundary. α_D is equal to 1 in 2D and $r_0/h\pi$ in 3D with r_0 is the distance between two boundary particles. Figure 4.4b illustrates the efficiency of α_D in reducing the repulsive force of boundary particles in 3D simulation, which ensuring the accuracy of the code.

The repulsion function, R(y), is calculated based on the normalises distance q = y/2h, where y is the perpendicular distance of the particle a from the boundaries. $\boldsymbol{n}$ P(x) is a function to ensure exerting forces remain constant when a particle a travel parallel to the boundary, in which x is the projection of its interpolation location onto tangent of boundaries. The function $\varepsilon(z, u_\perp)$ is to adjust the force magnitude according to the local depth $\varepsilon(z)$ of particle, and to adjust the velocity of fluid particles $\varepsilon(u_\perp)$, which normal to the boundary (Gomez-Gesteira et al. 2012).
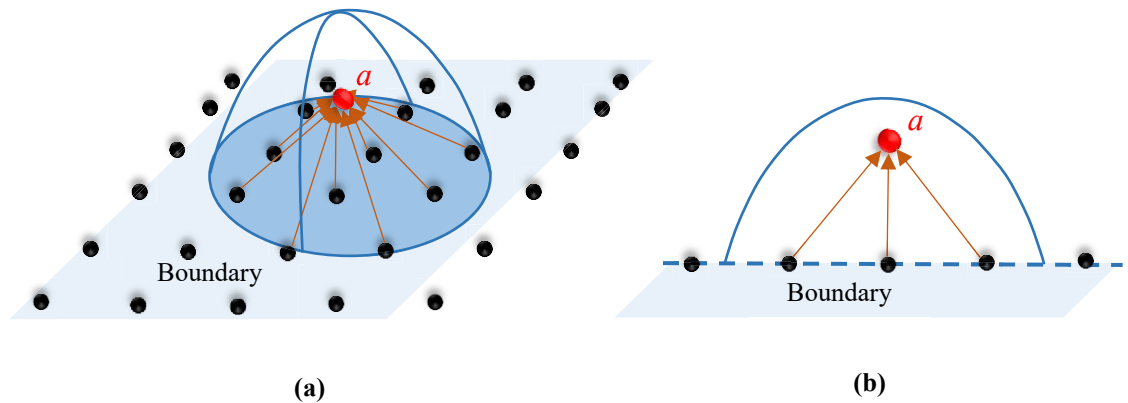
Figure 4.3 Repulsive force from boundary particles to particle a: (a) in 3D simulation; (b) in 2D simulation.
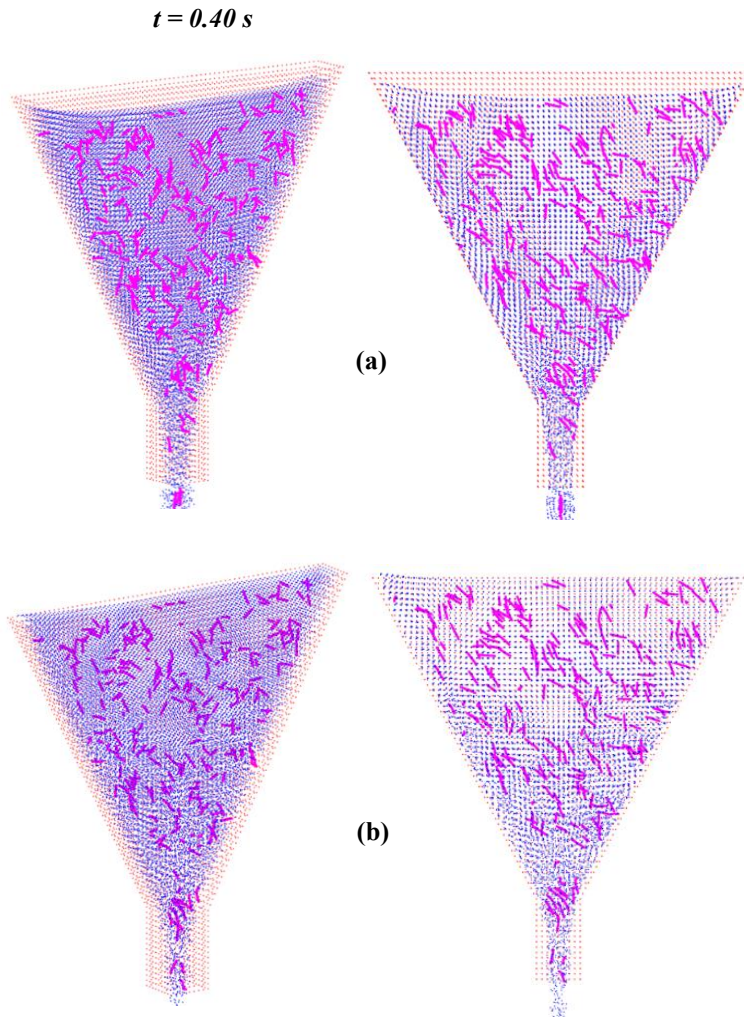
t = 0.40 s

Figure 4.4 Comparison of the repulsive force boundary at t = 0.40 s: (a) before implementing α_D; (b) after implementing α_D.

4.3 Initial Configuration for Computational Efficiency

It can be noticed that excessive computational time is one of the main drawbacks of the SPH methodology. In SPH simulation, each particle might interact with dozens of particles in 2D to hundreds of surrounding particles in 3D, depending on the solution of selective kernel W and its smoothing length h. More interactions between particles might result in a significant increase in time to complete each step in 3D simulation in comparison with the 2D modelling. Therefore, the implementation of a high-performance computer using single central processing unit (CPU) for serial SPH codes

and multiple CPUs or graphics processing units (GPUs) for parallel SPH codes are required (Crespo et al. 2015).

By balancing the computational time of the serial SPH codes used in this study with the accuracy and the smoothing performance of the simulations, the mortar particles are initially created in a uniform square grid form with the x-axis, y-axis and z-axis spacing equal to 0.004 m. This value is two times larger than that of the 2D simulations used in (Thanh et al. 2019). Fibre particles are then generated randomly with a range of inclined angles from 0 to 90 degrees. The space between the two neighboring particles of a fibre is chosen to be equal a half of the initial distance of mortar particles to facilely observe the shape of fibres. This means that one PVA fibre used in this study (length = 12.0 mm) is represented by seven-separated particles. Initially, particles of one synthetic fibre are created in a straight line and ensured not to overlap with the mortar particle. The amount of fibre is determined based on the number of mortar particles and its volume fraction, typically a 2% for ECC. Table 4.1 reveals the number of mortar, fibre and boundary particles involved in the computations. The particles representing the fibres and mortar possess the same continuum properties and form a homogeneous mass. The configuration of the devices and initial created particles for these two simulations are shown in Figure 4.5 and Figure 4.6.

(a)   (b)
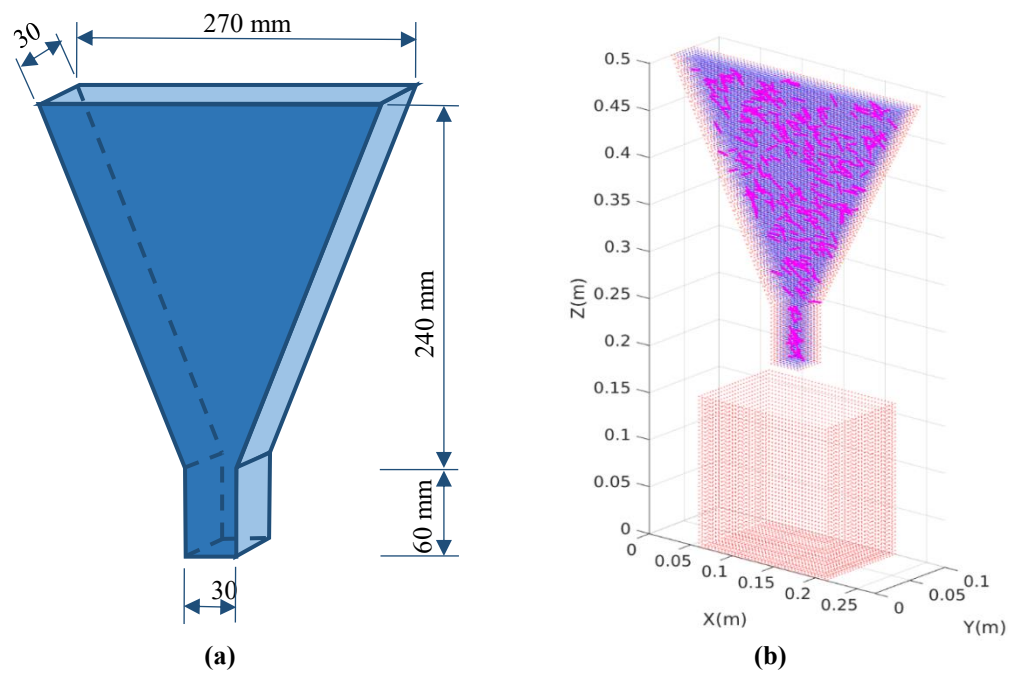
Figure 4.5 (a) V-funnel configuration; (b) Repulsive force boundary particles, initial generated mortar and random fibre particles.

(a)   (b)
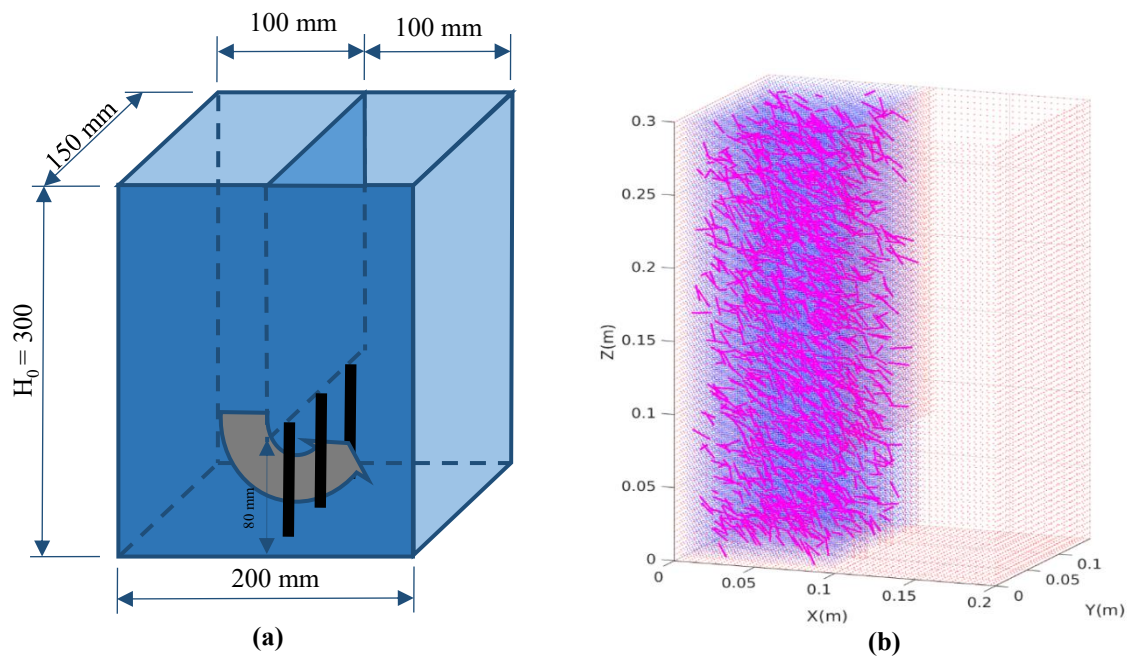
Figure 4.6 (a) U-box vessel configuration; (b) Repulsive force boundary particles, initial generated mortar and random fibre particles.

Table 4.1   The measured indices and the number of particles involve in simulations

Tests	V-funnel	U-box vessel
Measured indices	R=10/t	L=2H/H_0
Boundary particles	12,204	19,476
Mortar particles	16,324	64,800
Fibre volume fraction (%)	2.0	2.0
Number of fibres	326	1,296
Fibre particles	2,282	9,072
Total particles	30,810	93,348

4.4 Simulation Results

This section presents the results of the numerical simulations of the SC-ECC flow in V-funnel and U-box models. The material properties utilised as input data for these simulations are the same as in chapter 3. The parameters of PVA fibre are used in the two models. The values of two-rheology parameters, i.e., the plastics viscosity μ_B and the yield stress τ_B are selected as the previous chapter. These simulations are performed on a cluster computer (3.4 GHz Intel Xeon E5-2687W-8 Cores, 25Mb L3 Cache), and the time to process 12.5 s computational predetermination of the V-funnel test and U-box test are approximately 71 hours and 150 hours, respectively.

4.4.1 V-funnel test

The flow rate of SC-ECC is simulated by filling the V-funnel with square-grid mortar particles and random-inclined fibre particles, allowing the material particles to

flow through the funnel-outlet under the gravitational force. In this simulation, total number of 12,204 particles represents for the repulsive boundary of V-funnel and container box. In the meantime, 16,324 mortar particles and 326 fibres (2,282 fibre particles) are created for representing the material. The completing time, t, is when the material particles accomplished exudes from the bottom outlet of the funnel. The flow rate index, R, is calculated based on the measured time t as $R=10/t$.

Figure 4.7 presents the obtained flow patterns of a SC-ECC mix from the numerical model at three time steps. To clarity, fibre particles are plotted separately with the mortar particles in analogous time steps. After 11.2 seconds, the material particles completely vacate through the bottom outlet of V-funnel (Figure 4.7c). This discharge time of the numerical modelling agrees very well with the experimental data reported in (Kong et al. 2003b; Mohammed et al. 2017), and the value of flow rate index, R= 0.89, is also in the allowable range of SCC (Ozawa 1995), as presented in Table 4.2. It can be seen that the flexible synthetic fibres move smoothly along the flow of the cement paste particles. Most of the fibres are observed as being bent in the container box after travelling (Figure 4.7c). It can be also observed that the magnitude of vertical velocity of the flow decreases following the reduction of the pressure of gravitational force during the flow (Figure 4.7a and Figure 4.7b) except for the time when the last particles vacate the outlet of the funnel (Figure 4.7c).

(a) t = 0.48 s

(b) t = 5.72 s

(c) t = 11.20 s
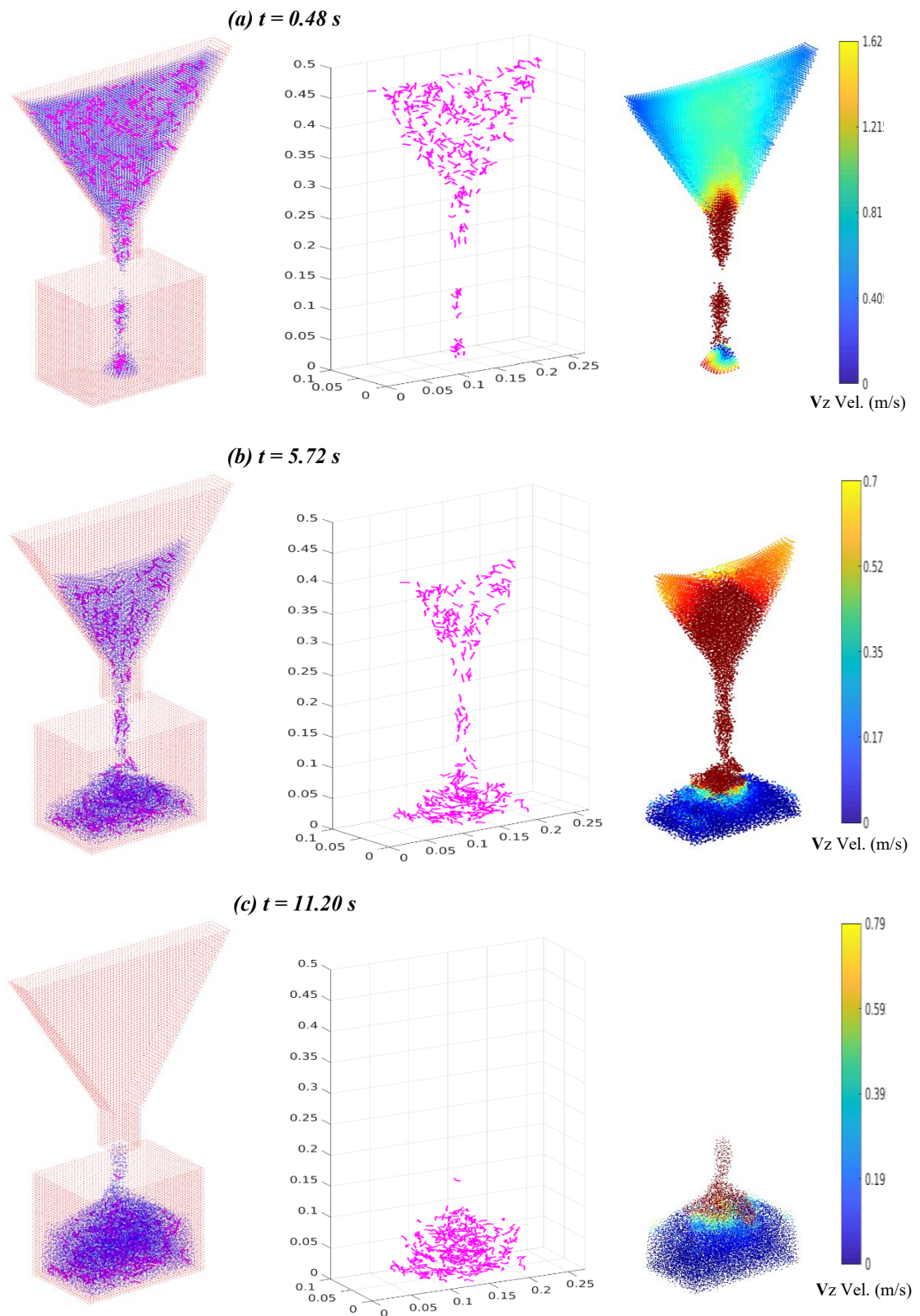
Figure 4.7   Numerical simulation results of the V-funnel test at different time steps.

Notably, due to the significant increase of particles interaction between mixture and wall-boundary in the 3D model, the dynamic coefficient that was used in the 2D model (0.55 Ns/m) becomes unsuitable for applying here. In 3D, this coefficient value leads to high friction between boundary particles and approached fluid particles, which then critically restrains the flow of SC-ECC, particularly near the wall-boundary. Therefore, different values from 0.55 to 0.1 Ns/m have been tried as input parameters of an error trial-corrector SPH modelling to determine this coefficient in 3D simulation, by comparing the flow time of the V-funnel model with reported data in the literature. The value of 0.2 Ns/m has provided a reasonable agreement, and it was utilised as the dynamic coefficient for two 3D simulations in this chapter.

4.4.2 U-box test

The U-box is an essential device to quantify the self-consolidating characteristic of fresh SC-ECC and to verify its ability to pass the steel rebars. The device consists of two separated chambers divided by a partition and a gate at the middle. Three reinforcing bars, with a net spacing of 3.0 cm, are placed at the gate's position performing as obstacles. The test is simulated by filling one of the chambers with fresh SC-ECC particles and then allowing material particles to flow through the adjacent chamber after passing bar-obstacles under its gravitational force. A self-consolidating index, L, is computed based on the height reached by materials in the initial empty-chamber when the flow stops levelling as $L=2H/H_0$. A total number of 83,348 particles are involved in this simulation, including 19,476 repulsive boundary particles, 64,800 and 9,072 particles represent for mortar and 1,296 fibres, respectively.

The numerical modelling results of U-box test at four time steps are plotted in three dimensions as shown in Figure 4.8. For facile observation, two front wall-boundaries of U-box are invisible. Initially, the mortar and fibre particles gradually pass three steel bars and move to the next chamber of the U-box, as can be observed in Figure 4.8a. Then, the mortar and fibre particles slowly increase their height under the action of pressure P with the restraint of the gravitational force, boundary friction and its viscosity (Figure 4.8b and Figure 4.8c). Finally, after 8.4 s since the simulation starts, the SC-ECC flow has stopped levelling as those forces are balanced. The flow reaches a value of H = 12.9 cm. This result is quite analogous to the result of the experimental study in (Kong et al. 2003a), as illustrated in Figure 4.9. The L index reflecting the self-levelling ability of SC-ECC in the simulation is also in the suggested range of SCC, from 0.73 to 1 (Nagamoto & Ozawa 1997) (Table 4.2). It should be noticed that the computation is established to run until 12.5s to ensure the actual stopping of the flow. Moreover, the kinematic coefficient accounting the friction of mix and steel bars is chosen to be equal to the mix and boundary in this model.

Table 4.2 Comparison of the flow of SC-ECC (PVA) in the simulations with experimental test data in literature.

Test	Experimental data			Simulation result
	SC-ECC (PVA)	SC-ECC (PE)	SCC	SC-ECC (PVA)
V-funnel test (R)	0.83-1.1 (Mohammed et al. 2017)	0.8 (Kong et al. 2003b)	0.8-1.2 (Ozawa 1995)	0.89
U-box vessel test (L)	0.82 (Kong et al. 2003a) ; 0.94 (Li 2002)	0.78 (Kong et al. 2003b)	0.73-1.0 (Nagamoto & Ozawa 1997)	0.86

(a) t = 0.40 s

(b) t = 1.20 s

(c) t = 5.60 s

(d) t = 8.40 s
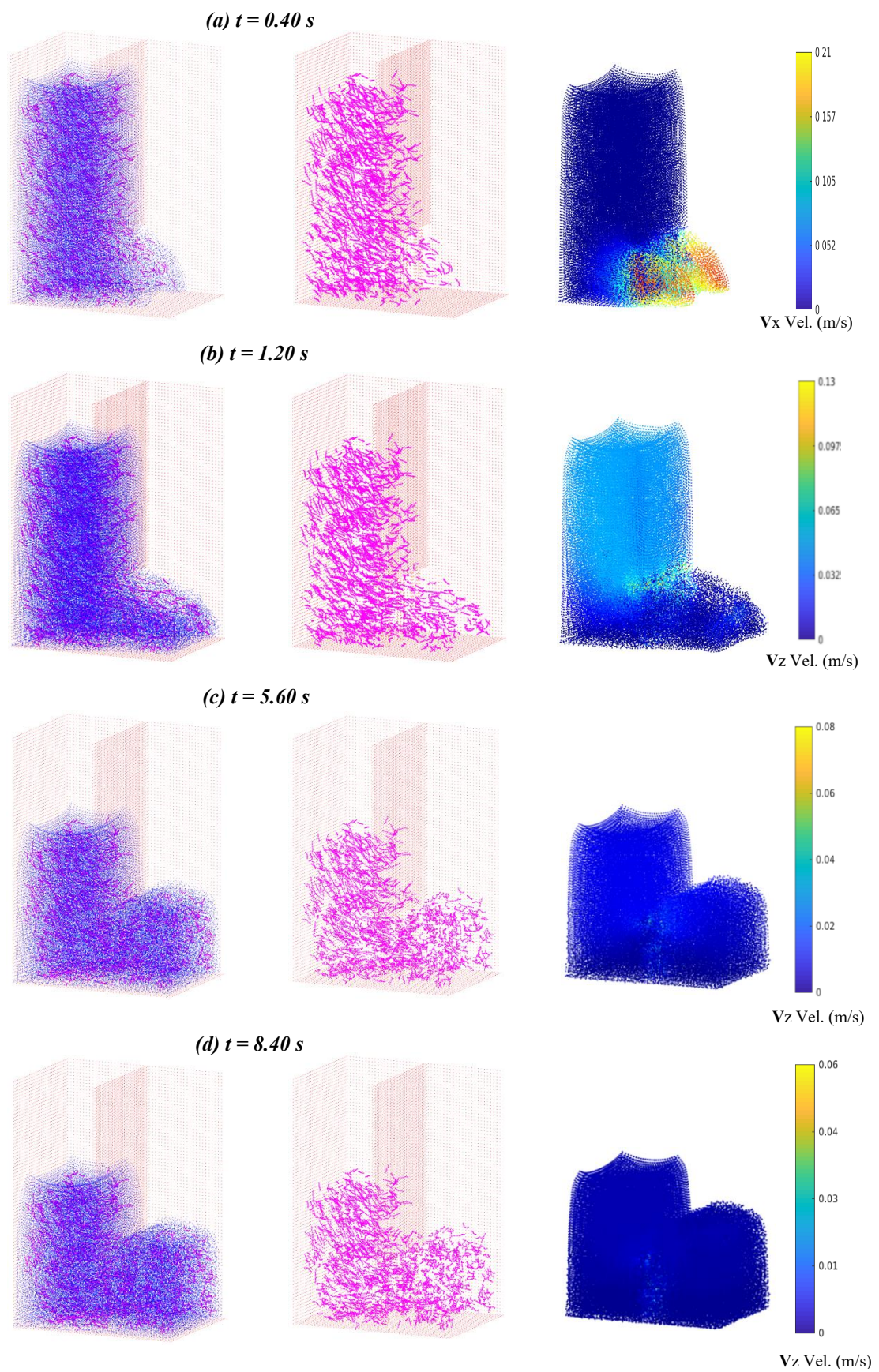
Figure 4.8   Numerical simulation results of the U-box test at different time steps.
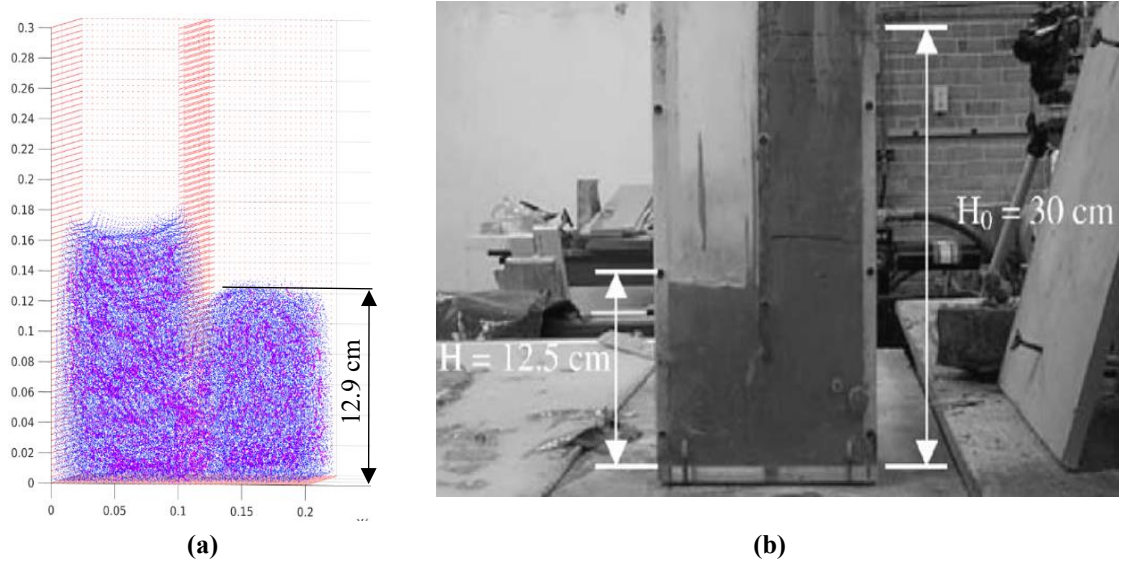
Figure 4.9   Demonstration of the self-consolidation of SC-ECC: (a) Simulation result in this study; (b) Experimental result in (Kong et al. 2003a)

4.5 Influence of Steel Reinforcement on the Flow of SC-ECC and Fibre Distribution

To explore the influence of steel reinforcement on the flow of SC-ECC, another U-box modelling without the three steel bar obstacles is performed. As compared with the original test, there is a remarkable difference in the reached height of the material particles and the magnitude of horizontal velocity after one second (Figure 4.10). In this model, it only takes 4.12 s for the SC-ECC flow to reach the maximum height in comparison with 8.4 s of the ordinary U-box test.

t = 1.00 s
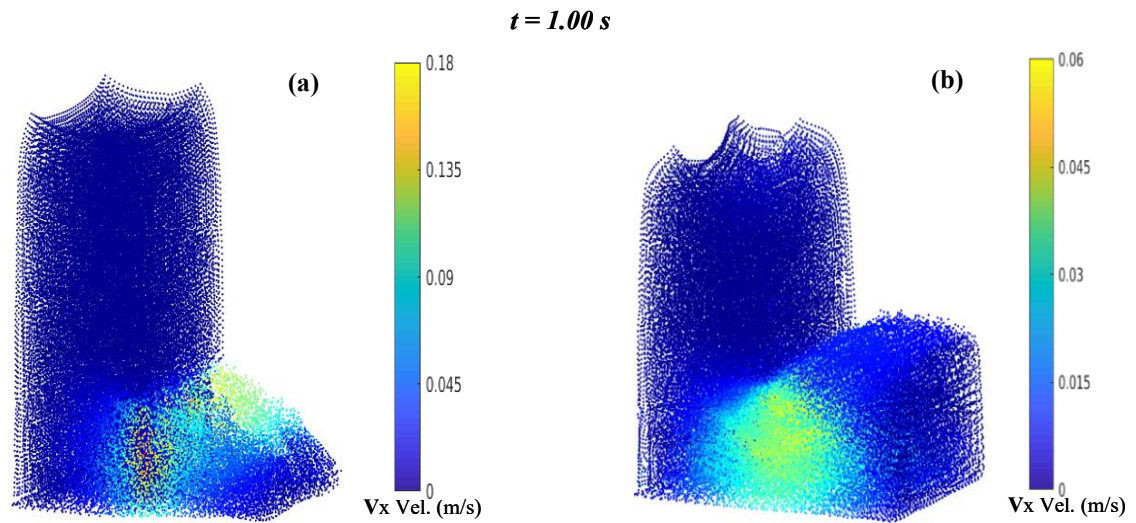
Figure 4.10   Comparison of magnitude of horizontal velocity at 1.0 second: (a) ordinary U-box; (b) U-box without steel bars.

As can be seen in Figure 4.11a, due to the presence of steel bars, a number of fibres are stuck at this position and can not travel to the next chamber. This phenomenon is the reason for the significantly decreasing of fibres in the adjacent empty-chamber in comparison with the modified U-box model (Figure 4.11b). It can also be observed that the fibre dispersion in the original U-box is also poorer than the modified one. Furthermore, flexible synthetic fibres also tend to coil more after passing the steel bars. These features might negatively affect the dispersion and orientation coefficient of flexible synthetic fibres in steel-reinforced structural elements, which then lessen the capability of ECC materials in bearing cracks in steel-ECC structures. Hence, these characteristics should be further investigated and taken into account in industrial construction of steel-ECC.
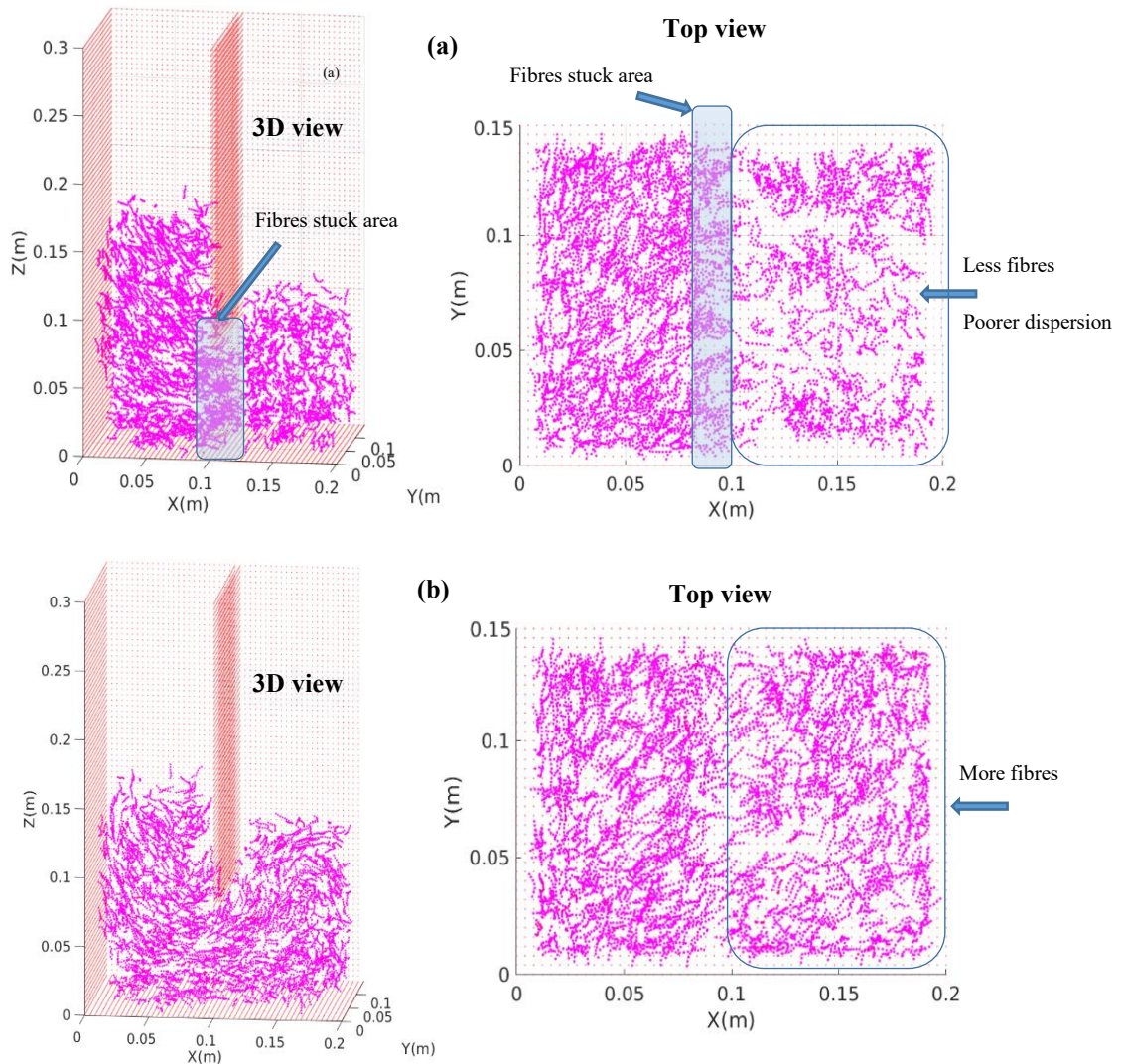
Figure 4.11   Fibre distribution in: (a) ordinary U-box; (b) U-box without steel bars.

4.6 Correlation between Plastic Viscosity, Flow Rate and Fibre Dispersion of SC-ECC

As the flow rate index, R, basically reflects the viscosity of fresh mixture (Li, Kong, et al. 1998; Okamura & Ouchi 2003), it is essential to investigate the influence of viscosity on the flow rate of SC-ECC. For a large range of the plastic viscosity of SCC mixes, the reported yield stress is almost unchanged (Ghanbari & Karihaloo 2009). Due to the similar intrinsic of SCC and SC-ECC, it is reasonable to vary the viscosity of fresh

SC-ECC while keeping the yield stress constant. Therefore, a range value of plastic viscosity μ_B from 5 Pa.s to 25.0 Pa.s corresponding to $\tau_B = 165\ Pa$ has been implemented as input parameters for V-funnel model to study the relationship between the plastic viscosity with the flow rate and fibre dispersion of SC-ECC.

The results of these simulations are shown in Figure 4.12. It can be seen that there is a strong correlation between the flow rate of fresh SC-ECC mixtures with their viscosity. However, while the completed vacation times of material particles increase with the rising of the plastic viscosity, the magnitude of their vertical velocities fluctuate. Specifically, it takes 10.56 s with v_{zmax} = 1.36 m/s for the SC-ECC mix with μ_B = 5.5 Pa. s to completely vacate the funnel in comparison with 11.56 s and v_{zmax} = 1.31 m/s of the μ_B = 25 Pa. s mix. Moreover, the maximum of vertical velocities of the mixtures with μ_B = 15 Pa. s and 17 Pa. s is much higher than the remaining mix. These features apparently affect the casting or printing speed of SC-ECC in industrial construction and the distribution/orientation of fibres in the mix.

As can be observed in the container box, the dispersion/orientation of synthetic fibres is dissimilar despite the similarly in initial random dispersion and initial inclined angle of fibres. The fibres of the μ_B = 15 Pa. s and 25 Pa.s mixtures somewhat disperse well in the container box than that in the μ_B = 5.5 Pa. s mix (Figure 4.13). This observation agrees well with those findings in (Yang et al. 2009; Li & Li 2013), suggesting that an optimal range of plastic viscosity of fresh mixes would enhance the fibre dispersion in ECC. Yang et al. (Yang et al. 2009) suggested that high plastic viscosity of fresh mixes is beneficial for better dispersion of fibres. Since the fibre dispersion is recognised as one of the main factors, which has crucial influence on the

performance of ECC, an appropriate range of plastic viscosity thus should be applied in

the practical application of SC-ECC.
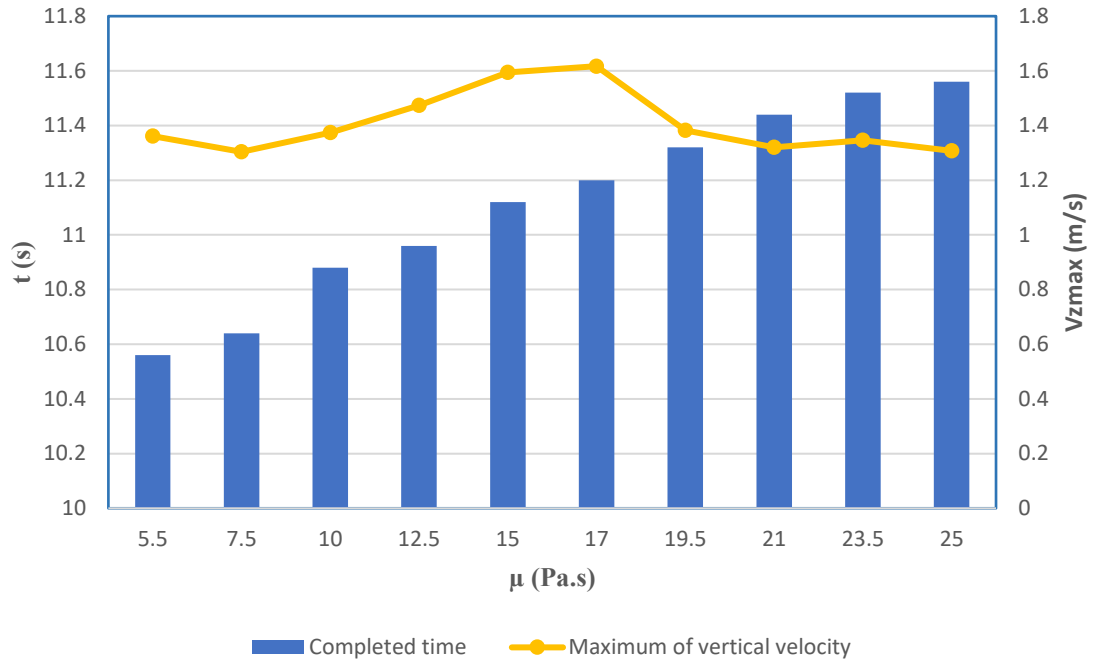
Figure 4.12   Correlation between the viscosity and the flow rate of SC-ECC.

(a) μ = 5.5 Pa.s   **(b) μ = 15 Pa.s**   **(c) μ = 23.5**
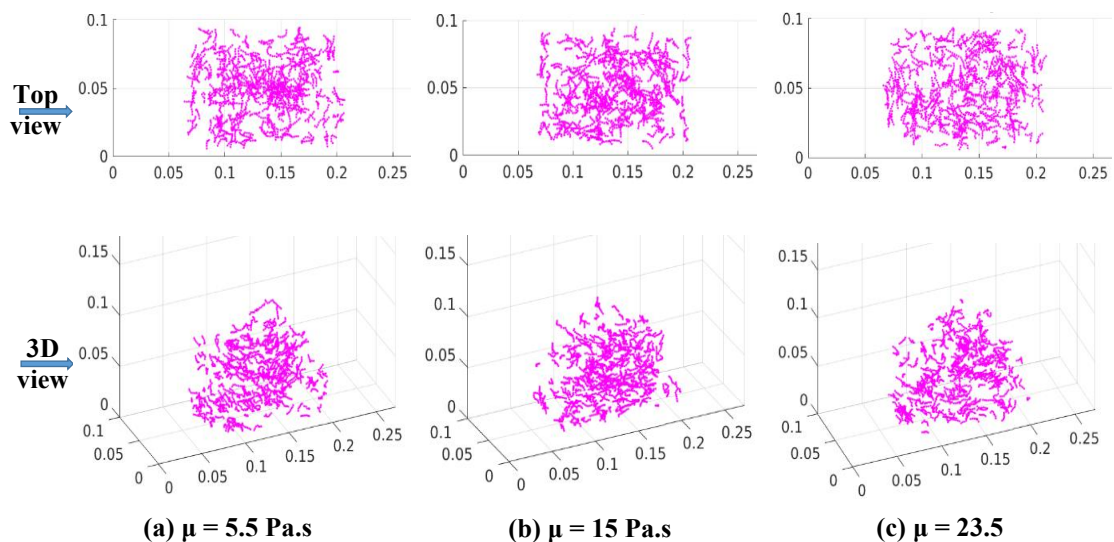
Figure 4.13   The dispersion of fibres in container box with three values of viscosity

at t = 12.5 s after completing vacate the V-funnel.

4.7 Conclusions

The V-funnel test and U-box test, which are essential to evaluate the filling and passing abilities for SC-ECC materials, are successfully simulated with a 3D numerical model in this chapter. The constitutive Cross model is used to describe the rheological behaviour of the fresh SC-ECC, which is represented by separated mortar and fibre particles and treated as weakly compressible flow in SPH approach. Flexible synthetic fibres travel smoothly with the mortar particles during the flow of SC-ECC. The rational agreements of the experimental data with the simulation results demonstrate the accurateness and effectiveness of the numerical method in 3D modelling. The proposed model provides insight into the SC-ECC's flow characteristics and the real image of flexible synthetic fibres in the mixture. This model thus not only proves the capability to substitute the repeated tests in the laboratory but also can be used to optimise the dispersion and orientation of synthetic fibre in structural members by controlling the rheology parameters and the casting technique of SC-ECC.

The results of the V-funnel model further demonstrate the correlation between the dispersion of synthetic fibres with the rheology of fresh mixtures. For the same yield stress, fibres disperse well in the higher plastic viscosity mixture than the lower one. Hence, this model has potential to be implemented to determine an optimal range of fresh mix plastic viscosity, improving fibre dispersion in structural elements. Furthermore, this model can also be extended to estimate the processing time in moulding or printing of extrudable ECC through a rectangular hopper. In addition, the presence of steel reinforcement significantly affects the flow of fresh SC-ECC. While the passing ability of SC-ECC is demonstrated, the speed of flow is reduced. Moreover,

the poorer dispersion of fibres in ECC matrix are observed in the adjacent chamber due

to the presence of steel bars.

Chapter 5

Effect of Specimen Thickness on Fibre

Orientation Distribution

5.1 Introduction

In ECC, the inclination angle of distributed synthetic fibres in cementitious matrix is recognised as playing an important role in bearing stress and bridging micro-cracks (Kanakubo et al. 2016). The larger inclined fibre, unlike the smaller one, tends to prematurely rupture due to the snubbing effect and reduction of its apparent strength (Kanda & Li 1998). This intrinsic nature of synthetic fibres raises a concern of how the size of specimens affects the synthetic fibres' orientation in ECC, which influences the mechanical properties of structural elements using ECC materials. However, studies concerning the effect of size of specimens on the orientation of synthetic fibres utilised in ECC are still rarely reported.

Unlike steel fibres that rigidly rotate and translate in the mixture during the mixing and moulding process, the rotation of synthetic fibres in ECC materials is more complex in nature. They are tiny in diameter (ranging around 0.012 to 0.039 mm) and flexible enough to be bent or coiled in the mix during the production process. This property could lead to a wide scatter in the dispersion of orientated synthetic fibres in the matrix, which might result in the variation of fibre orientation along specimens even when casting with the same batch and same technique. As one of the crucial factor, such variation can explain the fluctuation of mechanical properties in the experimental study by Rokugo et al. (2007). However, the effect of specimen thickness on the fibre orientation distribution is unclear. In another study, Lu & Leung (2017a) theoretical studied the influence of specimen thickness on the tensile performance of ECC by limiting the rotation of fibres at near the top and bottom surface of different thickness specimens. The results revealed that thick specimens tend to exhibit lower tensile strength and ductility than thin

specimens as a result of different fibre orientation in various thickness specimens. However, fibres were assumed to be straight and identically distributed.

In this context, numerical simulation provides an ideal tool for investigating the influence of specimen thickness on the orientation of flexible synthetic fibres utilised in ECC materials, to generate useful insights into the dispersion of fibres orientation in the ECC matrix. Recently, the authors have devised numerical models for simulating the flow of self-consolidating (SC) ECC, which were validated by the slump cone test in 2D simulation (Thanh et al. 2019), the V-funnel and U-box tests in 3D simulations (Thanh et al. 2020). The 3D developed model has provided the real image of the fresh SC-ECC and the actual distribution and orientation of synthetic fibres during and after the mix stopped flowing. In this chapter, the mouldings of fresh SC-ECC into three thicknesses are simulated by using the developed 3D model. This serves to examine the influence of specimen thickness on the orientation of synthetic fibres in SC-ECC specimens. The orientation of synthetic fibres at various sections of specimens is evaluated after fresh SC-ECC stops flowing in the formworks. The significant effect of element thickness on the orientation distribution of flexible synthetic fibres thus is subsequently revealed through this study.

5.2 Simulation of the Moulding of Fresh SC-ECC

In this chapter, the successfully developed 3D model is used to numerically investigate the influence of the beams' thickness on the orientation of synthetic PVA fibres in SC-ECC, through simulating the casting process of SC-ECC into beam specimens. The moulding of beams that are 340 mm in length with three different thicknesses, T, of 30 mm, 50 mm and 100 mm are simulated with the funnel mouth in

the same position (Figure 5.1) and the same initial distribution of orientated fibres. The results of these simulations are then used to quantify fibre orientation distribution in specimens of different thickness.
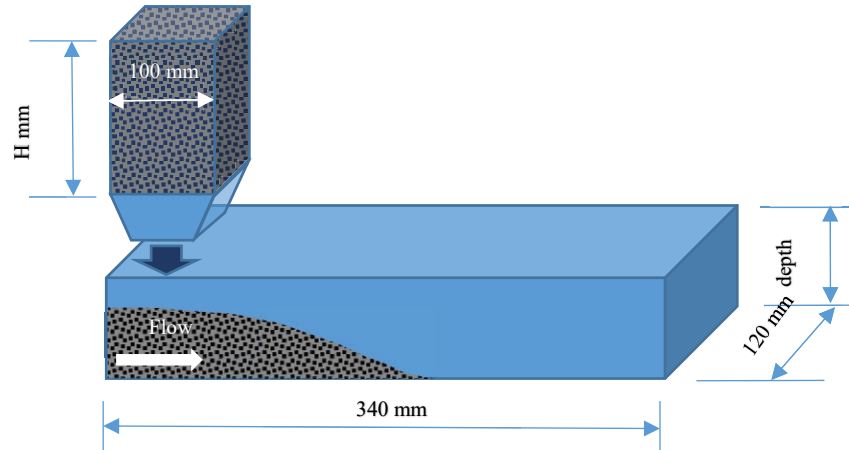
Figure 5.1   Moulding of beam specimens.

5.3 Initial Configuration

The funnel position is at the end of the beams with an identical distance from the bottom of the formwork to the bottom outlet of the funnel in three cases. Mortar and synthetic fibre particles are then created in the funnel-boxes, in which the height value, H, is calculated corresponding to three thickness beams. In all cases, synthetic fibres are created straightly with the same random distribution and orientation, reflecting that the fresh mixes in the same batch have similar dispersion of orientated synthetic fibres. Details concerning the initially created mortar and fibre particles are shown in Figure 5.2 and highlighted as follows:

- Mortar particles are initially arranged in a square grid form with the x-axis, y-axis and z-axis spacing equal to 4 mm.

- Fibre particles are generated randomly with a range of inclined angles from 0 to 90 degrees. Synthetic fibres are straight at the beginning, and the distance between the two neighbouring particles within a fibre is chosen to be equal to 2 mm.
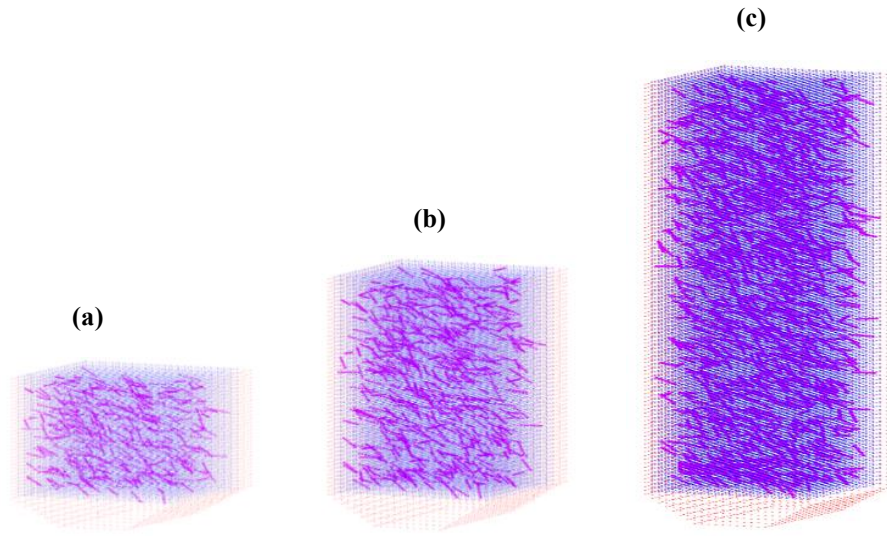
Figure 5.2   Initial mortar and synthetic fibre particles for beams thickness T: (a) T = 30 mm; (b) T = 50 mm; (c) T = 100 mm.

Table 5.1   The number of involved particles in simulations.

Beams	T = 30 mm	T = 50 mm	T = 100 mm
Boundary particles	13,260	15,318	20,512
Mortar particles	18,216	29,808	59,064
Fibre volume fraction (%)	2	2	2
Number of fibres	364	596	1,181
Fibre particles	2,548	4,172	8,267
Total particles	34,024	49,298	87,843

The number of fibres in each case is calculated based on the number of mortar particles and their 2% volume fraction. Table 5.1 shows the number of boundary, mortar and synthetic fibre particles involved in the three computations.

5.4 Results and Discussions

5.4.1 Simulation results and cutting specimens

The results of the moulding simulations of three thickness beams when material particles of fresh SC-ECC stop flowing, are shown in Figure 5.3. For facile observation of fibre orientation distribution, only fibre particles are plotted. Due to the time limitation and the bottom of the funnel mouth near the surface of T = 100 mm beam, some mortar and fibre particles still move slowly at the funnel mouth when the simulation stops after 20 s computational pre-determination time. However, this limitation does not affect the evaluation of fibre orientation in this work.
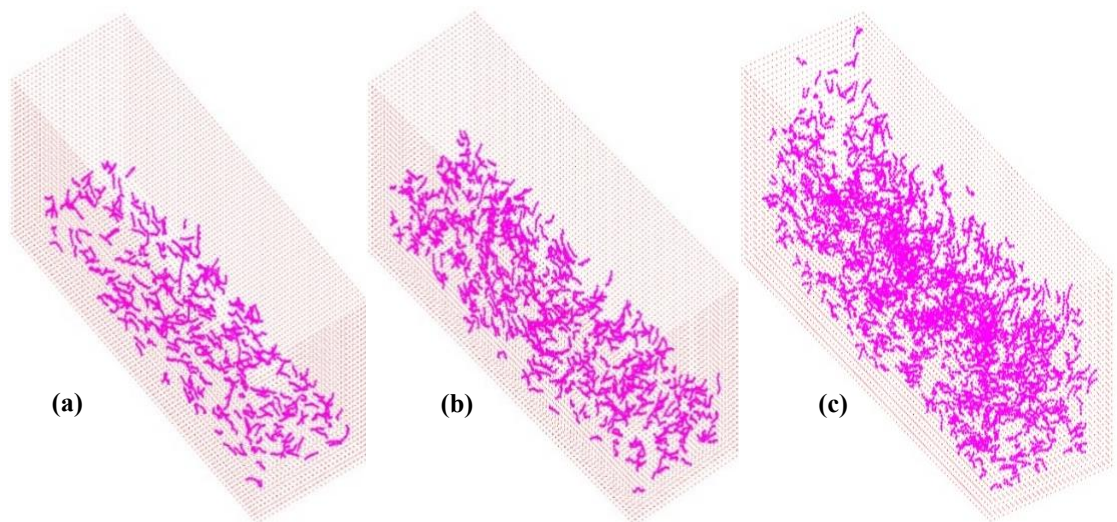
Figure 5.3   Moulding results of three thickness beams: (a) T = 30 mm; (b) T = 50 mm; (c) T = 100 mm.

Three beams are then cut virtually by multiple vertical and horizontal planes to quantify the orientation of synthetic fibres at the cutting sections (Figure 5.4a). Considering that a short straight line links two neighbouring fibre particles within a fibre, a PVA fibre will be represented by six continuity lines (Figure 5.4b). With the initial distance between the two nearby fibre particles equal to 2 mm in this study, the spacing of cut planes in vertical and horizontal directions are selected to be equal to 2 mm and 4 mm, respectively. For vertical planes, this value is comparable with the reported crack spacing in an experimental study of SC-ECC using PVA fibre (Kong et al. 2003a).
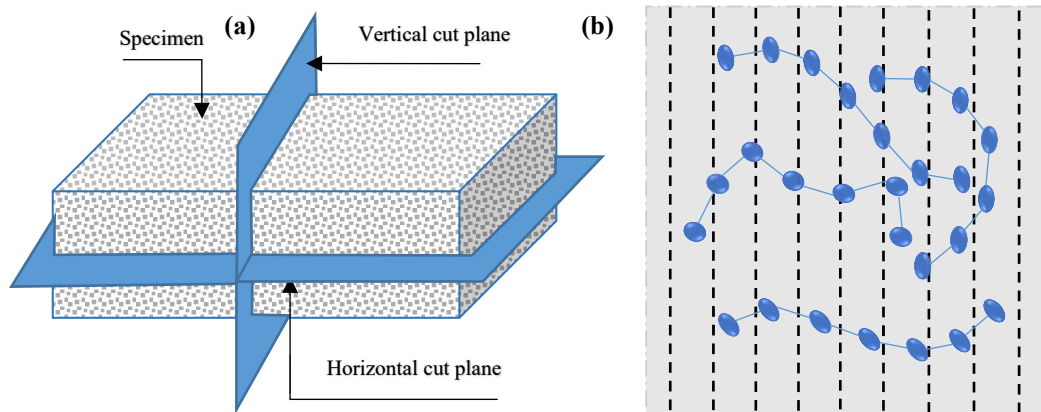
Figure 5.4 (a) Vertical and horizontal cutting planes; (b) Fibre particles intersection at multiple cutting planes.

5.4.2 Fibre orientation factor

The inclined angle of a synthetic fibre j at a vertical section is determined by the cosine of the angle α_j between two adjacent fibre particles of a fibre with the normal of the vertical plane (x-axis for vertical plane yz). The fibre orientation factor, $\overline{\theta_i}$ at plane i, is the mean value of the cosine angle of n intersected fibres at that plane (Equation 5.1). It is cleared that only two neighbouring fibre particles on opposite sides of a vertical cut plane are accounted for the orientation factor of a fibre at that plane.

$$\overline{\theta_i} = \frac{1}{n} \sum_{j=1}^{n} \cos\alpha_j \tag{5.1}$$

As can be seen from Figure 5.5, the fibre orientation factors vary along the specimens. The thin specimen tends to have a higher fibre orientation factor than the thick specimen. This finding reveals that synthetic fibres in the matrix of the thin specimen tend to be parallel more with the longitudinal direction than in the thick specimen.
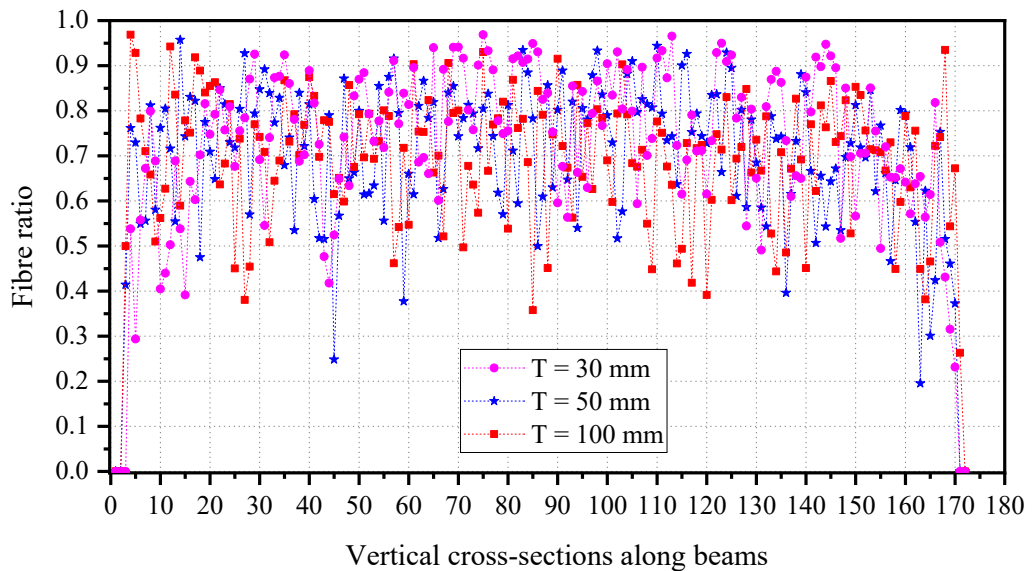
Figure 5.5 Distribution of fibre orientation factor along three beams of different thickness.

5.4.3 Fibre ratio along depths of specimen

To clarify the influence of bottom formwork and free surface of a specimen on the orientation distribution of synthetic fibres in the SC-ECC matrix, a fibre ratio along the depths of a specimen is proposed in this work. It is defined as the ratio of the number of fibre particles located between two adjacent cut planes in the horizontal direction with the total amount of fibre particles. It is clear that if fibres tend to be parallel with the

bottom or free surface of a specimen, the number of counted fibre particles in these areas would be larger than that of other parts of this specimen.

As shown in Figure 5.6, the bottom of formwork significantly affects the orientation of synthetic fibres, resulting in a tendency of these fibres to align along the longitudinal direction of specimens in this area. Consequently, the ratio of fibres in this area is remarkably larger than in other regions of the specimens. Additionally, this influence is more noticeable in thin specimens when compared with the thick specimens. Meanwhile, synthetic fibres tend to rotate freely at the top surface of specimens.
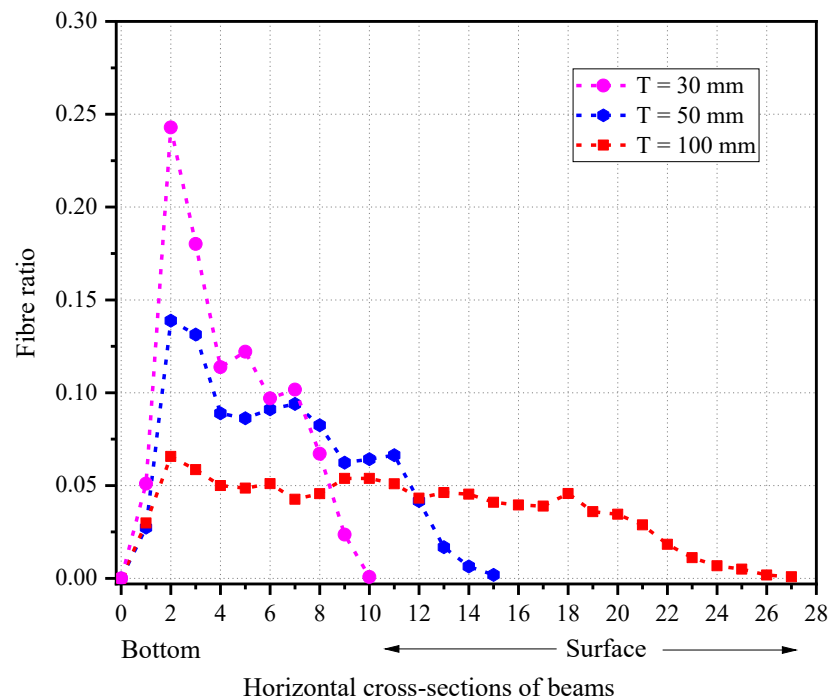
Figure 5.6   Fibre ratio along depths of three different thickness beams.

5.5 Conclusions

The mouldings of fresh SC-ECC in the formworks of three beams of different thickness are simulated using the developed 3D SPH model. Synthetic fibres in three

funnels are straightly generated with identical random distribution and orientation at the initial stage. From analysing the orientation of flexible synthetic fibres in simulated specimens, the following conclusions can be drawn:

- The orientation factors of synthetic fibres in SC-ECC vary along beam specimens.

- Thin specimens tend to have higher fibre orientation factors than thick specimens.

- The orientation of synthetic fibres is remarkably affected by the bottom of the formwork. Synthetic fibres are likely to be parallel with the longitudinal direction of specimens in this region.

- Synthetic fibres tend to rotate freely at the top surface of specimens.

The above findings regarding fibres orientation distributions might partially explain the greater tensile strength and strain capacity in thin specimens than those obtained from thick specimens which were reported in several studies. However, the distribution of fibres is also a crucial factor that influences the tensile behaviour of ECC and needs to be considered. Thus, it is essential to clarify the distinct effects of fibre orientation and distribution on the tensile behaviour of ECC. Moreover, the bending of synthetic fibres, which might affect their orientation distributions, has not been studied previously. These issues are subsequently addressed in the next chapter.

Chapter 6

Fibre Orientation and Distribution and Their Effects on Tensile Performance of ECC

6.1 Introduction

Fibres bridging micro-cracks, bearing and transferring stress to the surrounding matrix in the fracture zone play the crucial role in converting the brittle behaviour of ordinary concrete to the quasi-brittle behaviour of fibre reinforced composites, and to the ductile behaviour of high-performance fibre reinforced cementitious composites (HPFRCC) (Zollo 1997; Brandt 2008). Engineered Cementitious Composites (ECC) is a unique class of HPFRCC exhibiting high tensile ductility with a strain capacity that can reach 5%. To obtain the unique tensile performance of ECC, micromechanical models served as a useful tool for tailoring microstructures and optimising constitutive materials. Two indispensable criteria to form multiple cracks under tension, i.e., controlling the initiation of cracks (strength criterion) and ensuring the appearance of steady-state flat-crack propagation (energy criterion) are attained with just around 2% volume fraction of synthetic fibres (Li 2003).

From the micro to macroscale considerations, the distribution and orientation of fibres are recognised as the two vital factors which govern the relationship between the tensile stress-crack opening of a single crack, and thus strongly affect the tensile stress-strain behaviour of ECC. At the microscale level, the inclination angle of distributed fibres in the cementitious matrix is a crucial factor which governs the mechanisms of the fibre-matrix interface (Li et al. 1990; Ouyang et al. 1994). The snubbing phenomenon associated with inclined fibres helps to enhance fibre-bridging stress (Leung & Ybanez 1997). However, the apparent strength of inclined fibres is reduced due to fibres being bent when pulled out from the matrix (Kanda & Li 1998). Thus, a large inclined fibre tends to prematurely rupture more than a smaller one due to the combination of the snubbing effect and the reduction of its apparent strength. Moreover,

fibres' inclination also reduces the presence of fibres to bridge cracks at the mesoscale level when compared with aligned fibres. This situation significantly compromises the efficiency of fibres in ECC (Tosun-Felekoğlu et al. 2014). In the laboratory, by improving the distribution of fibre in the fresh mix of ECC through adjusting the mixing sequences (Zhou et al. 2012) or rheology control of fresh mortar (Li & Li 2013), the improved performance of tensile strength and tensile strain capacity was attained at the macroscale structure. Also, the variation of fibre distribution might cause a fluctuation of peak tensile stress at different sections of ECC specimen (Lu & Leung 2017b). Ideally, when fibres are homogeneously distributed in the cementitious matrix, the scatter of the peak fibre-bridging stress may be reduced, and consistent tensile behaviour of ECC specimen might be achieved.

Being recognised as crucial factors, methods for identifying fibre orientation/distribution factors in the ECC matrix have been well developed (Lee et al. 2009; Tosun-Felekoğlu et al. 2014; Felekoğlu et al. 2015; Ding et al. 2020). For detecting synthetic fibres with a tiny diameter and owning a lower contrast than the cementitious matrix, the fluorescence technique (Lee et al. 2009) and the backscatter mode of scanning electron microscope (Felekoğlu et al. 2015) were proved to be effective. However, these techniques basically require combining the image processing and analysis procedures, which is a time-consuming process. Thus, the overwhelmingly favoured approach is to cut the specimen and obtain the fibre orientation/distribution factors at the major cracking position or near the fracture zone of tested specimens. The obtained information was then used to correlate with the mechanical performance of ECC specimens. Visual observation and analysis of fibre orientation and distribution in

the whole specimen by using water glass solution to perform the casting of self-consolidating PVA-ECC were also conducted (Kanakubo et al. 2016).

Together with well-developed detection techniques, existing research efforts on the fibre orientation/distribution in ECC have mainly focused on: 1) improving the dispersion of fibre in the fresh mixture as discussed above; and 2) understanding fibre orientation distribution in the specimen and its effect on the tensile behaviour. The second approach is, in general, based on the hypothetical rotation of a rigid fibre in different zones of a specimen, and categorising the distribution of fibre orientation in 2D or 3D. The ultimate tensile stress-strain relationship of ECC specimen tends to decrease if the fibre orientation distribution changes from 2D to 3D (Lu & Leung 2017a; Alberti et al. 2018a). However, synthetic fibres in ECC are flexible, i.e., they can be bent or coiled in the matrix of ECC. Notably, the orientation of a bending fibre changes at different sections of the specimen. Moreover, the actual fibre orientation distribution is also affected by some factors like casting techniques or the rheology of fresh mix. Hitherto, a reliable technique, which can provide a better understanding of the orientation and distribution of flexible synthetic fibres in the matrix of ECC, and then providing a practical data of fibre orientation/distribution factors to estimate the tensile performance of ECC specimens, has not been reported.

At the lower mesoscale, the bridging constitutive model of ECC has been developed (Lin et al. 1999) and improved (Yang et al. 2008; Huang et al. 2015) to predict the stress-crack opening (σ - δ) relationship of a single crack. Although the two-way pullout mechanism of fibre, micro-matrix spalling and Cook-Gordon effects were considered, the prediction from the developed models still shows a remarkable difference in comparison with the experimental results (Yang et al. 2008). If the

incorrectness of input parameters of material microstructure is negligible, the inaccurate description of the stress-displacement relationship of fibres when opening a crack could be considered as the main factor causing those difference. This is because the existing models were developed based on the stress of a perpendicular fibre displacing with a crack plane, while most of fibres are arbitrarily inclined in the real matrix of ECC. Since the σ - δ relationship crucially governs the tensile strain-hardening in the macroscale composite structure of ECC, improving the accuracy of σ - δ prediction is also essential.

In the present chapter, a novel approach is proposed to numerically investigate the distribution and orientation of fibres in ECC specimen and their influence on the tensile performance through consideration of the two states of ECC. At the fresh state, the moulding of fresh ECC into the mould is simulated. The 3D SPH model, which was successfully developed above is adopted to simulate the flow of material particles during the moulding process. The information of fibre orientation/distribution at different sections of the specimen is then acquired when fresh ECC completes flowing in the formwork. At the hardened state, a fibre-bridging model is newly developed based on the two-way pullout mechanisms of an arbitrarily inclined fibre, and it is found to fit better with experimental data than existing models in the literature. The obtained fibre orientation and distribution data will then be implemented in the developed fibre-bridging model to attain the peak bridging stress at multi-vertical sections, which imitate the multi-flat crack in an ECC specimen. The orientation/distribution of bendable synthetic fibres from moulding simulation and obtained σ - δ curves at consecutive sections are then discussed. In the following sections, the SPH method for moulding simulation is briefly introduced. Then, the σ - δ relationship of a single crack with

bridging-inclined fibres is established. Finally, a benchmark example is conducted to illustrate the potential of the proposed approach.

6.2 Methodology

6.2.1 Simulation of the moulding of fresh ECC at the fresh state

As a mesh-free method, the SPH is a powerful approach for simulating the large deformation of the moulding process of a flowable ECC material owing to its self-consolidating properties. The SPH makes it possible to discretise the whole computational domain into separated particles possessing field variables, and then track the change in those properties during their motion.

The successfully developed 3D model in the Chapter 4 will be implemented to simulate the moulding process of fresh ECC. As one of the advantages of the SPH method is the ability to track the change of field variables (position of fibre particles in this study), the information of fibres orientation and distribution in the whole specimen can be identified.

6.2.2 Stress-crack opening relationship for a single crack at the hardened state

The bridging behaviour of fibres after initiating the first crack at the weakest matrix strength intensively affects the ultimate tensile strength and tensile strain capacity of ECC. This behaviour, first, governs the ability of crossing fibres to sustain the stress released from the weakest matrix, then transfer the stress into the adjacent matrix, helping to steadily form multiple flat cracks sequentially at other defect zones in the specimen.

At a crack plane, a crossing fibre typically undertakes two main mechanisms. First, it has to be completely debonded before being pulled out of the matrix. During the displacement of fibre in these two mechanisms, the debonding fracture energy, G_d, and frictional bond strength, τ_0, are assumed to be constant (Yang et al. 2008). For a single fibre parallel to the loading direction, loads of fibre in the debonding stage P_d and then the pullout stage P_p relevant to its displacement δ_m in the cementitious matrix are calculated as

$$P_d = \pi \sqrt{(\tau_0 \delta_m + G_d) E_f d_f^3 (1 + V_f E_f / V_m E_m)/2} \qquad \text{when} \ \ \delta_m < \delta_0 \qquad (6.1)$$

$$P_p = \pi \tau_0 (L_E - \delta_m + \delta_0)(d_f + \beta(\delta_m - \delta_0)) \qquad \text{when} \ \ \delta_0 < \delta_m < L_e \qquad (6.2)$$

In Equations. 6.1 and 6.2, E_m, E_f are the elastic modulus of matrix and fibres; V_m, V_f are the volume fraction of matrix and fibres. The value $\delta_0 = 2\tau_0 L_e^2 (1 + V_f E_f / V_m E_m)/(E_f d_f)$ is the displacement of a fibre when being fully debonded from the surrounding matrix, and d_f is the fibre diameter. The slip-hardening coefficient β represents for the resistance of synthetic fibres at fibre/matrix interface during the pullout process.

For PVA fibre exhibiting tough slip-hardening behaviour, the pullout load of the short embedment side of a fibre can be higher than the debonding load in the long embedment side and, therefore, leading to fibre into the pullout stage at both sides of the crack (Yang et al. 2008). In the numerical approach, the short embedment length L_{Se} and the long embedment length $L_{Le} = L_f - L_{Se}$ of fibre on each side of a potential crack can be identified initially. The displacement of fibre when being completely debonded from the surround matrix $\delta_{0S\,(0L)}$ is then computed by Equation 6.3:

$$\delta_{0S\,(0L)}=2\tau_0 L^2_{Se(Le)}(1+\eta)/(E_f d_f) \tag{6.3}$$
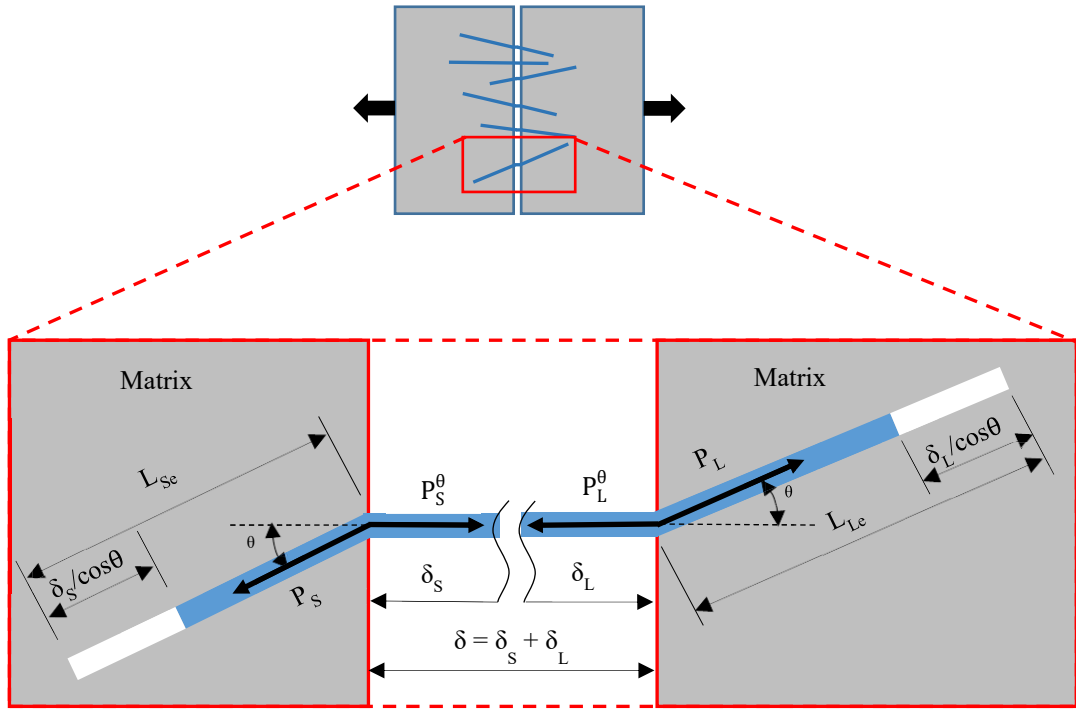
Figure 6.1   Schematic diagram of an inclined fibre θ bridging at both sides of a crack δ.

Considering a single fibre owning an incline angle θ with the loading axis, if the contribution to a crack opening δ from short and long embedment side denotes as δ_s and δ_l (Figure 6.1), the corresponding displacements of fibre in the matrix equal $\delta_s/\cos\theta$ and $\delta_l/\cos\theta$, respectively. With respect to the angle θ, the bridging force of an inclined fibre from the short and long embedment length can be generally expressed as

$$P_S^\theta=P_L^\theta=\begin{cases} P_d e^{f\theta}\cos\theta, & \text{for } \delta_{S(L)}/\cos\theta \leq \delta_{0S(0L)} \\ P_p e^{f\theta}\cos\theta, & \text{for } \delta_{0S(0L)} < \delta_{S(L)}/\cos\theta \leq L_{Se(Le)} \end{cases} \tag{6.4}$$

where $e^{f\theta}$ accounts for the snubbing effect, which is considered when an inclined fibre is pulled out from the matrix, and f is the snubbing coefficient. This effect magnifies the bridging load of an inclined fibre, while the apparent strength of that fibre is reduced due to the fibre being bent when dragged out from the matrix (Kanda & Li 1998).

Depending on micromechanical parameters, embedment lengths and the inclination angle θ, the embedded fibre at two sides of a crack can experience three stages when the crack appears and opens as follows:

- Stage 1: Two-way debonding: this occurs when the displacement of fibre on both sides of the crack is similar, meaning that $\delta = 2\delta_S = 2\delta_L$, and satisfying the condition $\delta_S/\cos\theta = \delta_L/\cos\theta \leq \delta_{0S}$

- Stage 2: Pullout – debonding: when the stress causes the displacement in the short side $\delta_S/\cos\theta > \delta_{0S}$, short embedment of fibre is completely debonded and starts to be pulled out from the matrix. Meanwhile, the long embedment side is still in the debonding phase with the displacement $\delta_L/\cos\theta \leq \delta_{0L}$.

- Stage 3: Two-way pullout: the effect of slip-hardening in short embedment side during pullout leads the long embedment side of fibre into the pullout stage simultaneously, and the corresponding displacement $\delta_L/\cos\theta > \delta_{0L}$.

Based on the condition of fibre displacements and related stress in the three stages above, the relationship of stress-crack opening (σ - δ) of fibre-bridging crack is then established. Excluding stage 1 when $\delta_S = \delta_L$, the iterative computations are applied in stages 2 and 3, on the principle of force balancing of the fibre at both sides of the crack, to identify the δ_S, δ_L separately. In this work, the elastic stretch of fibre is neglected. The $\sigma(\delta)$ is obtained through numerical grouping fibres based on their short embedment lengths L_{Se} from 0 to $L_f/2$ and inclined angles from 0° to 90°, then taking the average value of the bridging force of all groups.

For comparison and verification purposes, a similarity of matrix and PVA fibre parameters as used in Yang et al. (2008) is adopted and shown in Table 6.1. The interface parameters between a single pullout fibre and surrounding matrix, influenced by the

density of fibre in the matrix, are summarised in Table 6.2. The experimental results from measuring the $\sigma(\delta)$ curves of single cracks of ECC with 0.1% and 0.5% volume fraction of PVA fibre in Yang et al. (2008) are also collected. As can be seen in Figure 6.2a and Figure 6.2b, the results of $\sigma(\delta)$ relationship of the current model fit well with the experimental data. In comparison with the model prediction of Yang et al. (2008) and Huang et al. (2015), which are also plotted in Figure 6.2, the current results show a better prediction of $\sigma(\delta)$ during the fibre pullout stage.

Table 6.1　Matrix and PVA fibre parameters (Yang et al. 2008)

Matrix	Elastic modulus E_m (GPa)	20
Fibre	Fibre length L_f (mm)	12
	Fibre diameter (mm)	0.039
	Fibre elastic modulus E_f (GPa)	22
	Apparent tensile strength σ_{fu} (MPa)	1060
	Fibre strength reduction factor f'	0.33

Table 6.2　Interface parameters (Yang et al. 2008)

Fibre volume fraction V_f (%)	0.1%	0.5%	2%
Frictional bond strength τ_0 (MPa)	1.91	1.58	1.31
Debonding fracture energy G_d (N/m)	1.24	1.13	1.08
Snubbing coefficient f	0.20	0.20	0.20
Slip-hardening coefficient β	0.63	0.6	0.58

(a)   Crack opening (mm)

(b)   Crack opening (mm)
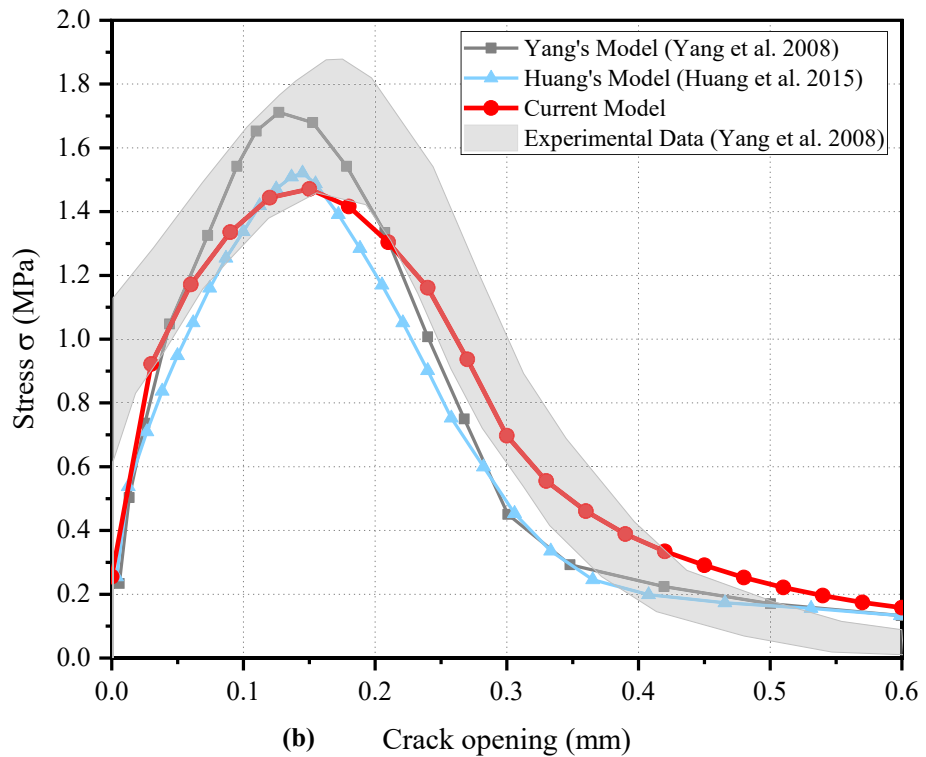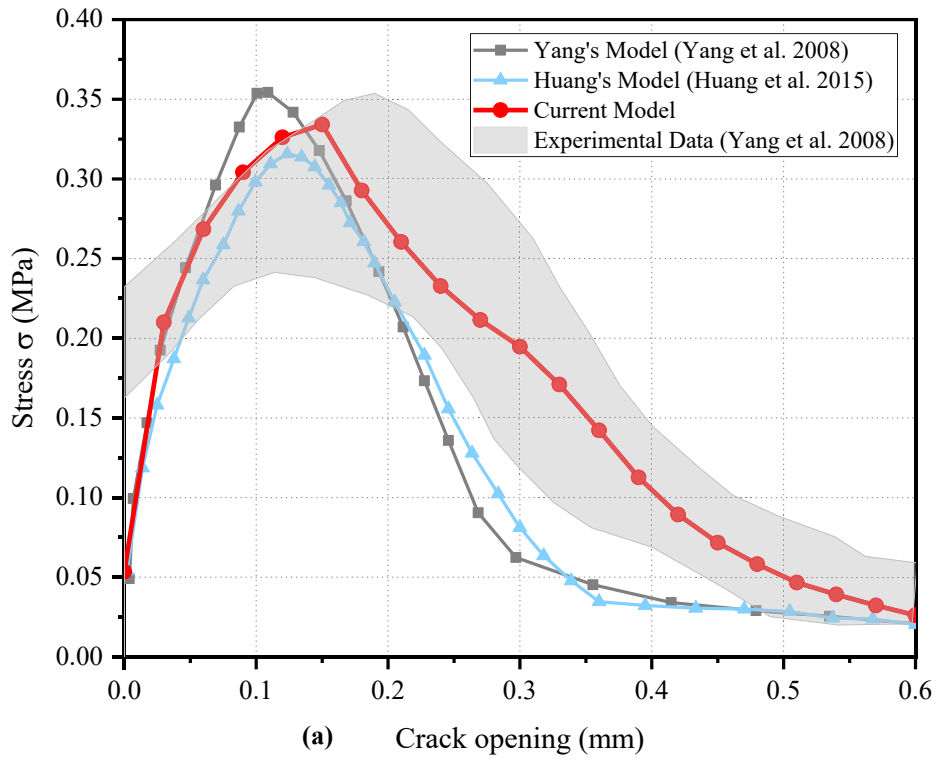
Figure 6.2 Comparison of model prediction and experimental data of $\sigma(\delta)$ curve: (a) $V_f = 0.1\%$; (b) $V_f = 0.5\%$.

Since the stress values are magnified in inclined fibres when they are dragged out of the matrix at the crack surface, their reduced apparent strength could be promptly overcome when a crack opening develops. Thus, the larger inclination of fibres has a tendency to prematurely rupture unlike the smaller inclination ones. It is clear that ruptured fibres or completely pulled out fibres will no longer contribute to the $\sigma(\delta)$ relationship. As illustrated in Figure 6.3, when five different groups of fibre inclinations with an identical distribution of 2% volume fraction of PVA fibres are considered, the ultimate tensile strength significantly increases for the group of fibres exhibiting smaller inclination. For instance, the peak stress of the group of fibres inclination from $0° - 30°$ might be almost double that of the group of $30° - 90°$ inclined fibres. The peak stress is also achieved at a larger crack opening, meaning that the strain capacity is also increased. These observations can be explained by the fact that there are less early ruptured fibres in the smaller inclination groups. These above properties emphasise the role of fibre orientation in ECC, and might be achieved in specimens produced by the 3D printing technique, since fibres are well-oriented through the nozzle of a printer (Li et al. 2020). For the group of $0 - 90°$ inclined fibres, the ultimate tensile strength is 5.3 MPa at around 0.15 mm of the crack opening. These values are also comparable with those reported in the literature (Huang et al. 2015; Lu et al. 2017).
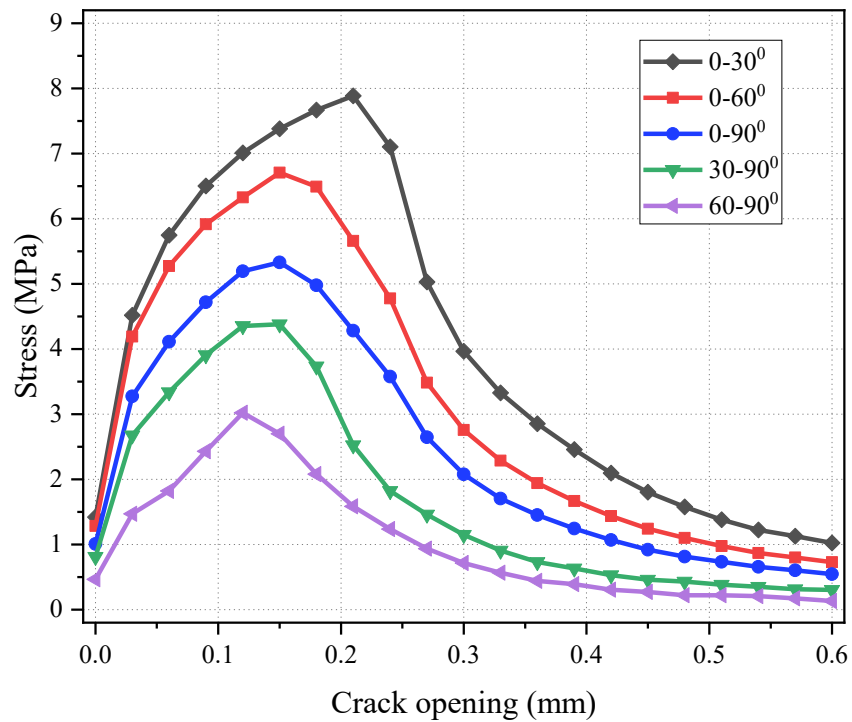
Figure 6.3   The σ(δ) relationship for a crack with different ranges of fibre inclination.

6.3 A Benchmark Example

The main objective of this research is to propose a novel method to investigate the orientation and distribution of flexible synthetic fibres inside the fresh mixture, then to examine their effects on the tensile properties at the hardened state of the ECC specimen. Thus, a benchmark example of the PVA-ECC specimen is conducted and presented in this section to illustrate the potential of this approach.

6.3.1 Moulding simulation of a beam specimen

The moulding of a beam specimen of dimensions 50×120×340 mm in depth, width and length is simulated. These dimensions are to ensure the fibre orientation distributing in a 3D scenario. The setup of initial configurations for mortar, fibre and boundary particles is displayed in Figure 6.4. A total of 29,808 mortar particles with their spatial

distances equal to 4 mm are created in the funnel. With 2% fibre volume fraction, 4,172

fibre particles are created based on the number of mortar particles. This number of fibre

particles represents 596 fibres in the mix, indicating that seven-consecutive particles

represent 12.0 mm length of a PVA fibre. The inclination of fibres is generated randomly

with a range of angles from 0° to 90°. The material and two-rheology properties are

selected as explained in Chapter 3. The selective values of the yield stress $\tau_B=165$ MPa

and the plastics viscosity $\mu_B=17$ Pa.s were authenticated through the results of the

standard tests of slump flow tests, V-funnel and U-box tests.
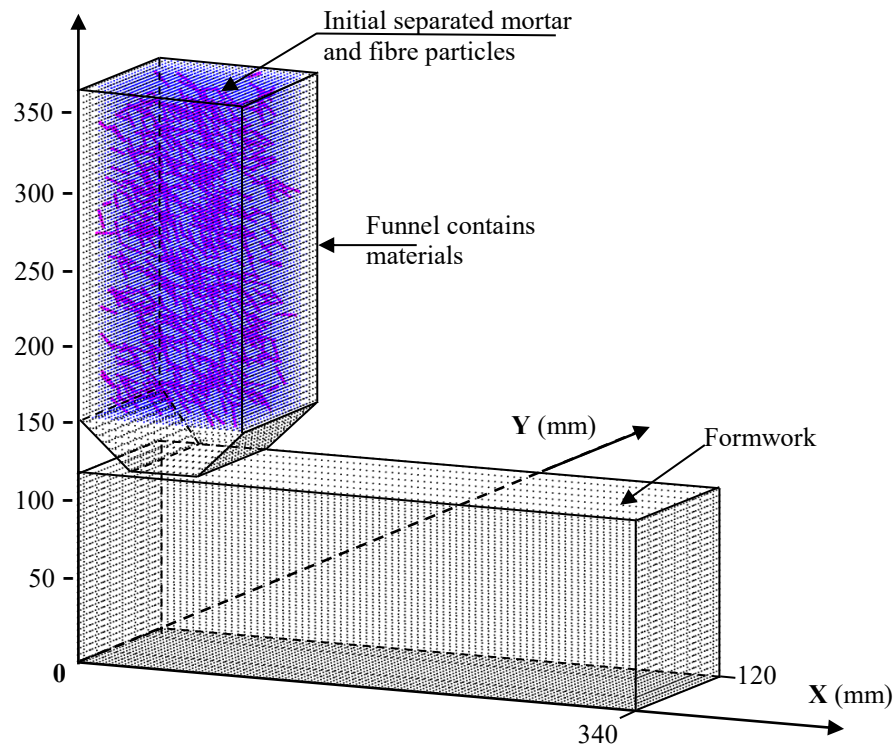
Figure 6.4   Initial configuration of contained funnel, fibre and mortar particles, and formwork
of specimen for moulding.

The flow patterns at several time steps obtained from the numerical simulation are

shown in Figure 6.5. During the moulding process, mortar and fibre particles drop

through the bottom outlet of the funnel to the bottom of the beam at the funnel position,

then flow to the far end of the mould. After 4.0s, material particles gradually stop flowing, of which only some particles under the funnel still slowly move when the computation is stopped.

At 0.40 s

At 2.00 s

At 8.00 s

At 4.00 s
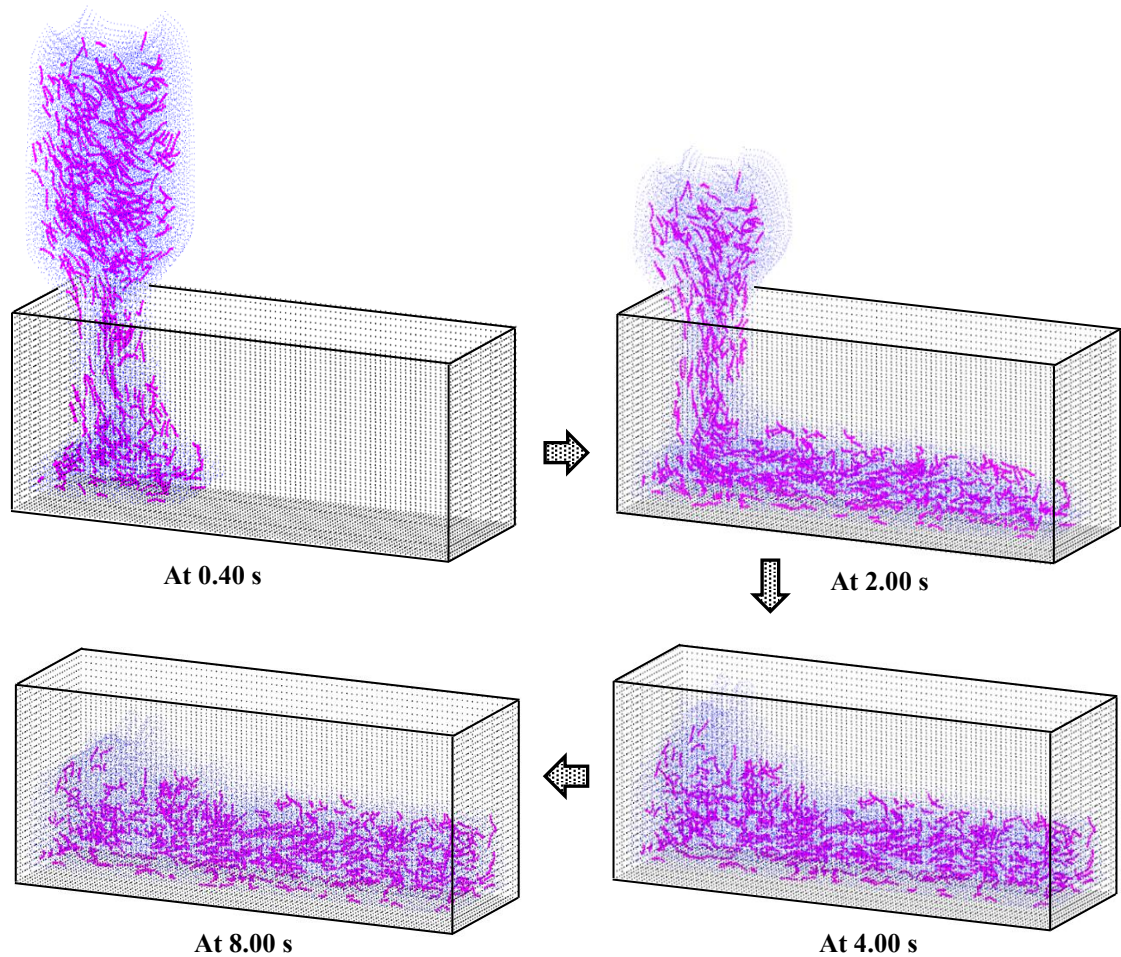
Figure 6.5   Flow patterns of mortar and fibre particles at four time steps during the moulding process.

For a bending fibre, its inclination can change along different sections of the specimen. Moreover, fibre bending also reduce the amount of fibre at fracture planes when compared with aligned fibres, thus undermining the fibre's efficiency in bearing cracks. Alberti et al. (2017) have probabilistically proposed a reductive factor for the length of bendable synthetic fibres equal to 0.946 initially, and then validated it to 0.856.

From the simulated result documented in this study, the bending of a flexible synthetic fibre can be estimated by taking the sum of spatial distance between two nearby particles of that fibre, then divide to its original length. Then, the general bending trend of all flexible synthetic fibres during their flow can be obtained. As illustrated in Figure 6.6, the normalised length of fibres significantly change from the start to around 4.0s. After that time, fibres' shape tends to become stable, and also reveal a slight tendency to reverse back to their straight line. The value of bending ratio, denoted as R_f, can approximately take around 0.915. Although synthetic fibres are initially created as straight lines in the funnel, the obtained bending ratio does agree with the probabilistic value above.
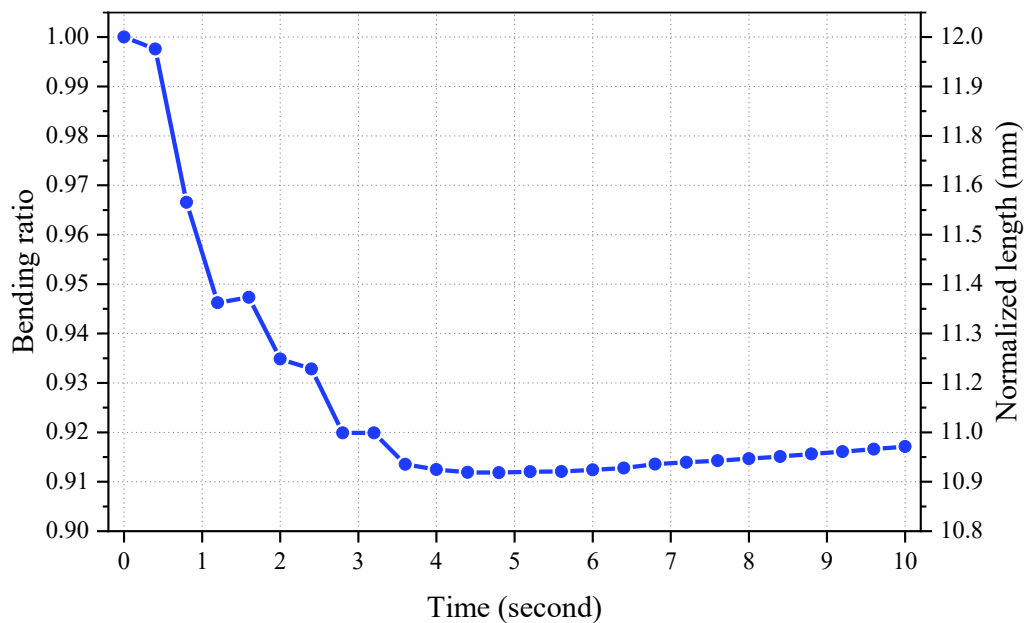
Figure 6.6   Bending of fibres at different times of flow.

6.3.2 Fibre orientation and distribution

Similar to the laboratory's works or field practices, the position of material particles are fixed when materials stop flowing, and the specimen will then be considered

for transfer into the hardened state in this work. For visual observation purposes, different 3D views of fibre orientation and distribution in the specimen are plotted in Figure 6.7. Most of the fibres are observed to be bent in the beam, as discussed above. Also, the top and front views of the orientation and distribution of fibres in the specimen are displayed in Figure 6.8. The heterogeneous distribution of fibre in the specimen can be observed. This outcome might be caused by the poor dispersion of fibres in the funnel at the beginning, which has not been considered in this current study. To quantify the orientation and distribution of fibres, the specimen is then cut by multi-vertical sections, which represent multi-flat cracks in the strain-hardening ECC. For reports of flat crack spacing of 2% PVA- ECC materials vary around 1 mm to 4 mm, the spacing between cutting sections is chosen to be equal to 2 mm in this study. This value also suits the initial distance between two nearby particles of a fibre. A total of 170 sections from end to end of the specimen is then numbered and illustrated in Figure 6.8.
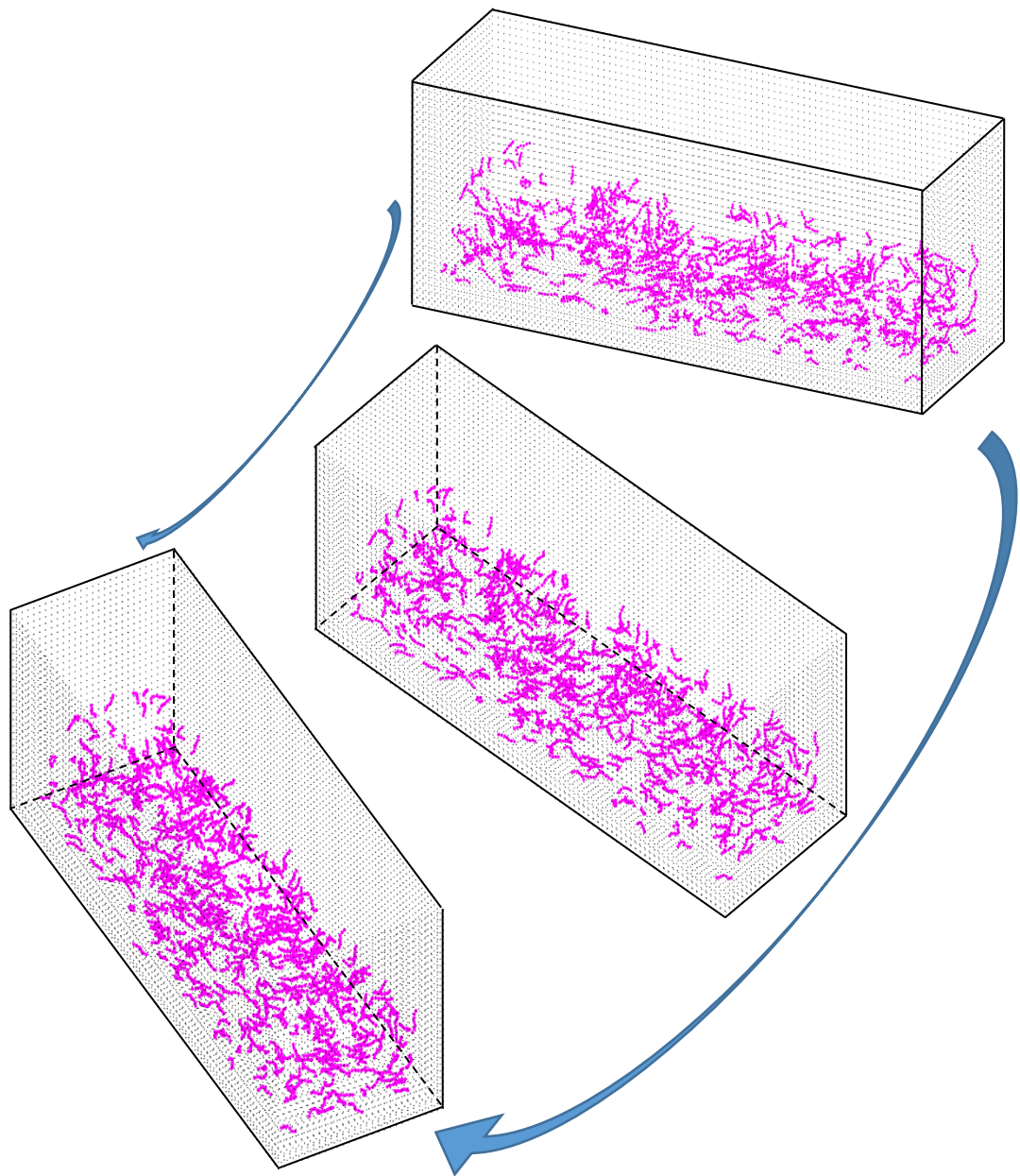
Figure 6.7 Different 3D-view of fibre orientation and distribution in the specimen after completing flow.
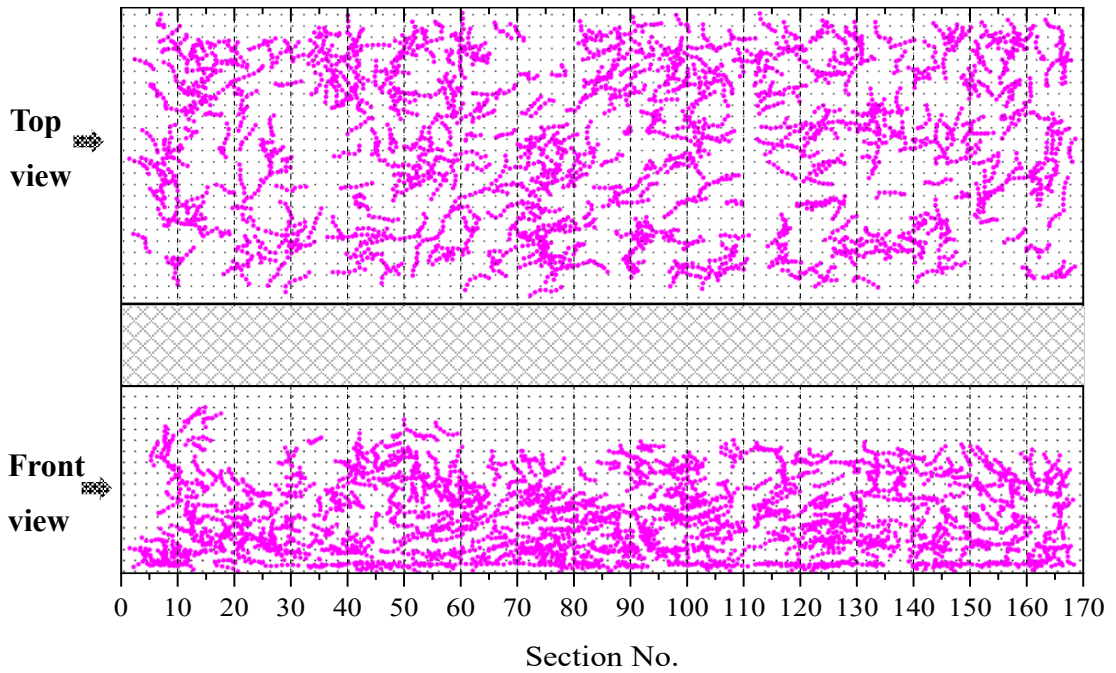
Figure 6.8 Two 2D-views of fibre orientation and distribution from the top and front of the specimen and the numbered sections.

6.3.2.1 Fibre orientation factor

For a section i (at vertical plane yz), the orientation factor of an inclined fibre is determined by the cosine of the angle between its two adjacent particles j and $j+1$, but at the opposite side of that section with the loading axis (x-axis). The angle α_{ij}, in Figure 6.9 is first calculated and the fibre orientation factor at section i, θ_i, is then identified by taking the mean value of the cosine angle α_{ij} of all n intersected fibres at that section.

$$\alpha_{ij} = \tan^{-1}\left(\sqrt{\Delta y_{ij}^2 + \Delta z_{ij}^2}/\Delta x_{ij}\right) \tag{6.5}$$

$$\theta_i = \frac{1}{n}\sum_{j=1}^{n} \cos\alpha_{ij} \tag{6.6}$$
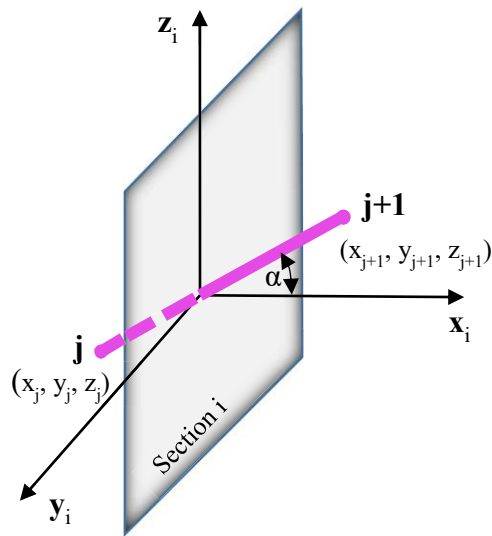
Figure 6.9 Schematic of two nearby fibre particles j and j+1 with section i.

The results of fibre orientation factors along the specimens corresponding to the 3D scenario are plotted in Figure 6.10. Due to the distortion of fibres under the funnel mouth and at the far end-wall of the specimen, only the results of sections from No. 20 to No.150 are considered. The variation of fibre orientation factors along the specimen can be observed, even with those adjacent sections. The average value of fibre orientation factor of the considered sections is somewhat larger than 0.65, and the average inclined angle θ is in the range of $30\text{-}50^0$. Those values are slightly higher than those reported in the literature (Alberti et al. 2018a), which might be the results of flow-induced effects on fibre orientation during the moulding of the flowable ECC. This effect needs to be further investigated in another study as the initial orientation and distribution of fibres in the funnel are not considered in this research.
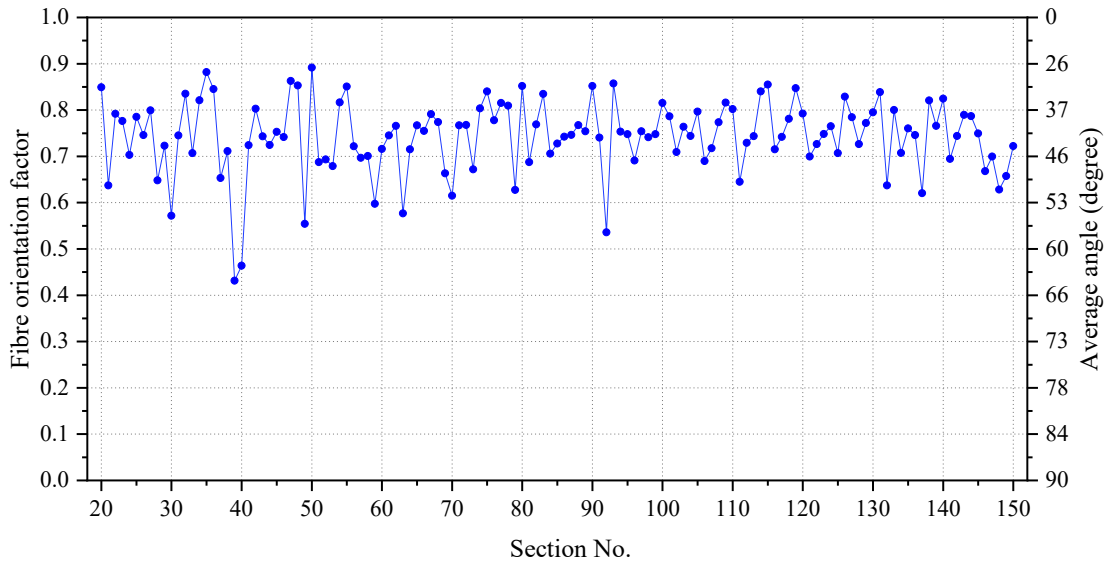
Figure 6.10   Variation of the average fibre orientation factor θ_i along the specimen.

6.3.2.2 Fibre distribution

Theoretically, the number of fibre at section i can be calculated based on the orientation factor θ_i as

$$n_{fi}=\theta_i\frac{A}{A_f}V_f \tag{6.7}$$

where A, A_f are the cross-section of the specimen and a fibre, respectively. However, for bendable synthetic fibres, their bending phenomena in the matrix also influence the number of fibres at fracture planes of the specimen. For this reason, the bending ratio or length- reduction factor R_f should be taken into account as follows:

$$n_{fi}=R_f\theta_i\frac{A}{A_f}V_f \tag{6.8}$$

Using the values of R_f, θ_i obtained above, the theoretical numbers of fibres at different sections are obtained and shown in Figure 6.11, together with the simulated number of fibres at different sections along the specimen.

147
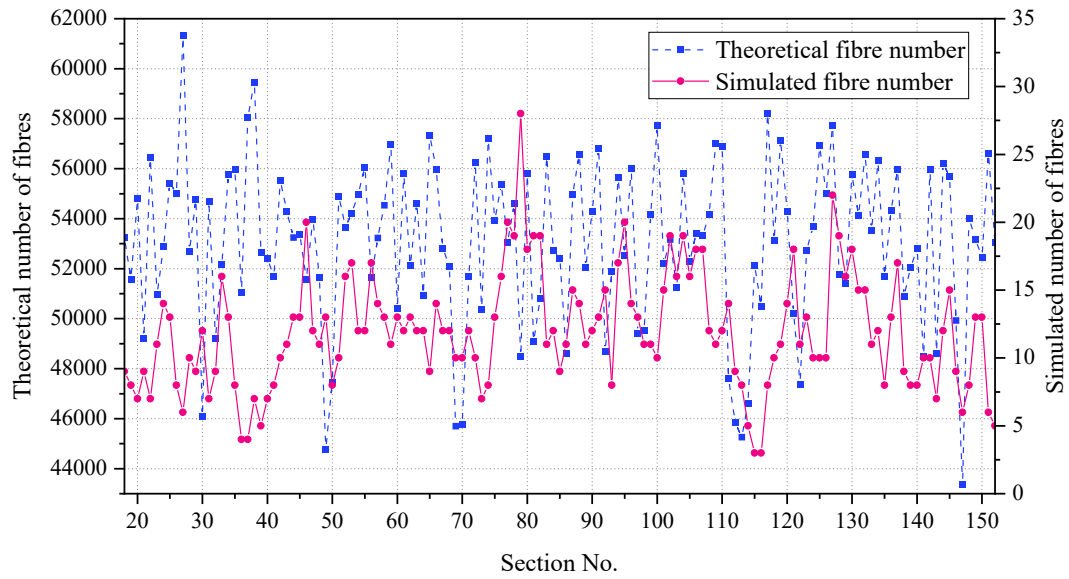
Figure 6.11   Difference between the theoretical and simulated number of fibres.

As can be seen in Figure 6.11, there is a tremendous difference between the theoretical and simulated number of fibres at multi-vertical sections of the specimen. Except for some poor dispersion sections due to the initial creation of fibre in the funnel, the theoretical number of fibres is approximately 2,000 to 10,000 times larger than the simulated fibre number. Within the scope of this study, it is simplified to assume that each inclined fibre at section i in the simulation represents a group of an average value, i.e., 6,000 fibres having a similar inclination but different embedment length L_e with the crack plane i in the specimen. Adopting this assumption, the results of fibre orientation and distribution at cutting planes from the moulding simulation will be implemented into the bridging model to obtain the $\sigma(\delta)$ relationships at different sections, which are presented in the following sections. With the identified number of fibres, the bridging stress is calculated by summing the tension forces in all contributing fibres at a crack opening, and then divided by the cross-sectional area of the specimen.

6.3.3 Peak bridging strength at various sections

From the fibre-bridging law, it is clear that the number of fibres, their orientation and embedment lengths in the matrix primarily determine the peak bridging strength at a cracked plane. Thus, by computing the bridging law of each section, the peak bridging strengths along the specimen are obtained. From Figure 6.12, the variation of fibre distribution can be mainly explained for the fluctuation of peak bridging stress at various sections. The poor dispersion of fibres can lead to sudden rupture of structural members when cracks occur at low fibre content sections since the strength criterion is not satisfied. This result demonstrates the role of fibre dispersion in the fresh mixture of ECC (Zhou et al. 2012; Li & Li 2013). Thus, the consistent tensile strain-hardening behaviour of ECC specimens might only be achieved when fibres are homogeneously distributed in the cementitious matrix of specimens.
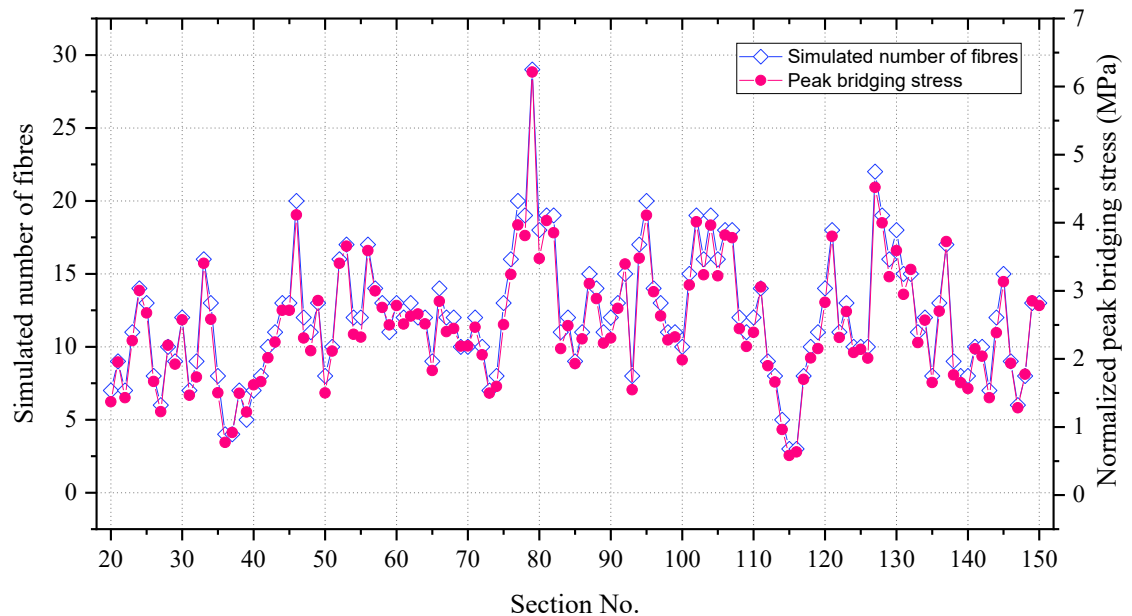
Figure 6.12　Correlation between the number of inclined fibre and peak bridging stress at sections.

6.3.4 Stress-crack opening relationships of different fibre orientation distributions

Since synthetic fibres can be bent or coiled, their inclination with loading axis might vary even with adjacent sections. To clarify this influence of the fibre bending phenomenon, the details of fibre orientation distribution at four consecutive sections from Section-102 to Section-105 are thoroughly considered. The orientation factors and histogram of inclination angles of intersected fibres at four adjacent sections are shown in Figure 6.13 and Figure 6.14. The remarkable variation of fibre orientation distribution can be observed, even with two adjacent sections. From the graphs, only a few fibres have a similar inclination at two nearby sections, such as fibre No.4 at Section-102 and Section-103 or fibre No.10 at Section-103 and Section-104. This result demonstrates the complexity of the orientation distribution of flexible synthetic fibres in the matrix of ECC.
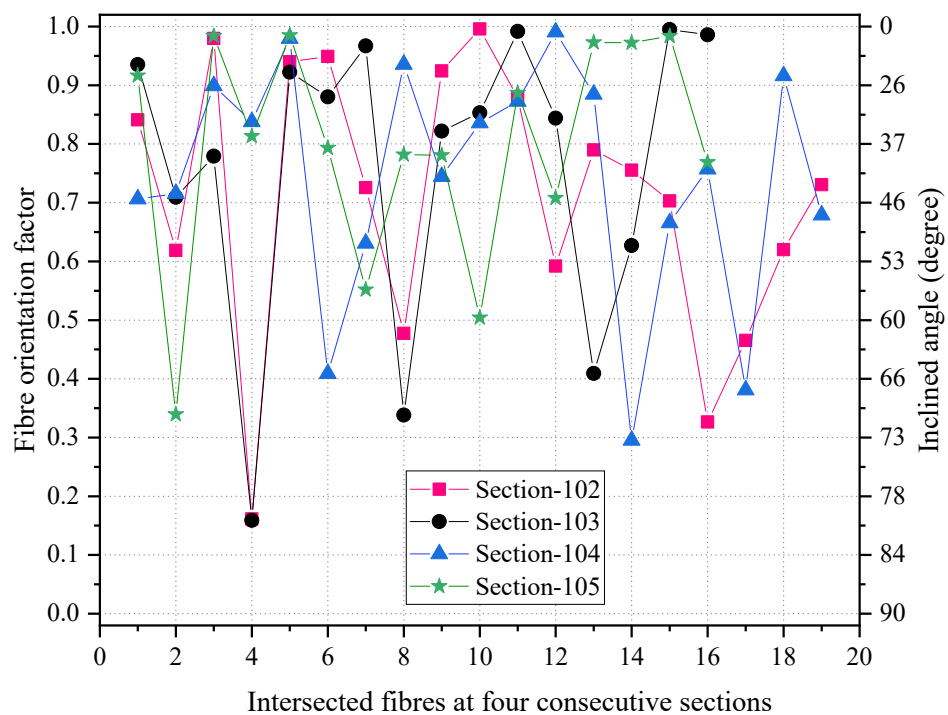
Figure 6.13   The variation of fibre inclination at four consecutive sections.
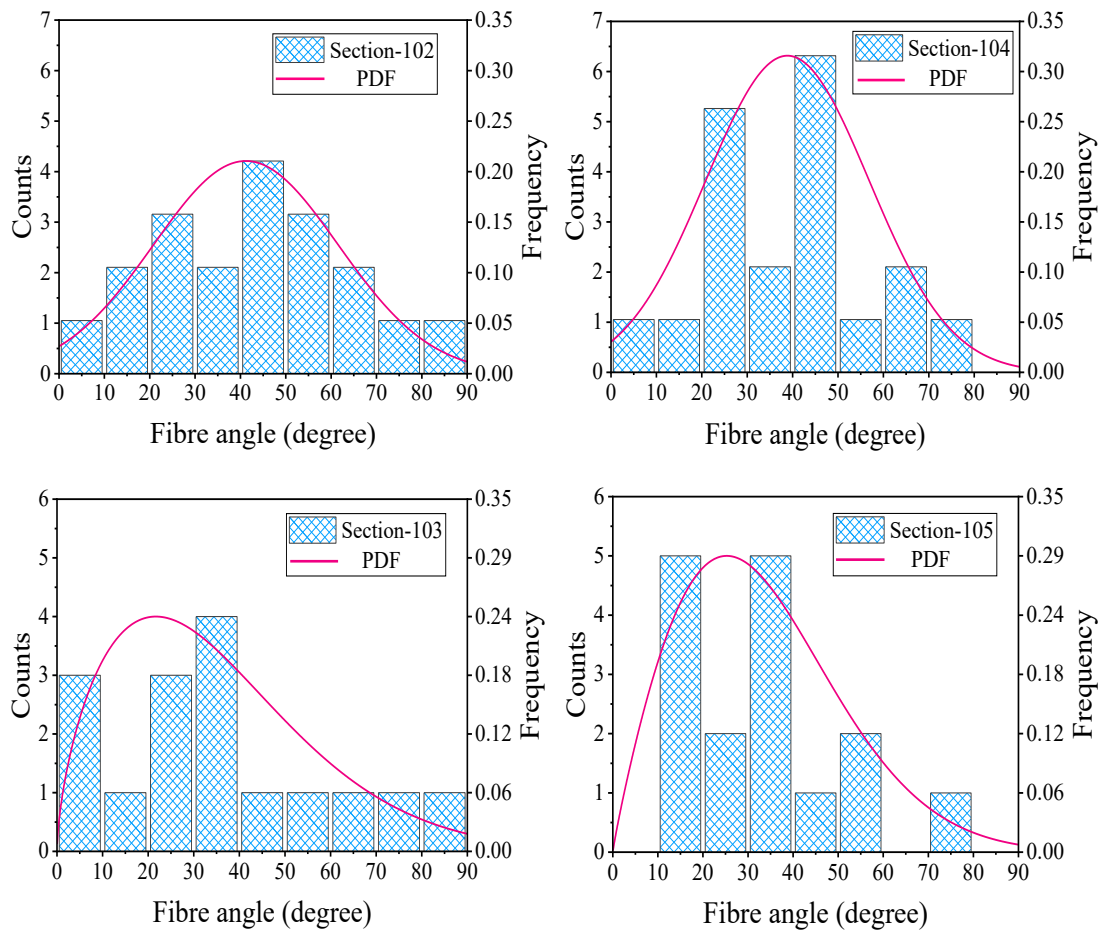
Figure 6.14   Histogram of fibre inclination at four consecutive sections.

The numerical predictions of the σ - δ curves at the four consecutive sections above are also computed and shown in Figure 6.15. For Section-102 and Section-104 having more fibre counted at the cutting plane than Section-103 and Section-105, the peak stresses are also significantly higher. Although possessing the same number of intersected fibres, the ultimate tensile stress in Sections-102 and -103 are slightly higher than that at Sections-104 and -105, respectively. Particularly, the peak stress at Section-102 reaches 4.03 MPa in comparison with the value of 3.97 MPa at Section-104. The peak stress value has increased by 1.51% as a result of well-distributed fibre inclination in Section - 102 than Section-104, as can be seen at their histograms in Figure 6.14.

Moreover, the crack openings at peak stresses are consistently around 40 μm to 50 μm, which agrees with the reported average value of the crack opening in ECC.
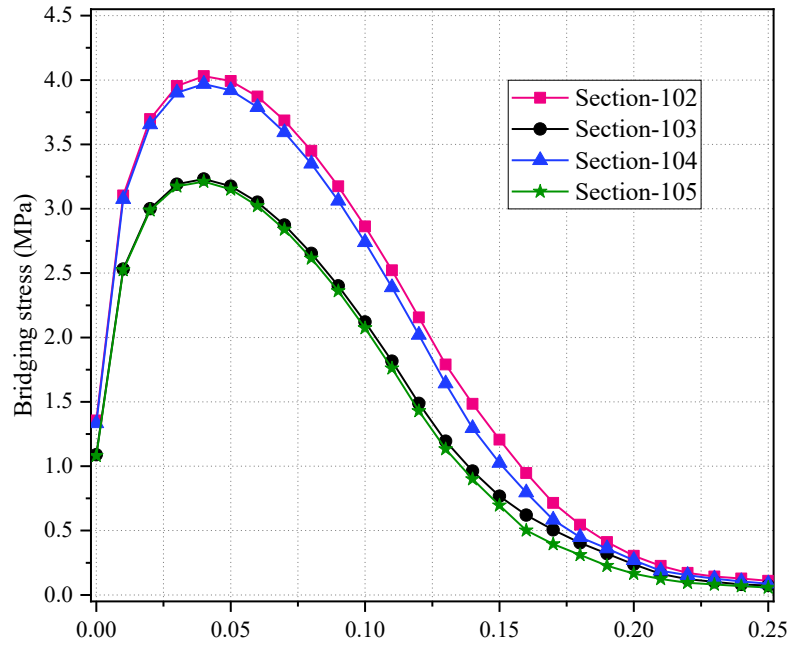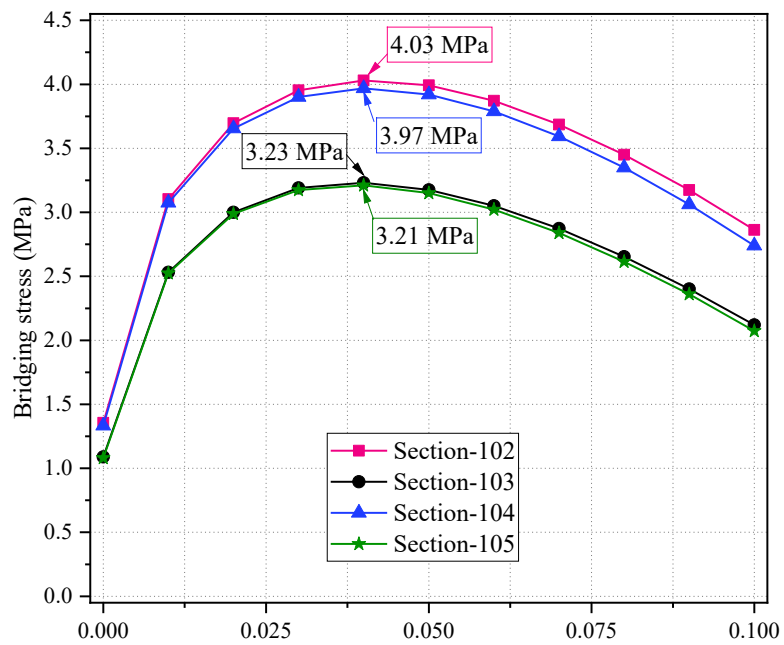
Figure 6.15   Influence of fibre orientation and distribution on the σ - δ relationship at four consecutive sections from 102 to 105: (a) full span view; (b) magnified view of (a) with δ = 0 ~ 0.1 mm.

6.4 Conclusions

This chapter proposes an innovative approach to numerically investigate the distribution and orientation of bendable synthetic fibre and their influence on the tensile performance through two-state consideration of ECC. At the fresh state, the moulding process of fresh ECC is simulated by using the mesh-free 3D SPH modelling. Thus, the orientation and distribution of flexible synthetic fibres at multiple vertical sections along the specimen are quantified. A fibre-bridging model at the hardened state of ECC is also developed. The model specifically consider the two-way pullout mechanisms of an inclined fibre displacement when bearing the tensile stress released from the cracked matrix. Results of the developed fibre-bridging model fit well with experimental data in comparison with existing models, especially during the pullout stage of fibre. Then, the obtained information of fibre orientation/distribution from the moulding simulation is implemented in the bridging model to acquire the tensile behaviour of ECC at those sections.

The results of the benchmark example demonstrate the proposed approach can be a potential tool so that the orientation and distribution of flexible synthetic fibre and their correlation with the tensile strain-hardening behaviour of ECC are much better understood. According to the word done in this chapter, the bending of flexible synthetic fibres can be recognised as a complex phenomenon which varies fibre orientation distributions and also reduces the number of fibres at the cross-sections. This in turn reduces the fibres' efficiency in bridging cracks in ECC materials.

Chapter 7

Conclusions and Recommendations for Future Research

7.1 Summary and Conclusions

The conducted research work in this thesis was in the following plan: firstly, to model the behaviour of flowable ECC; secondly, to evaluate the distribution and orientation of flexible synthetic fibres and, thirdly to investigate their effects on the tensile performance of ECC specimens. As the results, the numerical models were successfully developed to investigate the behaviour of ECC at its both fresh state and hardened state. Based on the work embodied from Chapters 3 to 6, the main achievements of this study are grouped with regard to two states of ECC and summarised in the two following sections.

7.1.1 Modelling flowable ECC at the fresh state

At the fresh state of ECC, numerical methods were developed to model the flow of fresh ECC, aiming to obtain the insights of ECC flow as well as the distribution and orientation of flexible synthetic fibres in the cementitious matrix of fresh ECC. The developed models focused on the flow behaviour of self-consolidating (SC or flowable) ECC, which was described as a non-Newtonian viscous fluid. The Lagrangian form of the Navier-Stokes constitutive equations of the SC-ECC was solved using the mesh-free, weakly compressible smoothed particle hydrodynamics (WCSPH). Synthetic fibres utilised in SC-ECC were considered as flexible fibres and modelled as separated particles, virtually connected by a drag force between two adjacent fibre particles. Fibre particles and mortar particles possessed similar continuum properties in the domain of SC-ECC. Since the non-Newtonian flow of SC-ECC is governed by its plastic viscosity and yield stress, which could not be accurately measured by rheometers, the yield stress was first assumed, then an enormous error trial-corrector using SPH modelling was

conducted for estimating the plastic viscosity of fresh mix. Also, the repulsive force particles method was applied to model the rigid wall boundary. Analogously with inter-molecular forces, the boundary particles in the influence range of the smoothing kernel exert central forces when fluid particles approach the boundary. This technique helps to prevent fluid particles penetrating the boundaries, which are also modelled as separated particles in the SPH. Moreover, due to the lack of surrounding particles in the supported range of the kernel function along boundaries or at the free surface, a constant correction of kernel function was implemented to ensure its consistency and normalised conditions being satisfied. The main conclusions drawn from the research works at the fresh state of ECC are given as follows:

- In the 2D model (Chapter 3), the slump flow tests were simulated with both mini cone and conventional cone. The numerical results of fresh mix spreads in both tests were found to be consistent with the obtained experimental data from the literature. The correlations between the wall-effects, the distance of flow, the casting position with the orientation and the distribution of synthetic fibres were also investigated. The results indicated that synthetic fibres tend to parallel to the bottom of formwork at the casting position and near the bottom wall. Also, fibres tend to coil near the end-vertical walls and at the surface of the specimen. Additionally, the influence of the flow on the fibres orientation and distribution gradually diminish when the flow distance increases from the casting position.

- In Chapter 4, the developed 2D model was extended to 3D model for obtaining the factual image of the ECC flow, the actual distribution and orientation of synthetic fibres in fresh mixtures. This is due to the obtained results of 2D simulation were somewhat inaccurate since the interaction between particles

occurred in a single plane. The calibration of the fibre number and the maximum inclination of fibre was restrict to 30^0 to suit the 2D model, which also affected the behaviour of the flowable ECC. The 3D model was validated through results of the V-funnel test and U-box test of flowable ECC. The V-funnel model focused on the flow rate characteristic and correlation of the dispersion of synthetic fibres with the plastic viscosity of fresh mixtures. The U-box simulation confirmed the self-consolidating capability and passing ability of SC-ECC flow through reinforcing bars. The simulation results of the discharge time in the V-funnel model and self-levelling index in the U-box model agreed well with experimental data. In this way, convincing evidence was provided for the correctness and effectiveness of the developed 3D model. The proposed model could therefore offer insights into the SC-ECC flow behaviour in terms of filling, passing abilities and dispersion/orientation of flexible synthetic fibres. In addition, the influences of plastic viscosity and steel bar obstacles on the distribution of fibres were also examined. The presence of steel bars has shown significant effects on the flow of fresh ECC and the dispersion of fibres. Steel bars could reduce the speed flow of fresh mix and also lessened the well-dispersion of fibres in the ECC matrix. Moreover, with the same yield stress, fibres have shown a tendency to disperse well in the higher plastic viscosity mixture than the lower one.

- The successfully developed 3D model was then implemented to simulate the moulding of fresh ECC. Since one of the advantages of the SPH method is to allow tracking the movement of fibre particles, the information regarding fibres orientation and distribution in the whole specimen can be identified. The bending phenomenon of flexible synthetic fibres during their flow was also considered, and

a general bending trend of flexible synthetic fibres was introduced. A bending ratio is then proposed for determining the distribution factor of flexible synthetic fibres in ECC.

7.1.2 Evaluation of fibre orientation and distribution and the tensile behaviour of ECC at the hardened state

At the hardened state of ECC, the evaluation of fibre orientation and distribution in ECC specimen and their effects on the featured and unique strain-hardening behaviour of ECC were studied. From the fresh state, the simulated specimen was considered as transferring into the hardened state when materials stop flowing in the moulds. The main conclusions drawn from the research work at the hardened state of ECC are given as follows:

- A simple method was first proposed to evaluate the orientation and distribution of flexible synthetic fibres at various sections of SC-ECC specimens. The effect of specimen thickness on the orientation of synthetic fibres is investigated through the simulation of the casting of fresh SC-ECC into different thicknesses of moulds. The results revealed that thin specimens tend to have higher fibre orientation factors than thick specimens. The tendency of fibre rotation was confirmed to parallel with the longitudinal direction of specimens at the bottom of the formwork and rotate freely at the top surface of specimens (Chapter 5). Furthermore, it was observed that the bendings of fibres significantly vary the distribution of their orientations within adjacent sections of ECC specimen (Chapter 6).

- A fibre-bridging model of a single crack at the lower mesoscale was also developed based on the two-way pullout mechanisms of an arbitrarily inclined

fibre (Chapter 6). The model has considered the snubbing effect and strength reduction of inclined fibres when being pulled out from both sides of a matrix crack plane. The obtained results of the stress-crack opening relationship fitted well with reported experimental data of 0.1% and 0.5% volume fraction of PVA fibre. Moreover, in comparison with existing models, the proposed model has shown a better prediction of stress-crack opening relationship during the fibre pullout stage. Through examining different groups of fibre inclination, the attained ultimate tensile strengths and corresponding crack openings significantly increased for the group of fibres exhibiting a smaller inclination. These findings emphasised the role of controlled orientation of fibres to a small degree for preventing their premature rupture, which might be achieved in the 3D printing technique as fibres are well-oriented through the nozzle of a printer.

- A novel approach was finally proposed aiming to link the obtained data of fibres distribution and orientation with the strain-hardening behaviour of ECC (Chapter 6). For this purpose, the obtained orientation and distribution of fibres from the moulding simulation were incorporated into the developed bridging model to acquire the peak bridging stress at multi-vertical sections along the ECC specimen. The stress-crack opening relationship at consecutive sections of the specimen was also computed to expose the distinct effect of fibre distribution and fibre orientation on the tensile performance of ECC. For the stress-crack opening relationship at crack planes, while the number of intersected fibres mainly governs the peak bridging stresses and strain capacity, the corresponding distribution of fibre orientations shows a slight effect on those properties of ECC.

7.2 Recommendations for Future Research

The developed models in this PhD research have successfully provided practical insights into the flow characteristics of flowable ECC at the fresh state and real picture of flexible synthetic fibres in the mixture. The information regarding fibres distribution and orientation and their correlation with the tensile behaviour of ECC are also explored. However, there are still a number of possible enhancements, which can be worthwhile for future research efforts, as follows:

- Mixing procedures have been illustrated as wielding a significant effect on the dispersion of fibres. Also, synthetic fibres might be bent in the cementitious matrix during the mixing process. For this reason, it is worthwhile to extend the developed 3D model in this thesis to simulate the mixing process of ECC. At this step, different histograms of fibre distribution and orientation before mixing should be considered. Besides, the number of fibres in the simulation could be increased to diminish the remarkable difference with the actual fibres in specimens.

- Though the U-box test, the influences of steel obstacles on flow characteristics of fresh ECC and the dispersion and orientation of bendable fibres have been observed. To further clarify and quantify those influences, experimental and numerical studies should be conducted at the real scale of steel-ECC structures.

- ECC materials exhibit unique strain-hardening behaviour through the stress transferring, steady forming multiple flat cracks thanks to bridging fibres at different sections across structural members. Thus, the developed fibre-bridging model at the lower mesoscale and the novel two states approach in Chapter 6 are desirable to combine and develop to the upper mesoscale and macroscale level of ECC.

- The developed 3D SPH model is also worthwhile to extend for modelling of the extrusion process of printable ECC. Through this approach, the orientation and distribution of flexible fibres at each layer of 3D printing can be observed and evaluated. This model approach can also be used to assess the correlation between fresh state properties of printable ECC with the deformation of filaments and the stability of 3D printed structures.

References

References

Abrishambaf, A., Pimentel, M. & Nunes, S. 2017, 'Influence of fibre orientation on the tensile behaviour of ultra-high performance fibre reinforced cementitious composites', *Cement and Concrete Research*, vol. 97, pp. 28-40.

Ahmad, S. & Umar, A. 2018, 'Rheological and mechanical properties of self-compacting concrete with glass and polyvinyl alcohol fibres', *Journal of Building Engineering*, vol. 17, pp. 65-74.

AL-Rubaye, M., Kulasegaram, S. & Karihaloo, B.L. 2017, 'Simulation of self-compacting concrete in an L-box using smooth particle hydrodynamics', *Magazine of Concrete Research*, vol. 69, no. 12, pp. 618-28.

Alberti, M., Enfedaque, A. & Gálvez, J. 2018a, 'A review on the assessment and prediction of the orientation and distribution of fibres for concrete', *Composites Part B: Engineering*.

Alberti, M.G., Enfedaque, A. & Gálvez, J.C. 2017, 'On the prediction of the orientation factor and fibre distribution of steel and macro-synthetic fibres for fibre-reinforced concrete', *Cement and Concrete Composites*, vol. 77, pp. 29-48.

Alberti, M.G., Enfedaque, A. & Gálvez, J.C. 2018b, 'A review on the assessment and prediction of the orientation and distribution of fibres for concrete', *Composites Part B: Engineering*.

Alberti, M.G., Enfedaque, A., Gálvez, J.C. & Agrawal, V. 2016, 'Fibre distribution and orientation of macro-synthetic polyolefin fibre reinforced concrete elements', *Construction and Building Materials*, vol. 122, pp. 505-17.

Alyhya, W., Kulasegaram, S. & Karihaloo, B. 2017, 'Simulation of the flow of self-compacting concrete in the V-funnel by SPH', *Cement and Concrete Research*, vol. 100, pp. 47-59.

Anderson, J.D. 1992, 'Governing equations of fluid dynamics', *Computational fluid dynamics*, Springer, pp. 15-51.

Aveston, J. & Kelly, A. 1973, 'Theory of multiple fracture of fibrous composites', *Journal of Materials Science*, vol. 8, no. 3, pp. 352-62.

Badry, F., Kulasegaram, S. & Karihaloo, B.L. 2016, 'Estimation of the yield stress and distribution of large aggregates from slump flow test of self-compacting concrete

mixes using smooth particle hydrodynamics simulation', *Journal of Sustainable Cement-Based Materials*, vol. 5, no. 3, pp. 117-34.

Beaupré, D., Chapdelaine, F., Domone, P., Koehler, E., Shen, L., Sonebi, M., Struble, L., Tepke, D., Wallevik, J. & Wallevik, O. 2004, 'Comparison of concrete rheometers: International tests at MBT (Cleveland OH, USA) in May 2003'.

Becker, M. & Teschner, M. 2007, 'Weakly compressible SPH for free surface flows', *Proceedings of the 2007 ACM SIGGRAPH/Eurographics Symposium on Computer Animation*, Eurographics Association, pp. 209-17.

Bentur, A. & Mindess, S. 2014, *Fibre reinforced cementitious composites*, CRC Press.

Bi, J., Bao, C., Xu, D., Guan, J. & Cheng, W. 2017, 'Numerical simulation of the distribution and orientation of steel fibres in the SCC', *Magazine of Concrete Research*, pp. 1-12.

Bi, J., Zhao, Y., Guan, J., Huo, L., Qiao, H. & Yuan, L. 2019, 'Three-dimensional modeling of the distribution and orientation of steel fibers during the flow of self-compacting concrete', *Structural Concrete*, vol. 0, no. 0.

Bonet, J. & Kulasegaram, S. 2000, 'Correction and stabilization of smooth particle hydrodynamics methods with applications in metal forming simulations', *International Journal for Numerical Methods in Engineering*, vol. 47, no. 6, pp. 1189-214.

Bonet, J. & Lok, T.S.L. 1999, 'Variational and momentum preservation aspects of Smooth Particle Hydrodynamic formulations', *Computer Methods in Applied Mechanics and Engineering*, vol. 180, no. 1, pp. 97-115.

Boulekbache, B., Hamrat, M., Chemrouk, M. & Amziane, S. 2010, 'Flowability of fibre-reinforced concrete and its effect on the mechanical properties of the material', *Construction and Building Materials*, vol. 24, no. 9, pp. 1664-71.

Brandt, A.M. 2008, 'Fibre reinforced cement-based (FRC) composites after over 40 years of development in building and civil engineering', *Composite Structures*, vol. 86, no. 1, pp. 3-9.

Cao, G. & Li, Z. 2017, 'Numerical flow simulation of fresh concrete with viscous granular material model and smoothed particle hydrodynamics', *Cement and Concrete Research*, vol. 100, no. Supplement C, pp. 263-74.

Cercos-Pita, J.L. 2015, 'AQUAgpusph, a new free 3D SPH solver accelerated with OpenCL', *Computer Physics Communications*, vol. 192, pp. 295-312.

Cotterell, B. & Mai, Y.-W. 2014, *Fracture Mechanics of Cementitious Materials*, CRC Press.

Crespo, A., Gómez-Gesteira, M. & Dalrymple, R.A. 2007, 'Boundary conditions generated by dynamic particles in SPH methods', *CMC-TECH SCIENCE PRESS*-, vol. 5, no. 3, p. 173.

Crespo, A.J., Domínguez, J.M., Rogers, B.D., Gómez-Gesteira, M., Longshaw, S., Canelas, R., Vacondio, R., Barreiro, A. & García-Feal, O. 2015, 'DualSPHysics: Open-source parallel CFD solver based on Smoothed Particle Hydrodynamics (SPH)', *Computer Physics Communications*, vol. 187, pp. 204-16.

Cross, M.M. 1965, 'Rheology of non-Newtonian fluids: A new flow equation for pseudoplastic systems', *Journal of Colloid Science*, vol. 20, no. 5, pp. 417-37.

Cummins, S.J. & Rudman, M. 1999, 'An SPH projection method', *Journal of Computational Physics*, vol. 152, no. 2, pp. 584-607.

Dalrymple, R.A. & Knio, O. 2001, 'SPH modelling of water waves', *Coastal Dynamics' 01*, pp. 779-87.

Dalrymple, R.A. & Rogers, B.D. 2006, 'Numerical modeling of water waves with the SPH method', *Coastal Engineering*, vol. 53, no. 2, pp. 141-7.

De Larrard, F., Ferraris, C. & Sedran, T. 1998, 'Fresh concrete: A Herschel-Bulkley material', *Materials and Structures*, vol. 31, no. 7, pp. 494-8.

Deeb, R. 2013, 'Flow of self-compacting concrete', Cardiff University.

Deeb, R., Karihaloo, B. & Kulasegaram, S. 2014, 'Reorientation of short steel fibres during the flow of self-compacting concrete mix and determination of the fibre orientation factor', *Cement and Concrete research*, vol. 56, pp. 112-20.

Deeb, R., Kulasegaram, S. & Karihaloo, B.L. 2014a, '3D modelling of the flow of self-compacting concrete with or without steel fibres. Part I: slump flow test', *Computational Particle Mechanics*, vol. 1, no. 4, pp. 373-89.

Deeb, R., Kulasegaram, S. & Karihaloo, B.L. 2014b, '3D modelling of the flow of self-compacting concrete with or without steel fibres. Part II: L-box test and the assessment of fibre reorientation during the flow', *Computational Particle Mechanics*, vol. 1, no. 4, pp. 391-408.

Dhaheer, M.A., Kulasegaram, S. & Karihaloo, B. 2016, 'Simulation of self-compacting concrete flow in the J-ring test using smoothed particle hydrodynamics (SPH)', *Cement and Concrete Research*, vol. 89, pp. 27-34.

Ding, C., Guo, L. & Chen, B. 2020, 'Orientation distribution of polyvinyl alcohol fibers and its influence on bridging capacity and mechanical performances for high ductility cementitious composites', *Construction and Building Materials*, vol. 247, p. 118491.

Feldman, J. & Bonet, J. 2007, 'Dynamic refinement and boundary contact forces in SPH with applications in fluid flow problems', *International Journal for Numerical Methods in Engineering*, vol. 72, no. 3, pp. 295-324.

Felekoğlu, B., Tosun-Felekoğlu, K. & Gödek, E. 2015, 'A novel method for the determination of polymeric micro-fiber distribution of cementitious composites exhibiting multiple cracking behavior under tensile loading', *Construction and Building Materials*, vol. 86, pp. 85-94.

Ferrand, M., Laurence, D., Rogers, B.D., Violeau, D. & Kassiotis, C. 2013, 'Unified semi-analytical wall boundary conditions for inviscid, laminar or turbulent flows in the meshless SPH method', *International Journal for Numerical Methods in Fluids*, vol. 71, no. 4, pp. 446-72.

Ferrara, L., Cremonesi, M., Tregger, N., Frangi, A. & Shah, S.P. 2012, 'On the identification of rheological properties of cement suspensions: Rheometry, computational fluid dynamics modeling and field test measurements', *Cement and Concrete Research*, vol. 42, no. 8, pp. 1134-46.

Ferrara, L., Ozyurt, N. & Di Prisco, M. 2011, 'High mechanical performance of fibre reinforced cementitious composites: the role of "casting-flow induced" fibre orientation', *Materials and Structures*, vol. 44, no. 1, pp. 109-28.

Fischer, G. & Li, V.C. 2007, 'Effect of fiber reinforcement on the response of structural members', *Engineering Fracture Mechanics*, vol. 74, no. 1-2, pp. 258-72.

Fischer, G. & Shuxin, W. 2003, 'Design of engineered cementitious composites (ECC) for processing and workability requirements', *Brittle Matrix Composites 7*, Elsevier, pp. 29-36.

Fulk, D.A. & Quinn, D.W. 1996, 'An analysis of 1-D smoothed particle hydrodynamics kernels', *Journal of Computational Physics*, vol. 126, no. 1, pp. 165-80.

Ghafoori, N. & Diawara, H. 2010, 'Influence of temperature on fresh performance of self-consolidating concrete', *Construction and Building Materials*, vol. 24, no. 6, pp. 946-55.

Ghanbari, A. & Karihaloo, B.L. 2009, 'Prediction of the plastic viscosity of self-compacting steel fibre reinforced concrete', *Cement and Concrete Research*, vol. 39, no. 12, pp. 1209-16.

Gingold, R.A. & Monaghan, J.J. 1977, 'Smoothed particle hydrodynamics: Theory and application to non-spherical stars', *Monthly Notices of The Royal Astronomical Society*, vol. 181, no. 3, pp. 375-89.

Gomez-Gesteira, M., Rogers, B.D., Crespo, A.J.C., Dalrymple, R.A., Narayanaswamy, M. & Dominguez, J.M. 2012, 'SPHysics – development of a free-surface fluid solver – Part 1: Theory and formulations', *Computers & Geosciences*, vol. 48, pp. 289-99.

Gomez-Gesteira, M., Rogers, B.D., Dalrymple, R.A. & Crespo, A.J. 2010, 'State-of-the-art of classical SPH for free-surface flows', *Journal of Hydraulic Research*, vol. 48, no. S1, pp. 6-27.

Hackman, L.E., Farrell, M.B. & Dunham, O.O. 1992, 'Slurry infiltrated mat concrete (SIMCON)', *Concrete International*, vol. 14, no. 12, pp. 53-6.

Hedong, X.S.L. 2008, 'A review on the development of research and application of ultra high toughness cementitious composites [J]', *China Civil Engineering Journal*, vol. 6, p. 012.

Huang, H., Gao, X., Li, L. & Wang, H. 2018, 'Improvement effect of steel fiber orientation control on mechanical performance of UHPC', *Construction and Building Materials*, vol. 188, pp. 709-21.

Huang, H., Gao, X., Li, Y. & Su, A. 2020, 'SPH simulation and experimental investigation of fiber orientation in UHPC beams with different placements', *Construction and Building Materials*, vol. 233, p. 117372.

Huang, H., Gao, X. & Zhang, A. 2019, 'Numerical simulation and visualization of motion and orientation of steel fibers in UHPC under controlling flow condition', *Construction and Building Materials*, vol. 199, pp. 624-36.

Huang, H., Su, A., Gao, X. & Yang, Y. 2019, 'Influence of formwork wall effect on fiber orientation of UHPC with two casting methods', *Construction and Building Materials*, vol. 215, pp. 310-20.

Huang, T., Zhang, Y., Su, C. & Lo, S. 2015, 'Effect of slip-hardening interface behavior on fiber rupture and crack bridging in fiber-reinforced cementitious composites', *Journal of Engineering Mechanics*, vol. 141, no. 10, p. 04015035.

Huang, T., Zhang, Y.X. & Yang, C. 2016, 'Multiscale modelling of multiple-cracking tensile fracture behaviour of engineered cementitious composites', *Engineering Fracture Mechanics*, vol. 160, pp. 52-66.

Huang, X. & Garcia, M.H. 1998, 'A Herschel–Bulkley model for mud flow down a slope', *Journal of Fluid Mechanics*, vol. 374, pp. 305-33.

Huang, Y., Li, H. & Qian, S. 2018, 'Self-sensing properties of engineered cementitious composites', *Construction and Building Materials*, vol. 174, pp. 253-62.

Hughes, J.P. & Graham, D.I. 2010, 'Comparison of incompressible and weakly-compressible SPH models for free-surface water flows', *Journal of Hydraulic Research*, vol. 48, no. S1, pp. 105-17.

Idelsohn, S.R., Oñate, E. & Pin, F.D. 2004, 'The particle finite element method: A powerful tool to solve incompressible flows with free-surfaces and breaking

waves', *International Journal for Numerical Methods in Engineering*, vol. 61, no. 7, pp. 964-89.

Johnson, G.R., Stryk, R.A. & Beissel, S.R. 1996, 'SPH for high velocity impact computations', *Computer Methods in Applied Mechanics and Engineering*, vol. 139, no. 1-4, pp. 347-73.

Joung, C.G., Phan-Thien, N. & Fan, X.J. 2001, 'Direct simulation of flexible fibers', *Journal of Non-Newtonian Fluid Mechanics*, vol. 99, no. 1, pp. 1-36.

Kabele, P. 2007, 'Multiscale framework for modeling of fracture in high performance fiber reinforced cementitious composites', *Engineering Fracture Mechanics*, vol. 74, no. 1, pp. 194-209.

Kanakubo, T., Miyaguchi, M. & Asano, K. 2016, 'Influence of fiber orientation on bridging performance of polyvinyl alcohol fiber-reinforced cementitious composite', *ACI Materials Journal*, vol. 113, no. 2.

Kanda, T., Hiraishi, M. & Sakata, N. 2004, 'Tensile properties of ECC in full-scale production', *Fifth International Conference on Fracture Mechanics of Concrete and Structures*, pp. 1013-20.

Kanda, T. & Li, V.C. 1998, 'Interface property and apparent strength of high-strength hydrophilic fiber in cement matrix', *Journal of Materials in Civil Engineering*, vol. 10, no. 1, pp. 5-13.

Kanda, T., Nagai, S., Maruta, M. & Yamamoto, Y. 2011, 'New high-rise R/C structure using ECC coupling beams', *2nd International RILEM Conference on Strain Hardening Cementitious Composites, Rio de Janeiro*, pp. 12-4.

Kang, J. & Bolander, J.E. 2015, 'Multiscale modeling of strain-hardening cementitious composites', *Mechanics Research Communications*.

Kang, S.-T. & Kim, J.-K. 2011, 'The relation between fiber orientation and tensile behavior in an Ultra High Performance Fiber Reinforced Cementitious Composites (UHPFRCC)', *Cement and Concrete Research*, vol. 41, no. 10, pp. 1001-14.

Kim, J.-K., Kim, J.-S., Ha, G.J. & Kim, Y.Y. 2007, 'Tensile and fiber dispersion performance of ECC (engineered cementitious composites) produced with

ground granulated blast furnace slag', *Cement and Concrete Research*, vol. 37, no. 7, pp. 1096-105.

Kong, H.-J., Bike, S.G. & Li, V.C. 2003a, 'Constitutive rheological control to develop a self-consolidating engineered cementitious composite reinforced with hydrophilic poly (vinyl alcohol) fibers', *Cement and Concrete Composites*, vol. 25, no. 3, pp. 333-41.

Kong, H.-J., Bike, S.G. & Li, V.C. 2003b, 'Development of a self-consolidating engineered cementitious composite employing electrosteric dispersion/stabilization', *Cement and Concrete Composites*, vol. 25, no. 3, pp. 301-9.

Kostrzanowska-Siedlarz, A. & Gołaszewski, J. 2016, 'Rheological properties of high performance self-compacting concrete: Effects of composition and time', *Construction and Building Materials*, vol. 115, pp. 705-15.

Kulasegaram, S., Bonet, J., Lewis, R. & Profit, M. 2004, 'A variational formulation based contact algorithm for rigid boundaries in two-dimensional SPH applications', *Computational Mechanics*, vol. 33, no. 4, pp. 316-25.

Kulasegaram, S. & Karihaloo, B.L. 2013, 'Fibre-reinforced, self-compacting concrete flow modelled by smooth particle hydrodynamics', *Proceedings of the Institution of Civil Engineers-Engineering and Computational Mechanics*, vol. 166, no. 1, pp. 22-31.

Kulasegaram, S., Karihaloo, B.L. & Ghanbari, A. 2011, 'Modelling the flow of self-compacting concrete', *International Journal for Numerical and Analytical Methods in Geomechanics*, vol. 35, no. 6, pp. 713-23.

Kunieda, M. & Rokugo, K. 2006, 'Recent progress on HPFRCC in Japan', *Journal of Advanced Concrete Technology*, vol. 4, no. 1, pp. 19-33.

Lankard, D.R. 1984, 'Slurry infiltrated fiber concrete (SIFCON): Properties and applications', *MRS Online Proceedings Library Archive*, vol. 42.

Lashkarbolouk, H., Halabian, A.M. & Chamani, M.R. 2014, 'Simulation of concrete flow in V-funnel test and the proper range of viscosity and yield stress for SCC', *Materials and Structures*, vol. 47, no. 10, pp. 1729-43.

Lee, B., Lee, Y., Kim, J. & Kim, Y. 2010, 'Micromechanics-based fiber-bridging analysis of strain-hardening cementitious composite accounting for fiber distribution', *Computer Modeling in Engineering & Sciences(CMES)*, vol. 61, no. 2, pp. 111-32.

Lee, B.Y., Kim, J.-K., Kim, J.-S. & Kim, Y.Y. 2009, 'Quantitative evaluation technique of polyvinyl alcohol (PVA) fiber dispersion in engineered cementitious composites', *Cement and Concrete Composites*, vol. 31, no. 6, pp. 408-17.

Lee, B.Y., Kim, J.-K. & Kim, Y.Y. 2010, 'Prediction of ECC tensile stress-strain curves based on modified fiber bridging relations considering fiber distribution characteristics', *Computers and Concrete*, vol. 7, no. 5, pp. 455-68.

Lee, E.S., Moulinec, C., Xu, R., Violeau, D., Laurence, D. & Stansby, P. 2008, 'Comparisons of weakly compressible and truly incompressible algorithms for the SPH mesh free particle method', *Journal of Computational Physics*, vol. 227, no. 18, pp. 8417-36.

Lepech, M.D. & Li, V.C. 2008, 'Large-scale processing of engineered cementitious composites', *ACI Materials Journal*, vol. 105, no. 4, pp. 358-66.

Lepech, M.D. & Li, V.C. 2009, 'Application of ECC for bridge deck link slabs', *Materials and Structures*, vol. 42, no. 9, p. 1185.

Leroy, A., Violeau, D., Ferrand, M. & Kassiotis, C. 2014, 'Unified semi-analytical wall boundary conditions applied to 2-D incompressible SPH', *Journal of Computational Physics*, vol. 261, pp. 106-29.

Leung, C.K. & Li, V.C. 1992, 'Effect of fiber inclination on crack bridging stress in brittle fiber reinforced brittle matrix composites', *Journal of the Mechanics and Physics of Solids*, vol. 40, no. 6, pp. 1333-62.

Leung, C.K. & Ybanez, N. 1997, 'Pullout of inclined flexible fiber in cementitious composite', *Journal of Engineering Mechanics*, vol. 123, no. 3, pp. 239-46.

Li, H., Xu, S. & Leung, C.K. 2009, 'Tensile and flexural properties of ultra high toughness cemontious composite', *Journal of Wuhan University of Technology-Mater. Sci. Ed.*, vol. 24, no. 4, pp. 677-83.

Li, M. & Li, V.C. 2013, 'Rheology, fiber dispersion, and robust properties of engineered cementitious composites', *Materials and Structures*, vol. 46, no. 3, pp. 405-20.

Li, S. & Liu, W.K. 2002, 'Meshfree and particle methods and their applications', *Applied Mechanics Reviews*, vol. 55, no. 1, pp. 1-34.

Li, V.C. 1993, 'From micromechanics to structural engineering-The design of cementitous composites for civil engineering applications', *J. Struct. Mech. Earthquake Eng., JSCE*, vol. 10, no. 2, pp. 37-48.

Li, V.C. 1998, 'Engineered cementitious composites-tailored composites through micromechanical modeling', *In: Fiber Reinforced Concrete: Present and the Future*, no. edited by N. Banthia, A. Bentur, A. and A. Mufti, Canadian Society for Civil Engineering, Montrea, pp. 64-97.

Li, V.C. 2002, 'Advances in ECC research', *ACI Special Publications*, vol. 206, pp. 373-400.

Li, V.C. 2003, 'On engineered cementitious composites (ECC)', *Journal of Advanced Concrete Technology*, vol. 1, no. 3, pp. 215-30.

Li, V.C. 2008, 'Engineered cementitious composites (ECC) material, structural, and durability performance', *In: Nawy E (ed) Concrete construction engineering handbook, CRC Press, Boca Raton, Chapter 24*.

Li, V.C., Bos, F.P., Yu, K., McGee, W., Ng, T.Y., Figueiredo, S.C., Nefs, K., Mechtcherine, V., Nerella, V.N., Pan, J., van Zijl, G.P.A.G. & Kruger, P.J. 2020, 'On the emergence of 3D printable Engineered, Strain Hardening Cementitious Composites (ECC/SHCC)', *Cement and Concrete Research*, vol. 132, p. 106038.

Li, V.C., Kong, H. & Chan, Y.-W. 1998, 'Development of self-compacting engineered cementitious composites', *Journal of Materials in Civil Engineering*, vol. 10, no. 2, p. 66.

Li, V.C. & Leung, C.K. 1992, 'Steady-state and multiple cracking of short random fiber composites', *Journal of Engineering Mechanics*, vol. 118, no. 11, pp. 2246-64.

Li, V.C., Lim, Y.M. & Chan, Y.-W. 1998, 'Feasibility study of a passive smart self-healing cementitious composite', *Composites Part B: Engineering*, vol. 29, no. 6, pp. 819-27.

Li, V.C. & Maalej, M. 1996, 'Toughening in cement based composites. Part II: Fiber reinforced cementitious composites', *Cement and Concrete Composites*, vol. 18, no. 4, pp. 239-49.

Li, V.C., Mishra, D.K. & Wu, H.-C. 1995, 'Matrix design for pseudo-strain-hardening fibre reinforced cementitious composites', *Materials and Structures*, vol. 28, no. 10, pp. 586-95.

Li, V.C., Wang, Y. & Backer, S. 1990, 'Effect of inclining angle, bundling and surface treatment on synthetic fibre pull-out from a cement matrix', *Composites*, vol. 21, no. 2, pp. 132-40.

Li, V.C., Wang, Y. & Backer, S. 1991, 'A micromechanical model of tension-softening and bridging toughening of short random fiber reinforced brittle matrix composites', *Journal of the Mechanics and Physics of Solids*, vol. 39, no. 5, pp. 607-25.

Li, V.C., Wu, C., Wang, S., Ogawa, A. & Saito, T. 2002, 'Interface tailoring for strain-hardening polyvinyl alcohol-engineered cementitious composite (PVA-ECC)', *Materials Journal*, vol. 99, no. 5, pp. 463-72.

Li, V.C. & Wu, H.-C. 1992, 'Conditions for pseudo strain-hardening in fiber reinforced brittle matrix composites', *Applied Mechanics Reviews*, vol. 45, no. 8, pp. 390-8.

Li, V.C., Wu, H.C. & Chan, Y.W. 1996, 'Effect of plasma treatment of polyethylene fibers on interface and ementitious composite properties', *Journal of the American Ceramic Society*, vol. 79, no. 3, pp. 700-4.

Lin, V.W., Li, M., Lynch, J.P. & Li, V.C. 2011, 'Mechanical and electrical characterization of self-sensing carbon black ECC', *Nondestructive Characterization for Composite Materials, Aerospace Engineering, Civil Infrastructure, and Homeland Security 2011*, vol. 7983, International Society for Optics and Photonics, p. 798316.

Lin, Z., Kanda, T. & Li, V.C. 1999, 'On interface property characterization and performance of fiber reinforced cementitious composites', *Journal of Concrete Science and Engineering*, vol. 1, pp. 173-84.

Lin, Z. & Li, V.C. 1997, 'Crack bridging in fiber reinforced cementitious composites with slip-hardening interfaces', *Journal of the Mechanics and Physics of Solids*, vol. 45, no. 5, pp. 763-87.

Lindner, A. & Shelley, M. 2015, 'Elastic fibers in flows', *Fluid-Structure Interactions in Low-Reynolds-Number Flows*, Royal Society of Chemistry, pp. 168-92.

Liu, G.-R. & Liu, M.B. 2003, *Smoothed particle hydrodynamics: A meshfree particle method*, World Scientific. 472pp.

Liu, M. & Liu, G. 2010, 'Smoothed particle hydrodynamics (SPH): An overview and recent developments', *Archives of Computational Methods in Engineering*, vol. 17, no. 1, pp. 25-76.

Liu, M., Liu, G. & Lam, K. 2003, 'Constructing smoothing functions in smoothed particle hydrodynamics with applications', *Journal of Computational and Applied Mathematics*, vol. 155, no. 2, pp. 263-84.

Liu, W.-K., Li, S. & Belytschko, T. 1997, 'Moving least-square reproducing kernel methods (I) methodology and convergence', *Computer methods in applied mechanics and engineering*, vol. 143, no. 1-2, pp. 113-54.

Lu, C. & Leung, C.K. 2017a, 'Theoretical evaluation of fiber orientation and its effects on mechanical properties in Engineered Cementitious Composites (ECC) with various thicknesses', *Cement and Concrete Research*, vol. 95, pp. 240-6.

Lu, C., Leung, C.K. & Li, V.C. 2017, 'Numerical model on the stress field and multiple cracking behavior of Engineered Cementitious Composites (ECC)', *Construction and Building Materials*, vol. 133, pp. 118-27.

Lu, C. & Leung, C.K.Y. 2017b, 'Effect of fiber content variation on the strength of the weakest section in Strain Hardening Cementitious Composites (SHCC)', *Construction and Building Materials*, vol. 141, pp. 253-8.

Lucy, L.B. 1977, 'A numerical approach to the testing of the fission hypothesis', *The Astronomical Journal*, vol. 82, pp. 1013-24.

Ma, H., Qian, S., Zhang, Z., Lin, Z. & Li, V.C. 2015, 'Tailoring engineered cementitious composites with local ingredients', *Construction and Building Materials*, vol. 101, pp. 584-95.

Maalej, M. & Li, V.C. 1994, 'Flexural/tensile-strength ratio in engineered cementitious composites', *Journal of Materials in Civil Engineering*, vol. 6, no. 4, pp. 513-28.

Maalej, M., Li, V.C. & Hashida, T. 1995, 'Effect of fiber rupture on tensile properties of short fiber composites', *Journal of Engineering Mechanics*, vol. 121, no. 8, pp. 903-13.

Marshall, D.B. & Cox, B.N. 1988, 'A J-integral method for calculating steady-state matrix cracking stresses in composites', *Mechanics of Materials*, vol. 7, no. 2, pp. 127-33.

Maruta, M., Kanda, T., Nagai, S. & Yamamoto, Y. 2005, 'New high-rise RC structure using pre-cast ECC coupling beam', *Concrete Journal*, vol. 43, no. 11, pp. 18-26.

Maya Duque, L.F. & Graybeal, B. 2016, 'Fiber orientation distribution and tensile mechanical response in UHPFRC', *Materials and Structures*, vol. 50, no. 1, p. 55.

Mechtcherine, V., Gram, A., Krenzer, K., Schwabe, J.-H., Shyshko, S. & Roussel, N. 2014, 'Simulation of fresh concrete flow using Discrete Element Method (DEM): Theory and applications', *Materials and Structures*, vol. 47, no. 4, pp. 615-30.

Meng, D., Huang, T., Zhang, Y.X. & Lee, C.K. 2017, 'Mechanical behaviour of a polyvinyl alcohol fibre reinforced engineered cementitious composite (PVA-ECC) using local ingredients', *Construction and Building Materials*, vol. 141, pp. 259-70.

Meng, D., Lee, C. & Zhang, Y. 2017, 'Flexural and shear behaviours of plain and reinforced polyvinyl alcohol-engineered cementitious composite beams', *Engineering Structures*, vol. 151, pp. 261-72.

Meng, W. & Khayat, K.H. 2017, 'Improving flexural performance of ultra-high-performance concrete by rheology control of suspending mortar', *Composites Part B: Engineering*, vol. 117, pp. 26-34.

Mohammed, B.S., Achara, B.E., Nuruddin, M.F., Yaw, M. & Zulkefli, M.Z. 2017, 'Properties of nano-silica-modified self-compacting engineered cementitious composites', *Journal of Cleaner Production*, vol. 162, pp. 1225-38.

Monaghan, J. & Kos, A. 1999, 'Solitary waves on a Cretan beach', *Journal of Waterway, Port, Coastal, and Ocean Engineering*, vol. 125, no. 3, pp. 145-55.

Monaghan, J.J. 1989, 'On the problem of penetration in particle methods', *Journal of Computational Physics*, vol. 82, no. 1, pp. 1-15.

Monaghan, J.J. 1992, 'Smoothed particle hydrodynamics', *Annual review of astronomy and astrophysics*, vol. 30, no. 1, pp. 543-74.

Monaghan, J.J. 1994, 'Simulating free surface flows with SPH', *Journal of Computational Physics*, vol. 110, no. 2, pp. 399-406.

Morris, J.P. 1996, *Analysis of smoothed particle hydrodynamics with applications*, PhD thesis, Monash University, Melbourne, Australia, 1996b.

Morris, J.P. 2000, 'Simulating surface tension with smoothed particle hydrodynamics', *International Journal for Numerical Methods in Fluids*, vol. 33, no. 3, pp. 333-53.

Naaman, A.E. 2007, 'High performance fiber reinforced cement composites: classification and applications', *CBM-CI international workshop, Karachi, Pakistan*, Citeseer, pp. 389-401.

Naaman, A.E. & Homrich, J.R. 1989, 'Tensile stress-strain properties of SIFCON', *Materials Journal*, vol. 86, no. 3, pp. 244-51.

Nagamoto, N. & Ozawa, K. 1997, 'Mixture Proportions of Self-Compacting High-Performance Concrete', *In: High-Performance Concrete: Design and Materials and Advances in Concrete Technology*, pp. 623-36.

Nak-Ho, S. & Suh, N.P. 1979, 'Effect of fiber orientation on friction and wear of fiber reinforced polymeric composites', *Wear*, vol. 53, no. 1, pp. 129-41.

Nomeritae, Daly, E., Grimaldi, S. & Bui, H.H. 2016, 'Explicit incompressible SPH algorithm for free-surface flow modelling: A comparison with weakly compressible schemes', *Advances in Water Resources*, vol. 97, pp. 156-67.

Noor, M.A. & Uomoto, T. 1999, 'Three-dimensional discrete element simulation of rheology tests of self-compacting concrete', *Proc. of the 1rd Int. RILEM Symp. on SCC*, pp. 35-46.

References

Okamura, H. & Ouchi, M. 2003, 'Self-compacting concrete', *Journal of Advanced Concrete Technology*, vol. 1, no. 1, pp. 5-15.

Okamura, H. & Ozawa, K. 1995, 'Mix design for self-compacting concrete', *Concrete Library of JSCE*, vol. 25, no. 6, pp. 107-20.

Ouyang, C., Pacios, A. & Shah, S. 1994, 'Pullout of inclined fibers from cementitious matrix', *Journal of Engineering Mechanics*, vol. 120, no. 12, pp. 2641-59.

Ozawa, K. 1995, 'Evaluation of self-compactability of fresh concrete using the funnel test', *Concr Lib JSCE*, vol. 25, pp. 59-75.

Pan, J. & Yuan, F. 2013, 'Seismic behaviors of ECC/Concrete composite beam-column joints under reversed cyclic loading', *VIII International Conference on Fracture Mechanics of Concrete and Concrete Structures*.

Papanastasiou, T.C. 1987, 'Flows of materials with yield', *Journal of Rheology*, vol. 31, no. 5, pp. 385-404.

Parra-Montesinos, G.J. 2005, 'High-performance fiber-reinforced cement composites: An alternative for seismic design of structures', *ACI Structural Journal*, vol. 102, no. 5, p. 668.

Parzen, E. 1962, 'On estimation of a probability density function and mode', *The Annals of Mathematical Statistics*, vol. 33, no. 3, pp. 1065-76.

Qudah, S. & Maalej, M. 2014, 'Application of Engineered Cementitious Composites (ECC) in interior beam–column connections for enhanced seismic resistance', *Engineering Structures*, vol. 69, pp. 235-45.

Ranade, R., Stults, M., Lee, B. & Li, V. 2012, 'Effects of fiber dispersion and flaw size distribution on the composite properties of PVA-ECC', *High Performance Fiber Reinforced Cement Composites 6*, Springer, pp. 107-14.

Randles, P.W. & Libersky, L.D. 1996, 'Smoothed Particle Hydrodynamics: Some recent improvements and applications', *Computer Methods in Applied Mechanics and Engineering*, vol. 139, no. 1, pp. 375-408.

Redon, C., Li, V.C., Wu, C., Hoshiro, H., Saito, T. & Ogawa, A. 2001, 'Measuring and modifying interface properties of PVA fibers in ECC matrix', *Journal of Materials in Civil Engineering*, vol. 13, no. 6, pp. 399-406.

Rogers, B.D. & Dalrymple, R.A. 2008, 'SPH modeling of tsunami waves', *Advanced Numerical Models for Simulating Tsunami Waves and Runup*, vol. 10, pp. 75-100.

Rokugo, K., Uchida, Y., Moriyama, M. & Lim, S. 2007, 'Direct tensile behavior and size effect of strain-hardening fiber-reinforced cement-based composites (SHCC)', *6th International Conference on FractureMechanics of Concrete and Concrete Structures*.

Şahmaran, M., Bilici, Z., Ozbay, E., Erdem, T.K., Yucel, H.E. & Lachemi, M. 2013, 'Improving the workability and rheological properties of Engineered Cementitious Composites using factorial experimental design', *Composites Part B: Engineering*, vol. 45, no. 1, pp. 356-68.

Sarmiento, E.V., Geiker, M.R. & Kanstad, T. 2016, 'Influence of fibre distribution and orientation on the flexural behaviour of beams cast from flowable hybrid polymer–steel FRC', *Construction and Building Materials*, vol. 109, pp. 166-76.

Sassani, A., Ceylan, H., Kim, S., Gopalakrishnan, K., Arabzadeh, A. & Taylor, P.C. 2017, 'Influence of mix design variables on engineering properties of carbon fiber-modified electrically conductive concrete', *Construction and Building Materials*, vol. 152, pp. 168-81.

Shao, S. & Lo, E.Y.M. 2003, 'Incompressible SPH method for simulating Newtonian and non-Newtonian flows with a free surface', *Advances in Water Resources*, vol. 26, no. 7, pp. 787-800.

Shimizu, K., Kanakubo, T., Kanda, T. & Nagai, S. 2004, 'Shear behavior of steel reinforced PVA-ECC beams', *13th World Conference on Earthquake Engineering, Conference Proceedings DVD, Paper*, p. 8.

Soltan, D.G. & Li, V.C. 2018, 'A self-reinforced cementitious composite for building-scale 3D printing', *Cement and Concrete Composites*, vol. 90, pp. 1-13.

Song, Q., Yu, R., Shui, Z., Wang, X., Rao, S. & Lin, Z. 2018, 'Optimization of fibre orientation and distribution for a sustainable Ultra-High Performance Fibre Reinforced Concrete (UHPFRC): Experiments and mechanism analysis', *Construction and Building Materials*, vol. 169, pp. 8-19.

Švec, O., Skoček, J., Stang, H., Geiker, M.R. & Roussel, N. 2012, 'Free surface flow of a suspension of rigid particles in a non-Newtonian fluid: A lattice Boltzmann approach', *Journal of Non-Newtonian Fluid Mechanics*, vol. 179, pp. 32-42.

Svec, O., Skocek, J., Stang, H., Olesen, J.F. & Poulsen, P.N. 2011, 'Flow simulation of fiber reinforced self compacting concrete using Lattice Boltzmann method', *8th International Congress on the Chemistry of Cement*.

Švec, O., Žirgulis, G., Bolander, J.E. & Stang, H. 2014, 'Influence of formwork surface on the orientation of steel fibres within self-compacting concrete and on the mechanical properties of cast structural elements', *Cement and Concrete Composites*, vol. 50, pp. 60-72.

Thanh, H.T., Li, J. & Zhang, Y. 2019, 'Numerical modelling of the flow of self-consolidating engineered cementitious composites using smoothed particle hydrodynamics', *Construction and Building Materials*, vol. 211, pp. 109-19.

Thanh, H.T., Li, J. & Zhang, Y.X. 2020, 'Numerical simulation of self-consolidating engineered cementitious composite flow with the V-funnel and U-box', *Construction and Building Materials*, vol. 236, p. 117467.

Torigoe, S.-i., Horikoshi, T., Ogawa, A., Saito, T. & Hamada, T. 2003, 'Study on evaluation method for PVA fiber distribution in engineered cementitious composite', *Journal of Advanced Concrete Technology*, vol. 1, no. 3, pp. 265-8.

Torrijos, M.C., Barragán, B.E. & Zerbino, R.L. 2010, 'Placing conditions, mesostructural characteristics and post-cracking response of fibre reinforced self-compacting concretes', *Construction and Building Materials*, vol. 24, no. 6, pp. 1078-85.

Tosun-Felekoğlu, K., Felekoğlu, B., Ranade, R., Lee, B.Y. & Li, V.C. 2014, 'The role of flaw size and fiber distribution on tensile ductility of PVA-ECC', *Composites Part B: Engineering*, vol. 56, pp. 536-45.

Van Mier, J., Ruiz, G., Andrade, C. & Yu, R. 2013, 'Fiber orientation in ultra high performance fiber reinforced concrete and its visualization', *Proceedings of the Eighth International Conference on Fracture Mechanics of Concrete and Concrete Structures*.

Vasilic, K., Meng, B., Kühne, H.-C. & Roussel, N. 2011, 'Flow of fresh concrete through steel bars: A porous medium analogy', *Cement and Concrete Research*, vol. 41, no. 5, pp. 496-503.

Vasilic, K., Schmidt, W., Kühne, H.-C., Haamkens, F., Mechtcherine, V. & Roussel, N. 2016, 'Flow of fresh concrete through reinforced elements: experimental validation of the porous analogy numerical method', *Cement and Concrete Research*, vol. 88, pp. 1-6.

Violeau, D. & Rogers, B.D. 2016, 'Smoothed particle hydrodynamics (SPH) for free-surface flows: past, present and future', *Journal of Hydraulic Research*, vol. 54, no. 1, pp. 1-26.

Wallevik, O.H. & Wallevik, J.E. 2011, 'Rheology as a tool in concrete science: The use of rheographs and workability boxes', *Cement and Concrete Research*, vol. 41, no. 12, pp. 1279-88.

Wang, R., Gao, X., Huang, H. & Han, G. 2017, 'Influence of rheological properties of cement mortar on steel fiber distribution in UHPC', *Construction and Building Materials*, vol. 144, pp. 65-73.

Wang, S. & Li, V.C. 2007, 'Engineered cementitious composites with high-volume fly ash', *Materials Journal*, vol. 104, no. 3, pp. 233-41.

Wendland, H. 1995, 'Piecewise polynomial, positive definite and compactly supported radial functions of minimal degree', *Advances in Computational Mathematics*, vol. 4, no. 1, pp. 389-96.

Wu, C., Pan, Z., Su, R., Leung, C. & Meng, S. 2017, 'Seismic behavior of steel reinforced ECC columns under constant axial loading and reversed cyclic lateral loading', *Materials and Structures*, vol. 50, no. 1, p. 78.

Wu, H.C. & Li, V.C. 1992, 'Snubbing and bundling effects on multiple crack spacing of discontinuous random fiber-reinforced brittle matrix composites', *Journal of the American Ceramic Society*, vol. 75, no. 12, pp. 3487-9.

Wu, J., Liu, X., Xu, H. & Du, H. 2016, 'Simulation on the self-compacting concrete by an enhanced Lagrangian particle method', *Advances in Materials Science and Engineering*, vol. 2016.

Wu, M., Johannesson, B. & Geiker, M. 2012, 'A review: Self-healing in cementitious materials and engineered cementitious composite as a self-healing material', *Construction and Building Materials*, vol. 28, no. 1, pp. 571-83.

Xu, L., Pan, J. & Chen, J. 2017, 'Mechanical behavior of ECC and ECC/RC composite columns under reversed cyclic loading', *Journal of Materials in Civil Engineering*, p. 04017097.

Y.M. Lo, E. & Shao, S. 2002, 'Simulation of near-shore solitary wave mechanics by an incompressible SPH method', *Applied Ocean Research*, vol. 24, no. 5, pp. 275-86.

Yang, E.-H., Sahmaran, M., YINGZI, Y. & Li, V.C. 2009, 'Rheological control in production of engineered cementitious composites', *ACI Materials Journal*, vol. 106, no. 4, pp. 357-66.

Yang, E.-H., Wang, S., Yang, Y. & Li, V.C. 2008, 'Fiber-bridging constitutive law of engineered cementitious composites', *Journal of Advanced Concrete Technology*, vol. 6, no. 1, pp. 181-93.

Yang, E.-H., Yang, Y. & Li, V.C. 2007, 'Use of high volumes of fly ash to improve ECC mechanical properties and material greenness', *ACI materials journal*, vol. 104, no. 6, pp. 620-8.

Yang, X. & Liu, M. 2017, 'Particle-Based Modeling of Asymmetric Flexible Fibers in Viscous Flows', *Communications in Computational Physics*, vol. 22, pp. 1015-27.

Yang, X., Peng, S. & Liu, M. 2014, 'A new kernel function for SPH with applications to free surface flows', *Applied Mathematical Modelling*, vol. 38, no. 15, pp. 3822-33.

Yashiro, S. 2017, 'Application of particle simulation methods to composite materials: a review', *Advanced Composite Materials*, vol. 26, no. 1, pp. 1-22.

Yashiro, S., Sasaki, H. & Sakaida, Y. 2012, 'Particle simulation for predicting fiber motion in injection molding of short-fiber-reinforced composites', *Composites Part A: Applied Science and Manufacturing*, vol. 43, no. 10, pp. 1754-64.

Yu, K.-Q., Yu, J.-T., Dai, J.-G., Lu, Z.-D. & Shah, S.P. 2018, 'Development of ultra-high performance engineered cementitious composites using polyethylene (PE) fibers', *Construction and Building Materials*, vol. 158, pp. 217-27.

Yu, K., Ding, Y. & Zhang, Y.X. 2020, 'Size effects on tensile properties and compressive strength of engineered cementitious composites', *Cement and Concrete Composites*, vol. 113, p. 103691.

Yuan, F., Pan, J., Xu, Z. & Leung, C. 2013, 'A comparison of engineered cementitious composites versus normal concrete in beam-column joints under reversed cyclic loading', *Materials and structures*, vol. 46, no. 1-2, pp. 145-59.

Zerbino, R., Tobes, J.M., Bossio, M.E. & Giaccio, G. 2012, 'On the orientation of fibres in structural members fabricated with self compacting fibre reinforced concrete', *Cement and Concrete Composites*, vol. 34, no. 2, pp. 191-200.

Zhang, J. & Li, V.C. 2002, 'Effect of inclination angle on fiber rupture load in fiber reinforced cementitious composites', *Composites Science and Technology*, vol. 62, no. 6, pp. 775-81.

Zhou, B. & Uchida, Y. 2017a, 'Influence of flowability, casting time and formwork geometry on fiber orientation and mechanical properties of UHPFRC', *Cement and Concrete Research*, vol. 95, pp. 164-77.

Zhou, B. & Uchida, Y. 2017b, 'Relationship between fiber orientation/distribution and post-cracking behaviour in ultra-high-performance fiber-reinforced concrete (UHPFRC)', *Cement and Concrete Composites*, vol. 83, no. Supplement C, pp. 66-75.

Zhou, J., Qian, S., Beltran, M.G.S., Ye, G., van Breugel, K. & Li, V.C. 2010, 'Development of engineered cementitious composites with limestone powder and blast furnace slag', *Materials and Structures*, vol. 43, no. 6, pp. 803-14.

Zhou, J., Qian, S., Ye, G., Copuroglu, O., van Breugel, K. & Li, V.C. 2012, 'Improved fiber distribution and mechanical properties of engineered cementitious composites by adjusting the mixing sequence', *Cement and Concrete Composites*, vol. 34, no. 3, pp. 342-8.

Zhu, B., Pan, J., Nematollahi, B., Zhou, Z., Zhang, Y. & Sanjayan, J. 2019, 'Development of 3D printable engineered cementitious composites with ultra-high tensile ductility for digital construction', *Materials & Design*, vol. 181, p. 108088.

Zollo, R.F. 1997, 'Fiber-reinforced concrete: An overview after 30 years of development', *Cement and Concrete Composites*, vol. 19, no. 2, pp. 107-22.